

Heikki Suikkanen

**APPLICATION AND DEVELOPMENT OF
NUMERICAL METHODS FOR THE MODELLING OF
INNOVATIVE GAS COOLED FISSION REACTORS**

Thesis for the degree of Doctor of Science (Technology) to be presented with due permission for public examination and criticism in the Auditorium 1383 at Lappeenranta University of Technology, Lappeenranta, Finland on the 5th of December, 2014, at noon.

Acta Universitatis
Lappeenrantaensis 610

Supervisor Professor Riitta Kyrki-Rajamäki
LUT School of Technology
Department of Energy Technology
Lappeenranta University of Technology
Finland

Reviewers Professor Lars Davidson
Division of Fluid Dynamics
Department of Applied Mechanics
Chalmers University of Technology
Sweden

Assistant Professor Danny Lathouwers
Faculty of Applied Sciences
Department of Radiation Science and Technology
Delft University of Technology
Netherlands

Opponent Dr. Timo Pätkängas
VTT Technical Research Centre of Finland
Finland

ISBN 978-952-265-698-8
ISBN 978-952-265-699-5 (PDF)
ISSN-L 1456-4491
ISSN 1456-4491
Lappeenrannan teknillinen yliopisto
Yliopistopaino 2014

Abstract

Heikki Suikkanen

Application and development of numerical methods for the modelling of innovative gas cooled fission reactors

Lappeenranta 2014

130 p.

Acta Universitatis Lappeenrantaensis 610

Diss. Lappeenranta University of Technology

ISBN 978-952-265-698-8, ISBN 978-952-265-699-5 (PDF)

ISSN-L 1456-4491, ISSN 1456-4491

Innovative gas cooled reactors, such as the pebble bed reactor (PBR) and the gas cooled fast reactor (GFR) offer higher efficiency and new application areas for nuclear energy. Numerical methods were applied and developed to analyse the specific features of these reactor types with fully three dimensional calculation models. In the first part of this thesis, discrete element method (DEM) was used for a physically realistic modelling of the packing of fuel pebbles in PBR geometries and methods were developed for utilising the DEM results in subsequent reactor physics and thermal-hydraulics calculations. In the second part, the flow and heat transfer for a single gas cooled fuel rod of a GFR were investigated with computational fluid dynamics (CFD) methods.

An in-house DEM implementation was validated and used for packing simulations, in which the effect of several parameters on the resulting average packing density was investigated. The restitution coefficient was found out to have the most significant effect. The results can be utilised in further work to obtain a pebble bed with a specific packing density. The packing structures of selected pebble beds were also analysed in detail and local variations in the packing density were observed, which should be taken into account especially in the reactor core thermal-hydraulic analyses.

Two open source DEM codes were used to produce stochastic pebble bed configurations to add realism and improve the accuracy of criticality calculations performed with the Monte Carlo reactor physics code Serpent. Russian ASTRA criticality experiments were calculated. Pebble beds corresponding to the experimental specifications within measurement uncertainties were produced in DEM simulations and successfully exported into the subsequent reactor physics analysis. With the developed approach, two typical issues in Monte Carlo reactor physics calculations of pebble bed geometries were avoided.

A novel method was developed and implemented as a MATLAB code to calculate porosities in the cells of a CFD calculation mesh constructed over a pebble bed obtained from DEM simulations. The code was further developed to distribute power and temperature data accurately between discrete based reactor physics and continuum based thermal-hydraulics models to enable coupled reactor core calculations. The developed method was also found useful for analysing sphere packings in

general.

CFD calculations were performed to investigate the pressure losses and heat transfer in three dimensional air cooled smooth and rib roughened rod geometries, housed inside a hexagonal flow channel representing a sub-channel of a single fuel rod of a GFR. The CFD geometry represented the test section of the L-STAR experimental facility at Karlsruhe Institute of Technology and the calculation results were compared to the corresponding experimental results. Knowledge was gained of the adequacy of various turbulence models and of the modelling requirements and issues related to the specific application.

The obtained pressure loss results were in a relatively good agreement with the experimental data. Heat transfer in the smooth rod geometry was somewhat under predicted, which can partly be explained by unaccounted heat losses and uncertainties. In the rib roughened geometry heat transfer was severely under predicted by the used realisable $k - \epsilon$ turbulence model. An additional calculation with a $v^2 - f$ turbulence model showed significant improvement in the heat transfer results, which is most likely due to the better performance of the model in separated flow problems. Further investigations are suggested before using CFD to make conclusions of the heat transfer performance of rib roughened GFR fuel rod geometries.

It is suggested that the viewpoints of numerical modelling are included in the planning of experiments to ease the challenging model construction and simulations and to avoid introducing additional sources of uncertainties. To facilitate the use of advanced calculation approaches, multi-physical aspects in experiments should also be considered and documented in a reasonable detail.

Keywords: nuclear reactors, gas cooled reactors, high temperature reactors, pebble bed reactors, gas cooled fast reactors, computational fluid dynamics, discrete element method

UDC: 621.039.5:621.039.534.2:51.001.57:519.61:004.94

Acknowledgements

The funding of this work and my postgraduate studies between 2009 and 2014 has come from several sources. I would like to thank the Academy of Finland for the financial support they have given for the research of new type nuclear reactors, first in the New Type Nuclear Reactors project (Grant No. 124264) and then in the Coupled Multi-Physics Modelling of Pebble Bed Reactor Core project (Grant No. 258145). I also wish to thank Fortum Oyj. for their participation to the funding of the former project. In between these projects, I was selected as a fully sponsored member of the YTERA doctoral school whose board I wish to thank for their trust and support. My acknowledgements go also for the European Commission as the work presented in the second part of my dissertation was conducted in the FP 7 EC collaborative project THINS (Grant agreement No. 249337). I also wish to express my gratitude to the Doctoral School of Computational Fluid Dynamics (2009) and the Research Foundation of Lappeenranta University of Technology for the travel and support grants they have given for my postgraduate studies and research.

I would like to thank my supervisor, professor Riitta Kyrki-Rajamäki not only for guiding me through my doctoral studies but also for introducing me to the serious and important world of project management and applying research funding. I also wish to thank her for encouraging me to participate several international courses, conferences and collaborations from the very beginning of my doctoral studies. These things have greatly widened my perspective to research work and to the world in general. For my dissertation work Professor Kyrki-Rajamäki has given me much room to find my own way but has still given many valuable comments and suggestions during the work and the finalisation of this dissertation. Professor Kyrki-Rajamäki has a remarkable talent to get things progressing even when the deadline was already yesterday.

The preliminary examiners of my dissertation, professor Lars Davidson and assistant professor Danny Lathouwers I would like to thank for their good comments and suggestions, which helped to further improve this work. My opponent Dr. Timo Pättikangas I would like to thank in advance for his efforts and undoubtedly very good comments and questions he will raise during the public defence of my dissertation.

My friend and colleague Ville Rintala has played a vital role in the success of this work. With his skilful reactor physics input to the modelling of pebble bed reactors we have together managed to do things no-one else has done before. He also possesses a deep passion for developing and maintaining our computer clusters which has made it possible to perform the calculations in this work. This is very valuable work as it has a direct positive effect to the output of many other researchers.

I wish to thank Dr. Jouni Ritvanen and Dr. Payman Jalali for introducing me to the practise of discrete element modelling and for the nice interlaboratory work we managed to process into the form of a publication. Dr. Jalali was also responsible for the major part of my post-graduate courses and I have to mention that they were very inspiring and of excellent quality. Dr. Ritvanen I have to thank also for his numerous helpful tips, tricks and templates which he seems very keen on sharing.

Within the THINS project I had the pleasure to work with Rodrigo Gómez from KIT and Sebastian Buchholz from GRS. I wish to thank both of them for the successful co-operation which resulted in a joint publication. Rodrigo Gómez and the whole L-STAR experimental team deserve my thanks for the hard work they have done to run the experiments.

I would like to thank Dr. Jaakko Leppänen from VTT for his input in our reactor physics work. Without the efficient reactor physics code Serpent and the HTR specific models he implemented into Serpent, it would have been practically impossible to utilise the results of my DEM simulations in the subsequent reactor physics calculations.

For proofreading this thesis and pointing out some technicalities in writing english, I would like to express my gratitude to Sari Silventoinen. I wish to thank also Markku Nikku and Ville Rintala for pointing out some mistakes in the text.

I wish to thank everyone in my laboratory and also the people who have participated the coffee breaks in the "secret" coffee room for nice discussions and slight distractions.

All friends who have shared with me the time when I have not been working or studying, including also some of whom I have already mentioned, I want to thank for the good time and the important distraction from the sometimes too serious and absorbing work.

My parents and family have always supported and valued my desire to study and have never pushed me in any direction I did not want to go myself. For this I am very grateful. I am also very grateful to Päivi, who has been by my side the whole time I have pursued the degree of doctor. She has been the most valuable person supporting me during this sometimes stressful period of my life.

At the time of writing these acknowledgements I am just a few kilometres away from the site where two full scale pebble bed high temperature reactors are under construction. Doing research on a technology that has minor interest in Finland can feel quite lonely at times. It is thus encouraging to follow the progress of the technology in China and feel that the results of my work might soon become useful in practice.

Heikki Suikkanen
29th of October, 2014
Weihai, China

Contents

Abstract

Acknowledgements

Contents

Nomenclature	11
1 Introduction	15
1.1 About gas cooled reactors	15
1.2 Background and objectives	18
1.3 Outline and scientific contribution	19
Part I DEM modelling for gas cooled pebble bed reactors	23
2 Background and state of art	25
2.1 A brief review of related work	26
3 Methods for discrete element simulation and data analysis	29
3.1 Contact of two spheres	29
3.2 Contact force models	30
3.2.1 Normal force	30
3.2.2 Tangential force	31
3.2.3 Force summation	32
3.3 Time integration and simulation time step	32
3.4 Data analysis methods	33
3.4.1 Average packing density	34
3.4.2 Area based packing density profiles	34
3.4.3 Local packing density	35
4 Pebble packing studies for an annular reactor core geometry	37
4.1 Calculation model	37
4.2 Packing simulation results	39
4.2.1 Comparisons with experimental data	39
4.2.2 Average packing densities	40
4.2.3 Local packing structures	42
5 Enhancing neutronics analyses with realistic pebble packing data	47
5.1 Discrete element simulation codes	48
5.2 ASTRA packing simulation models	49
5.3 ASTRA packing simulation results	52
5.4 Feedback from reactor physics calculations	55

6	Mapping discrete pebble bed data to continuum volume elements	59
6.1	Description of the method	60
6.2	Application examples	63
6.2.1	Mapping data from discrete to continuum models	64
6.2.2	Extracting volumetric packing density data	68
7	Summary and conclusions of Part I	73
Part II CFD modelling for gas cooled fast reactors		77
8	Background and state of art	79
8.1	A brief review of related work	79
8.2	Description of the related experiments	81
9	Flow and heat transfer models	85
9.1	Governing equations	85
9.2	Turbulence modelling	86
9.2.1	Realisable $k - \epsilon$ model equations	87
9.2.2	Reynolds stress model equations	88
9.2.3	Near wall treatment	89
9.3	Turbulent heat transfer modelling	90
10	CFD calculation model	91
10.1	Geometry and materials	91
10.1.1	Flow conditioner	93
10.1.2	Surface roughness elements	93
10.2	Calculation mesh	94
10.3	Cell zone and boundary conditions	95
10.3.1	Porous zones	97
10.4	Turbulence models	98
10.5	Heat transfer models	99
10.6	Solver and numerical methods	99
11	CFD calculation results	101
11.1	Data extraction locations and dimensionless parameters	101
11.2	Numerical reliability of the results	103
11.2.1	Mesh convergence	103
11.2.2	Iteration convergence	107
11.3	Results and comparisons with experimental data	108
11.3.1	Total loss coefficients	108
11.3.2	Friction factors	110
11.3.3	Nusselt numbers and rod temperature profiles	111
12	Summary and conclusions of Part II	117

13 Final comments

119

References

121

Nomenclature

Latin alphabet

A	Area	m^2
\mathbf{a}	Translational acceleration vector	m/s^2
a, b	Polynomial coefficients	-
B_{ij}	Buoyancy production tensor in RSM model	$\text{kg}/(\text{m s}^3)$
C	Inertial loss coefficient	-
C_1, C_2	Coefficients in the $k - \epsilon$ turbulence model	-
C_μ	Coefficient in the $k - \epsilon$ turbulence model	-
c_p	Specific heat capacity	$\text{m}^2/(\text{s}^2 \text{K})$
D_{ij}	Turbulent diffusion tensor in RSM model	$\text{kg}/(\text{m s}^3)$
d	Diameter	m
E_{ij}	Dissipation tensor in RSM model	$\text{kg}/(\text{m s}^3)$
E	Young's modulus	$\text{kg}/(\text{m s}^2)$
e	Restitution coefficient	-
\mathbf{F}	Force vector	$\text{kg m}/\text{s}^2$
F	Force	$\text{kg m}/\text{s}^2$
f	Friction factor, relaxation function	-, -
f_D	Darcy friction factor	-
G	Shear modulus	$\text{kg}/(\text{m s}^2)$
G_b	Generation of k due to buoyancy	$\text{kg}/(\text{m s}^3)$
G_k	Generation of k due to mean velocity gradients	$\text{kg}/(\text{m s}^3)$
\mathbf{g}	Gravitational acceleration vector	m/s^2
g	Gravitational acceleration	m/s^2
H	Width	m
h	Specific enthalpy, heat transfer coefficient	$\text{m}^2/\text{s}^2, \text{kg}/(\text{s}^3 \text{K})$
I	Moment of inertia	kg m^2
K	Permeability	m^2
k	Stiffness, multiplication factor, turbulence kinetic energy	$\text{kg}/\text{s}^2, -, \text{m}^2/\text{s}^2$
L	Thickness	m
m	Mass	kg
\dot{m}	Mass flow rate	kg/s
Ma	Mach number	-
N	Number of entities	-
\mathbf{n}	Normal unit vector	-
Nu	Nusselt number	-
P	Probability	-
p	Pressure	$\text{kg}/(\text{m s}^2)$
\bar{p}	Mean pressure	$\text{kg}/(\text{m s}^2)$
p'	Fluctuating pressure	$\text{kg}/(\text{m s}^2)$
p'_1, p'_2	Pressures at measurement window positions	$\text{kg}/(\text{m s}^2)$
Pr	Prandtl number	-

Pr_ϵ	Turbulent Prandtl number for ϵ	-
Pr_k	Turbulent Prandtl number for k	-
Pr_t	Turbulent Prandtl number for energy	-
\dot{Q}	Power	$\text{kg m}^2/\text{s}^2$
q''	Heat flux	kg/s^3
R	Radius	m
\mathbf{r}	Position vector	m
r	Radial coordinate	m
Re	Reynolds number	-
S_h	Energy source term	$\text{kg}/(\text{m s}^3)$
s_{ij}	Strain rate tensor	1/s
\bar{s}_{ij}	Mean strain rate tensor	1/s
\mathbf{T}	Torque vector	$\text{kg m}^2/\text{s}^2$
T	Temperature	K
\bar{T}	Mean temperature	K
T'	Fluctuating temperature	K
\mathbf{t}	Tangential unit vector	-
t	Time	s
t_{ij}	Viscous stress tensor	$\text{kg}/(\text{m s}^2)$
\mathbf{v}	Velocity vector	m/s
v	Velocity	m/s
\bar{v}	Mean velocity	m/s
v'	Fluctuating velocity	m/s
v^+	Dimensionless velocity	-
v_τ	Friction velocity	m/s
x, y, z	Cartesian coordinates	m
\dot{x}	Velocity	m/s
\ddot{x}	Acceleration	m/s^2
y^+	Dimensionless wall normal distance	-
z'_1, z'_2	Axial positions at measurement windows	m

Greek alphabet

α	Angular acceleration vector	rad/s^2
δ	Overlap distance/deformation vector	m
δ	Overlap distance/deformation	m
δ_{ij}	Kronecker delta tensor	-
ϵ	Turbulence dissipation rate	m^2/s^3
ε	Porosity	-
η	Damping coefficient	kg/s
θ	Angular coordinate	rad
λ	Thermal conductivity	$\text{kg m}/(\text{s}^3 \text{K})$
λ_t	Turbulent thermal conductivity	$\text{kg m}/(\text{s}^3 \text{K})$
μ	Dynamic viscosity	$\text{kg}/(\text{m s})$

μ_f	Friction coefficient	-
μ_t	Eddy/turbulent viscosity	kg/(m s)
ν	Poisson's ratio	-
Π_{ij}	Pressure-strain tensor in RSM model	kg/(m s ³)
ρ	Density	kg/m ³
σ	Standard deviation	-
$\boldsymbol{\tau}$	Stress tensor	kg/(m s ²)
τ_w	Wall shear stress	kg/(m s ²)
ϕ	Packing density/fraction	-
$\bar{\phi}$	Average packing density/fraction	-
$\boldsymbol{\omega}$	Angular velocity vector	rad/s
ω	Specific turbulence dissipation rate	1/s

Subscripts

1, 2	Axial measurement locations at/near inlet, outlet
B	Body
b	bulk
c	Critical, cross section
con	Convective
eff	Effective
f	Fluid
heating	Heating
h	Hydraulic
$i, j, (k)$	Indices for spheres/pebbles, indices in the Einstein summation notation
init	Initial
inner	Inner wall
losses	Losses
m	Moderator, mean
outer	Outer wall
p	Pebble
rod	Rod
r	Relative
s	Slip, solid, surface
tot	Total
vor	Voronoi

Abbreviations

3D	Three dimensional
AGR	Advanced gas cooled reactor
ASM	Algebraic stress model
AVR	Arbeitsgemeinschaft Versuchsreaktor
CAD	Computer aided design

CEA	Commissariat à l'énergie et aux énergies alternatives
CFD	Computational fluid dynamics
CPU	Central processing unit
DEM	Discrete element method
DIN	Deutsches Institut für Normung
DNS	Direct numerical simulation
EARSM	Explicit algebraic Reynolds stress model
EIR	Eidgenössisches Institut für Reactorforchung
EWT	Enhanced wall treatment
GCR	Gas cooled reactor
GFR	Gas cooled fast reactor
HTGR	High temperature gas cooled reactor
HTR-10	10 MW high temperature gas cooled reactor
HTR-PM	High temperature reactor pebble bed module
HTR	High temperature reactor
HTTR	High temperature engineering test reactor
INET	Institute of Nuclear and New Energy Technology
KfK	Kernforschungszentrum Karlsruhe
KIT	Karlsruhe Institute of Technology
KTA	Kerntechnischer Ausschuss
L-STAR	Luft, Stab, Abstandhalter, Rauheiten
LDA	Laser Doppler anemometry
LES	Large eddy simulation
LWR	Light water reactor
MPI	Message passing interface
OEEC	Organisation for European Economic Co-operation
PBMR	Pebble bed modular reactor
PBR	Pebble bed reactor
RANS	Reynolds averaged Navier-Stokes
REV	Representative elementary volume
RRC	Russian Research Center
RSM	Reynolds stress model
S2S	Surface to surface
SIMPLE	Semi implicit method for pressure-linked equations
STL	Stereolithography
THINS	Thermal Hydraulics of Innovative Nuclear Systems
THTR	Thorium high temperature reactor
TRISO	Tri-structural isotropic
UNGG	Uranium naturel graphite gaz

1 Introduction

1.1 About gas cooled reactors

Despite the fact that the majority of the nuclear power reactors today are light water reactors (LWR), several gas cooled reactors (GCR) have been constructed in the past, some of which are still in operation. While the LWRs represent an already mature technology, advanced reactors designed with gas cooling still require major development efforts to realise their full potential. This potential includes increased efficiency and entirely new application areas for nuclear energy due to high operating temperatures made possible partly by the use of a gas coolant. Practically two gaseous materials, namely carbon dioxide and helium, are considered suitable for reactor cooling (Melese and Katz, 1984). Carbon dioxide was typically used in the past GCRs but as it has an unfavourable corroding effect with graphite, the typical moderator and structural material in GCRs, helium has become the preferred coolant option for modern GCR designs.

There are several advantages in using a gas coolant and specifically helium over other practical reactor coolants. Helium does not interact with neutrons significantly. This simplifies the reactor physical design as the coolant has an insignificant role in moderating neutrons contrary to, for example water, and thus makes it a more suitable coolant option also for fast spectrum reactors. Helium itself does not become radioactive although the possible impurities in the coolant might. Also, as helium gas is transparent the maintenance of the reactor circuit is easier compared to, for example, lead-bismuth cooled reactors where radioactive polonium is produced and the coolant is opaque. Helium is also chemically inert so that it does not contribute to the corrosion of reactor materials like liquid lead and supercritical water or have the possibility of unfavourable exothermic chemical reactions like sodium has when it comes in contact with water or air. Yet another good feature is that there is no phase change in the normal or abnormal operating conditions which further simplifies the reactor design and does not become a limiting factor for the operating temperature.

Despite the many advantages there are also challenges in using helium as a reactor coolant. Due to its low density helium needs to be pressurised to obtain sufficient heat transfer properties. Retaining a high pressure level in the primary circuit is not as crucial an issue from the safety perspective for thermal neutron spectrum reactors, where the core typically contains large amounts of thermal inertia in the form of graphite. However, if used as the coolant in fast spectrum reactors where the graphite is missing, the reactor circuit needs to retain at least some pressure level even to transfer decay heat from a shut down reactor core. This requires optimisation of the heat transfer from fuel to the coolant and design of additional safety systems to guarantee a sufficient pressure level in the reactor circuit in all circumstances. Another, yet manageable issue is the leakage of helium from the primary circuit due to helium being such a small atom. Special attention needs to be put into the tightness of the circuit to keep helium losses at minimum. In graphite moderated

thermal GCRs it is also important to secure the integrity of the primary circuit to prevent the ingress of air into the loop after its depressurisation which could cause oxidation of graphite and thus increase material temperatures and eventually lead to the release of radioactivity (Hishida et al., 1993). However, this issue does not directly arise from using gas cooling.

Several thermal GCRs have been constructed in the past. First ones were developed in Britain and in France in the 1950's. They were at first used to produce weapon plutonium but later on also electricity. Carbon dioxide was used as the coolant in the first generation GCRs, which were called Magnox in Britain and UNGG (uranium naturel graphite gaz) in France (Melese and Katz, 1984). Although independently developed, the reactors had rather identical design features. Natural uranium was used as the fuel which was possible by using graphite as the moderator and a fuel cladding material with a low neutron absorption cross section (Magnox alloy). The first reactors were assembled inside a steel pressure vessel but later on pre-stressed concrete pressure vessels were developed because of the huge size of the reactors. In Britain 26 and in France 8 such reactors were built and a few were exported to Italy, Japan and Spain (Goodjohn, 1991).

GCRs were further developed in Britain. The second generation was the advanced gas cooled reactor (AGR) designed for higher efficiency and fuel burnup than Magnox (Melese and Katz, 1984). This was achieved by using a slightly enriched uranium fuel now enclosed inside a stainless steel cladding capable of withstanding higher operating temperatures than the Magnox alloy. Carbon dioxide was still used as the coolant. Core power density was increased and thus also the physical dimensions of the reactor were reduced. The first AGR was started in Windscale in 1963, a prototype reactor which has already been shut down (Melese and Katz, 1984). A total of 14 AGRs were started between 1976–1988 (Goodjohn, 1991).

A helium cooled high temperature reactor (HTR) was being developed in parallel with the AGR. With the entire core built of ceramic materials it was possible to increase the operating temperature. The first HTR test reactor, Dragon, was built in Britain as an OEEC (Organisation for European Economic Co-operation) coordinated project and it operated from 1964 to 1977 (Simmnad, 1991). Dragon was primarily used in experiments with different fuels and materials, such as the coated particle fuel TRISO (tri-structural isotropic), which was the fuel type to be used in the later HTRs. HTRs with the TRISO fuel particles enclosed inside graphite spheres with a diameter of 60 mm were developed in West Germany (Stansfield, 1991). A critical core was formed by piling these "pebbles" inside a cavity surrounded by graphite blocks. The core was cooled by a helium flow that was forced through the pebble bed. This type of HTR came to be known as the pebble bed reactor (PBR) and two such reactors were built in West Germany. First was the prototype reactor AVR (Arbeitsgemeinschaft Versuchsreaktor) which was operated from 1967 to 1987 (Marnet et al., 1991). AVR was followed by a 300 MW_e thorium high temperature reactor (THTR) which had its first criticality in 1983 and was shutdown in 1988 (Baumer and Kalinowski, 1991). HTRs were also developed in the United States, although an acronym HTGR (high temperature gas cooled

reactor) was used. These reactors were also designed in a more conventional way and thus instead of graphite pebbles the TRISO fuel particles were enclosed inside small graphite rods which were placed into bigger graphite blocks (Stansfield, 1991). The reactor core was then assembled from these blocks which also included channels for the helium flow. A prototype reactor was built and operated in Peach Bottom Pennsylvania between 1966 and 1974 (Simnad, 1991) followed by a 330 MW_e power reactor that was built in Fort St. Vrain in Colorado and started producing electricity in 1976 (Brey, 1991).

Despite the relatively good experiences with HTRs and enthusiasm to even construct fast spectrum breeder reactors with a gas cooling (Melese-d'Hospital and Simon, 1977), the development of gas cooled reactors like the development of many other advanced reactor concepts stalled in most countries mainly due to political reasons in the late 1980's. However, motivated by the possibility to produce industrial process heat by nuclear reactors, a test reactor with a similar design as the HTGRs in the United States was constructed in Japan (Shiozawa et al., 2004). This 30 MW_{th} reactor HTTR (high temperature engineering test reactor) had its first criticality in 1998 and is still in use. One of the important objectives with HTTR is to investigate the production of hydrogen using nuclear heat produced by HTRs. The reactor has demonstrated coolant outlet temperatures around 950 °C which opens up new possibilities to utilise nuclear energy in the process industry (Fujikawa et al., 2004). Also a 10 MW high temperature gas cooled reactor (HTR-10) based on the German pebble bed concept was built in China (Wu et al., 2002). This test reactor had its first criticality in 2000 and it was built to acquire experience on the HTR technology and investigate the cogeneration of heat and electricity and the safety features of HTRs (Xu and Zuo, 2002).

A few full scale HTR reactor projects have seen light in the 21st century. A major effort in HTR development was launched in 1994 in South Africa led by the electricity utility Eskom (Koster et al., 2003). Pebble Bed Modular Reactor (Pty) Limited was formed in 1999 from various actors in the nuclear industry to design and construct a modern pebble bed modular reactor (PBMR) for the cogeneration of heat and electricity. The PBMR design featured a helium turbine in the primary loop, that is, a Brayton cycle for electricity generation and a high reactor outlet temperature of 900 °C. The project, however, came to its conclusion when the South African government ceased to fund the project in 2010. Another project to construct a modern PBR emerged in China (Zhang et al., 2009). Design of a modular HTR-PM (high temperature reactor pebble bed module) is led by the Institute of Nuclear and New Energy Technology (INET) of the Tsinghua University. The experience gained from the test reactor HTR-10 has been used in designing a PBR with design choices based on already proven technology.

In addition to thermal GCRs, gas cooled fast reactors (GFR) have also regained some renewed interest (Stainsby et al., 2011). Not even a single research reactor with a fast spectrum and gas cooling has been built so far. Some research is, however, conducted and a GFR prototype reactor ALLEGRO has been envisaged to be constructed in Europe (Poette et al., 2009).

1.2 Background and objectives

In this thesis, some of the challenges in the development of GCRs, specifically the pebble bed high temperature reactor and the gas cooled fast reactor, are addressed. Modern computational methods are applied, developed and validated to study various aspects related to the reactor types with three dimensional calculation models.

The work related to PBRs is a part of an effort to develop a new type of a three dimensional calculation system for full core PBR analyses coupling Monte Carlo reactor physics with a thermal-hydraulic solver using a porous medium model for the pebble bed. A computational method for modelling particulate materials known as the discrete element method (DEM) is used to provide a realistic representation of the packing of the fuel pebbles inside the reactor core for the reactor physics and thermal-hydraulics calculations. While the author of this thesis is also responsible for the development of the thermal-hydraulic tool, the details of the PBR thermal-hydraulic models have been left outside of this thesis as the emphasis is in the DEM simulations and development of data transfer methods from DEM to the reactor physics and thermal-hydraulics models.

The work related to GFRs is an effort to validate computational fluid dynamics (CFD) models for the GFR analyses related especially to the development of the European demonstration reactor ALLEGRO. The turbulent flow and heat transfer in a three dimensional gas cooled heated rod geometry representing a sub channel of a GFR is investigated numerically with CFD. The CFD calculation results are compared with the results of the related experiments performed at the Karlsruhe Institute of Technology (KIT) to validate the CFD models. The studies include heated rods with a smooth and a rib roughened surfaces.

The work presented in this thesis has been done within several projects. The work related to PBRs has been done in the *New Type Nuclear Reactors* project funded primarily by the Academy of Finland and partly by Fortum Oyj. and the *Coupled Multi-Physics Modelling of Pebble Bed Nuclear Reactor Core* project funded solely by the Academy of Finland. The work related to GFRs has been done within the Seventh Framework Programme project *Thermal Hydraulics of Innovative Nuclear Systems* funded by the European Commission.

Objectives of the work presented in this thesis

- Establishment of capabilities and experience for the discrete element modelling and analysis of the packing of fuel elements in PBRs.
- Application of discrete element modelling to construct realistic pebble bed configurations for subsequent reactor physics and thermal-hydraulics calculations.
- Development of a method to transfer data accurately from the discrete pebble bed models to volume averaged continuum models.

- Validation of CFD calculation models and their application practices for the flow and heat transfer analyses of gas cooled fuel rod geometries.

1.3 Outline and scientific contribution

This thesis has been divided into two parts. The first part covers the work related to the DEM modelling of PBRs while the second part presents the CFD calculations related to GFRs.

The contents of the individual chapters is briefly the following. Chapter 2 provides background information and a literature review for the first part of the thesis. The models and methodology behind DEM are covered in Chapter 3 along with the description of the methods used for analysing the data obtained from DEM simulations. In Chapter 4, an in-house DEM code is used in pebble packing simulations of a full size annular reactor core geometry. The effect of various parameters on the final packing density of the compacted pebble bed is studied and selected pebble beds are further analysed at various spatial scales to extract data of the local variations in the packing density. Chapter 5 describes how Monte Carlo reactor physics calculations of pebble beds are enhanced by using realistic pebble bed configurations produced in DEM simulations. In Chapter 6 a method is developed and implemented as a MATLAB code to map discrete pebble bed data to the continuum volume elements of thermal-hydraulics models. A summary and conclusions of the first part of the thesis is given in Chapter 7. Background and literature review related to the second part of the thesis are given in Chapter 8 along with the description of the related experiments. Chapter 9 covers the models and methods relevant for the CFD calculations in this work. The calculation models for the CFD calculations of the smooth and rough surface heated rod geometries are described in Chapter 10. The results of the CFD calculations are presented in Chapter 11 with comparison to experimental results. A summary and conclusions of the second part is given in Chapter 12. Finally, some concluding words regarding the whole thesis are given in Chapter 13.

Scientific contribution of the thesis

- Knowledge was gained on producing and analysing randomly packed pebble beds of various packing densities for subsequent reactor physics and thermal-hydraulics calculations. The possibility to produce stochastic pebble beds with very low and very high packing densities provides a way to introduce conservatism for the otherwise realistic "best estimate" calculation models.
- Knowledge was gained regarding the local packing density variations in a full size annular PBR geometry. Suggestions for taking these variations into account in thermal-hydraulic analyses of PBRs were given.
- Comparisons of the results obtained from DEM packing analyses with experimental results found from literature contributed to the validation of an in-house DEM code.

- A new approach was developed to enhance Monte Carlo reactor physics analyses of pebble bed geometries by producing realistic stochastic pebble bed configurations in DEM simulations. With this approach two typical issues encountered in Monte Carlo calculations of pebble beds can be avoided.
- A novel method was developed and implemented as a MATLAB code to transfer detailed three dimensional pebble bed data obtained from DEM and reactor physics simulations accurately to thermal-hydraulic continuum models. The method can also be used to investigate the packing structure of numerical sphere packings in general.
- The PBR related work forms a major contribution to the development of a unique calculation system where DEM is used to provide pebble packing data for the coupled Monte Carlo reactor physics and porous media thermal-hydraulics models.
- Knowledge was gained regarding the adequacy of different turbulence models for the prediction of the flow and heat transfer in three dimensional smooth and rib roughened GFR fuel rod geometries. Suggestions for future work were given.
- Knowledge was gained of the requirements and issues related to the three dimensional CFD modelling of the investigated gas cooled rod geometries and of the relevance of different heat transfer mechanisms.

From the experience gained during the work the following general recommendations are given for experimental work intended for the validation of numerical models.

- Viewpoints of numerical modelling should be included in the planning of experiments to ease the challenging model construction and simulation and to avoid introducing additional sources of uncertainties.
- Multi-physical aspects in experiments should be considered and documented in a reasonable detail to facilitate the use of advanced calculation approaches.

Additional notes about the author's contribution

- The in-house DEM code used in the work described in Chapter 4 was not programmed by the author of this thesis, although the author did minor modifications to its original source code.
- The Monte Carlo reactor physics simulations mentioned in Chapters 5 and 6 were not done by the author of this thesis.
- The thermal-hydraulic calculations mentioned in Chapter 6 were done by the author of this thesis.

This thesis is written as a monograph and it contains both published and unpublished work. The articles related to this monograph are listed below.

Peer reviewed articles with major contribution by the author

Suikkanen, H., Ritvanen, J., Jalali, P., and Kyrki-Rajamäki, R. (2014). Discrete element modelling of pebble packing in pebble bed reactors. *Nuclear Engineering and Design*, 273:24–32.

Rintala, V., Suikkanen, H., Leppänen, J., and Kyrki-Rajamäki, R. (2014). Modelling of realistic pebble bed reactor geometries using the Serpent Monte Carlo code. *Annals of Nuclear Energy*, Accepted.

Gómez, R., Buchholz, S., and Suikkanen, H. (2014). Experimental and numerical investigation of heat transfer and pressure drop for innovative gas cooled systems. *Nuclear Engineering and Design*, revised and resubmitted after minor comments.

Suikkanen, H., Rintala, V., and Kyrki-Rajamäki, R. (2014). Development of a coupled multi-physics code system for pebble bed reactor core modeling. In *Proceedings of HTR 2014, Weihai, China, October 27–31, 2014*.

Suikkanen, H., Rintala, V., and Kyrki-Rajamäki, R. (2010). An approach for detailed reactor physics modelling of randomly packed pebble beds. In *Proceedings of HTR 2010, Prague, Czech Republic, October 18–20, 2010*.

Related articles with minor contribution by the author or no peer review practice

Suikkanen, H., and Kyrki-Rajamäki, R. (2014). Validation of RANS CFD models for gas cooled fuel rod analyses. In *THINS 2014 International Workshop, Modena, Italy, January 20–22, 2014*.

Suikkanen, H., and Kyrki-Rajamäki, R. (2013). RANS calculations of L-STAR/SL gas cooled smooth rod experiments. In *THINS 2nd Cluster Workshop, Stockholm, Sweden, February 5–7, 2013*.

Suikkanen, H., Ritvanen, J., Jalali, P., and Kyrki-Rajamäki, R. (2012). Modeling packing of spherical fuel elements in pebble bed reactors using DEM. In *The Proceedings of the International Symposium on Discrete Element Modelling of Particulate Media held at the University of Birmingham on 29–30 March 2012*.

Roelofs, F., Shams, A., Hering, W., Otic, I., Papukchiev, A., Lathouwers, D., Pavlidis, D., Suikkanen, H., Hassan, Y., Barth, T., Niceno, B., and Cheng, X. (2012). HTR related activities within the European Thermal-Hydraulics for Innovative Nuclear Systems (THINS) project. In *Proceedings of 6th International Topical Meeting on High Temperature Reactor Technology HTR2012, Miraikan, Tokyo, Japan, October 28 – November 1, 2012*.

Kyrki-Rajamäki, R., Salomaa, R., Vanttola, T., Suikkanen, H., Viitanen, T., Penttilä, S., and Kangas, P. (2009). The Finnish Sustainable Energy (SusEn) project on New Type Nuclear Reactors (NETNUC). In *Proceedings of 20th International Conference on Structural Mechanics in Reactor Technology (SMiRT 20), Espoo, Finland, August 9–14, 2009*.

Part I

DEM modelling for gas cooled pebble bed reactors

2 Background and state of art

The first part of this thesis documents the work that was done to establish a framework for physically realistic simulation of pebble packing in PBRs and the subsequent utilisation of the result data in reactor physics and thermal-hydraulics analyses.

There are several methods and algorithms available for the generation of dense sphere packings. Some of them are based only on geometric parameters or might include some simplified physical models (see, e.g., work by Jodrey and Tory (1985) or Visscher and Bolsterli (1972)). Such algorithms can be used for generating random packings with a minimal computational effort. Depending on the purpose for which they are needed it might be important to verify that the packings actually have physically realistic packing structures. This type of algorithms also have a limited applicability and cannot be used for further dynamic analyses such as for simulating granular flow. Methods in which the actual contact physics of the spheres are solved and the trajectories of the individual spheres are tracked in a Lagrangian reference frame are computationally more demanding but also more versatile and physically realistic. There are basically two approaches for contact modelling in such methods, either treat the spheres as hard spheres which do not overlap each other, or as soft spheres which can overlap (Allen and Tildesley, 1987). The hard sphere model is typically used in simulations of gases as it is more suited for dilute systems. For dense systems, such as a packed bed of spheres in PBRs the soft sphere approach is more suitable. The term discrete element method (DEM) basically covers both simulation approaches but is usually used to refer to the soft sphere approach.

DEM was preferred in this work over simpler sphere packing methods because of its versatility and capabilities to model the actual packing process and dynamic behaviour of the pebbles. The main objective of the pebble packing studies in this work was to be able to produce realistic pebble bed configurations that can be utilised in further reactor physics and thermal-hydraulics analyses. Eventually the objective is to build a coupled code system for full reactor core analyses, where DEM simulations provide pebble bed packing data for a Monte Carlo method based reactor physics code and a thermal-hydraulic code employing the porous medium approach for the pebble bed. The reactor physics and thermal-hydraulics codes then exchange power and temperature data in iterations between each other until a converged solution is obtained.

It is important to have a sufficient understanding of the method to be able to use the simulation tools in a valid and efficient way. Also it is good to establish proper methods to analyse the data resulting from the simulations. These important prerequisites are covered first in Chapter 3. The next natural step is to move into practice. An in-house DEM code was used in pebble packing studies of a full size pebble bed reactor geometry. The effect of various parameters on the average packing density of the resulting pebble bed was studied and some of the result pebble beds were investigated in detail to extract packing structure details at various spatial scales. Also, comparisons to available experimental data were made. In the work

presented in Chapter 5, reactor physics analyses were enhanced by producing realistic pebble bed configurations to be used directly in a Monte Carlo method based criticality calculations. Finally, a description with examples is given of a method that was developed to map discrete pebble packing data to the volume elements of thermal-hydraulic continuum models. As a whole, these efforts cover a major part of the work towards the above mentioned coupled multi-physics calculation system.

2.1 A brief review of related work

Experimental work on granular flow related to pebble beds was done by Kadak and Bazant (2004) for a PBR design with a dynamic centre reflector formed of graphite pebbles. They did pebble flow experiments in a scaled-down facility using small plastic beads to represent the pebbles and studied the streamlines of the pebble flow and the mixing of the moderator and fuel pebbles. In their experiments they used a half model and a full three-dimensional model. Similar experimental work was also done by other investigators, for example Li et al. (2009), Jiang et al. (2012) and Yang et al. (2012) along with DEM computer simulations to compare experiments with and provide complementing data. Pebble flow simulations with DEM was also done before by Rycroft et al. (2006), who studied the pebble flow in a full scale reactor geometry with a dynamic centre reflector formed of moderator pebbles. Later on, Li and Ji (2013) did also DEM simulations on pebble flow coupled with fluid flow calculations.

Either commercial or freely available general purpose DEM codes have been used by most investigators. However, Cogliati and Ougouag (2006) developed the DEM code PEBBLES specifically for PBR related analyses. It was used for simulating the pebble packing and flow in the Chinese test reactor HTR-10 and the South African PBMR-400 reactor designs. Earthquake simulations were also performed with PEBBLES where DEM results were utilised in a transient neutronics analysis (Ougouag and Cogliati, 2007; Ougouag et al., 2009). Use of DEM simulation for studying loads on the solid centre reflector during an earthquake was also reported by Keppler (2013) who used the EDEM software. The DEM code PEBBLES was also used in simulations where the amount of dust produced in the German AVR was estimated by using DEM together with wear models (Cogliati and Ougouag, 2008). Dust generation related DEM analyses were also done by Rycroft et al. (2012) as scaling studies to give recommendations for designing an experimental facility for graphite dust experiments.

During the development of the South African PBMR, DEM was used to produce data for structural, thermal-hydraulic and neutronics models, for pebble packing and flow analyses and for estimating the loads caused by the pebble bed on the centre reflector blocks (Mitchell and Polson, 2007; Venter and Mitchell, 2007).

Methods to generate packed pebble beds were surveyed by Ougouag et al. (2005) and Auwerda et al. (2010). DEM is a highly accurate method as it is based on physical models. Due to this, it is also computationally a very expensive method for generating dense packed beds. There are also simpler algorithms for generating

packed beds that are based only on geometrical parameters or simplified physical models such as the one developed by Li and Ji (2012) for the fast generation of packed pebble beds.

du Toit (2002, 2006, 2008) did extensive work to study the packing characteristics of numerical pebble beds. He presented methods for analysing the radial and axial porosity variations in annular pebble beds, analysed the the packing structure variations of physical and numerical packed beds and compared them with literature correlations. He came to the conclusion that the packed beds obtained using DEM can be considered as acceptable representations of real packed beds. Recently, Auwerda et al. (2013) presented results of packing fraction measurements done with gamma ray scanning together with comparisons to computationally generated pebble beds.

Related to the utilisation of DEM results directly in Monte Carlo reactor physics analyses of pebble beds, surprisingly not a single published work could be found. Although, for example Monte Carlo code MCNP has capabilities to model stochastic geometries, which has been demonstrated with pebble bed calculations by Abedi and Vosoughi (2012), the pebbles were packed with an algorithm that does not simulate the physical packing process. However, Forestier et al. (2008) reported pebble bed criticality calculations performed with the Monte Carlo code MORET where the stochastic pebble bed was produced with a dynamic packing method apparently similar to DEM, although the details of the method were not explained in detail.

3 Methods for discrete element simulation and data analysis

Discrete element method (DEM), sometimes referred as distinct element method (Cundall and Strack, 1979), is a numerical method used to solve interactions between individually defined bodies, typically spheres. The method can be considered to be a sub-category of molecular dynamics (Allen and Tildesley, 1987). In DEM the spheres are typically regarded to be soft so that they can overlap each other. The overlap distance then represents the deformation between the spheres which is the parameter that is used to formulate contact forces. The contact force models and numerical methods behind DEM as well as methods for analysing simulation results are introduced below in the extent relevant to this work.

3.1 Contact of two spheres

A few useful parameters are defined as preliminaries before introducing the specific contact force models.

Two spheres i and j are in mechanical contact with each other if

$$\delta_{nij} = R_i + R_j - |\mathbf{r}_i - \mathbf{r}_j| > 0, \quad (3.1)$$

where δ_n is the normal overlap distance, R is the radius of a sphere and \mathbf{r} is the position vector. The normal unit vector between the spheres is

$$\mathbf{n}_{ij} = \frac{\mathbf{r}_j - \mathbf{r}_i}{|\mathbf{r}_j - \mathbf{r}_i|} \quad (3.2)$$

and their relative velocity is

$$\mathbf{v}_{rij} = \mathbf{v}_j - \mathbf{v}_i. \quad (3.3)$$

The slip velocity at the contact point can be calculated from

$$\mathbf{v}_{sij} = \mathbf{v}_{rij} - (\mathbf{v}_{rij} \cdot \mathbf{n}_{ij}) \mathbf{n}_{ij} + (R_i \boldsymbol{\omega}_i + R_j \boldsymbol{\omega}_j) \times \mathbf{n}_{ij}, \quad (3.4)$$

where $\boldsymbol{\omega}$ is the angular velocity of a sphere. A tangential unit vector can then be calculated with the slip velocity as

$$\mathbf{t}_{ij} = \frac{\mathbf{v}_{sij}}{|\mathbf{v}_{sij}|}. \quad (3.5)$$

Considering that the spheres can have different sizes and material properties it is useful to define effective parameters for the sphere pair. The effective radius R_{eff} and mass m_{eff} of a sphere pair are

$$R_{\text{eff}} = \frac{R_i R_j}{R_i + R_j}, \quad (3.6)$$

$$m_{\text{eff}} = \frac{m_i m_j}{m_i + m_j}. \quad (3.7)$$

3.2 Contact force models

When the two spheres i and j are in contact with each other the force between them consists of a normal and a tangential component

$$\mathbf{F}_{ij} = \mathbf{F}_{nij} + \mathbf{F}_{tij}. \quad (3.8)$$

In general, the contact forces in DEM are formulated using spring, dash-pot and slider components. The contact force models are shown in Figure 3.1. The spring and dash-pot represent the elasticity and viscosity of the material, respectively. The slider component in the tangential force model represents the friction between surfaces. The parameters in Figure 3.1 are the stiffness k , the damping coefficient η and the friction coefficient μ_f .

A simple linear spring and dash-pot model can be formed as

$$m\ddot{x} + \eta\dot{x} + kx = 0. \quad (3.9)$$

Other models have been formulated, for example, by Walton and Braun (1986). In their model different stiffnesses for the spring component in the normal contact are used depending on whether the spheres are moving towards or away from each other.

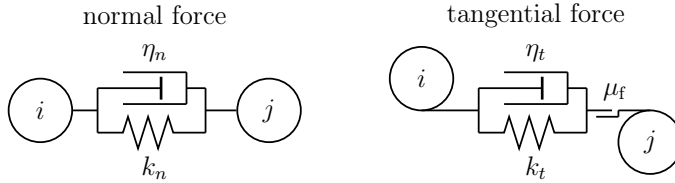


Figure 3.1: Contact force model based on a spring, a dash-pot and a slider.

3.2.1 Normal force

The preferred force model in this work is the nonlinear model proposed by Tsuji et al. (1992). Equation 3.9 can be reformulated using the previously defined parameters. A linear normal force on sphere i is then given by

$$\mathbf{F}_n = -k_n \delta_{nij} \mathbf{n}_{ij} - \eta_n (\mathbf{v}_{rij} \cdot \mathbf{n}_{ij}) \mathbf{n}_{ij}. \quad (3.10)$$

The elastic part can be replaced with a non-linear force deformation relation based on the contact theory by Hertz (1881) when the material parameters are known. The damping part can be calculated using the model proposed by Tsuji et al. (1992). The normal force then becomes

$$\mathbf{F}_n = -k_n \sqrt{R_{\text{eff}}} \delta_{nij}^{3/2} \mathbf{n}_{ij} - \eta_n \delta_{nij}^{1/4} (\mathbf{v}_{rij} \cdot \mathbf{n}_{ij}) \mathbf{n}_{ij}, \quad (3.11)$$

where the normal stiffness is calculated based on the material parameters E and ν denoting Young's modulus and Poisson's ratio, respectively. The normal stiffness can be obtained from (Pöschel and Schwager, 2005)

$$k_n = \frac{4}{3} \frac{E_i E_j}{E_i (1 - \nu_j^2) + E_j (1 - \nu_i^2)} \quad (3.12)$$

and the damping coefficient from (Tsuji et al., 1992; Antypov and Elliott, 2011)

$$\eta_n = \frac{\sqrt{5} \ln(e)}{\sqrt{\ln^2(e) + \pi^2}} \sqrt{m_{\text{eff}} k_n R_{\text{eff}}^{\frac{1}{4}}}, \quad (3.13)$$

where e is the restitution coefficient. The coefficient of restitution is typically given a constant value, although in reality it is a function of the impact velocity (Lun and Savage, 1986).

3.2.2 Tangential force

The tangential force on sphere i is given by (Tsuji et al., 1992)

$$\mathbf{F}_t = -k_t \boldsymbol{\delta}_{tij} - \eta_t \mathbf{v}_{sij}. \quad (3.14)$$

However, if the following criterion is satisfied,

$$|\mathbf{F}_t| > \mu_f |\mathbf{F}_n|, \quad (3.15)$$

meaning that the spheres are sliding, the tangential force is calculated as

$$\mathbf{F}_t = -\mu_f |\mathbf{F}_n| \mathbf{t}_{ij}. \quad (3.16)$$

When the tangential force is calculated with Equation 3.14 the tangential stiffness is given by (Tsuji et al., 1992)

$$k_t = 8G_{\text{eff}} \sqrt{R_{\text{eff}} \delta_{nij}}, \quad (3.17)$$

where G_{eff} is the effective shear modulus given by

$$G_{\text{eff}} = \frac{E_i E_j}{2E_j (2 - \nu_i) (1 + \nu_i) + 2E_i (2 - \nu_j) (1 + \nu_j)}. \quad (3.18)$$

The tangential damping coefficient can be assumed identical with the normal damping coefficient as suggested by Tsuji et al. (1992).

3.2.3 Force summation

After the contact forces between all sphere pairs have been resolved, the total force and torque on each sphere are calculated. For the sphere i the total contact force is

$$\mathbf{F}_{i,\text{tot}} = \sum_{j=1}^N \mathbf{F}_{ij}, \quad (3.19)$$

where N is the number of spheres in contact with the sphere i . Similarly, the contact torque on the sphere i is calculated as

$$\mathbf{T}_{i,\text{tot}} = \sum_{j=1}^N (R_i \mathbf{n}_{ij} \times \mathbf{F}_{tij}). \quad (3.20)$$

The translational acceleration of the sphere i can then be solved from

$$\mathbf{a}_i = \frac{\mathbf{F}_{i,\text{tot}}}{m_i} + \mathbf{g}, \quad (3.21)$$

which includes the gravitational acceleration \mathbf{g} . The angular acceleration is given by

$$\boldsymbol{\alpha}_i = \frac{\mathbf{T}_{i,\text{tot}}}{I_i}, \quad (3.22)$$

where I is the moment of inertia, which in the case of a sphere is

$$I = \frac{2mR^2}{5}. \quad (3.23)$$

3.3 Time integration and simulation time step

A typical DEM simulation progresses with explicitly set constant time intervals. There are various time integration methods that can be used to progress the simulation (Kruggel-Emden et al., 2008). First order accurate forward Euler integration is the simplest option. With this integration method the position of a sphere at the next time step ($t + \Delta t$) is calculated simply as (Kruggel-Emden et al., 2008)

$$\mathbf{r}_i(t + \Delta t) = \mathbf{r}_i(t) + \mathbf{v}_i(t)\Delta t \quad (3.24)$$

and the velocity as

$$\mathbf{v}_i(t + \Delta t) = \mathbf{v}_i(t) + \mathbf{a}_i(t)\Delta t, \quad (3.25)$$

where t is the time.

A more accurate and stable integration method is, for example, the velocity Verlet algorithm. With this algorithm the position and velocity are given by (Martys and Mountain, 1999)

$$\mathbf{r}_i(t + \Delta t) = \mathbf{r}_i(t) + \mathbf{v}_i(t)\Delta t + \frac{1}{2}\mathbf{a}_i(t)(\Delta t)^2 \quad (3.26)$$

and

$$\mathbf{v}_i(t + \Delta t) = \mathbf{v}_i(t) + \frac{\mathbf{a}_i(t) + \mathbf{a}_i(t + \Delta t)}{2} \Delta t. \quad (3.27)$$

The simulation time step needs to be small enough to capture all relevant physics but as large as possible for computational efficiency. Because the contact force is formulated using the overlap between the spheres, a too large time step would lead to unrealistic contact forces as the pebbles could move too much within each other in a single time step. The contact time for two elastic spheres can be derived from the energy balance of the collision as (Landau and Lifshitz, 1986)

$$t_{\text{tot}} = 2.87 \left(\frac{m_{\text{eff}}^2}{R_{\text{eff}} E_{\text{eff}}^2 v_r} \right)^{\frac{1}{5}}, \quad (3.28)$$

where

$$E_{\text{eff}} = \left(\frac{1 - \nu_i^2}{E_i} + \frac{1 - \nu_j^2}{E_j} \right)^{-1}. \quad (3.29)$$

The simulation time step then needs to be a small fraction of the total contact time. As t_{tot} is dependent on the relative collision velocity v_r the time step needs to be estimated based on the maximum expected velocity between spheres during the simulation.

Another requirement for the simulation time step is related to the speed of energy transfer in the system. Energy must not be transmitted faster in the simulation than it would be transmitted in reality (Li et al., 2005). In DEM the dynamics of a system consisting of multiple spheres is approximated with multiple simultaneous pairwise interactions. This requires that the simulation time step is small enough so that the displacement induced stresses cannot propagate further than to the spheres in direct contact with each other (Vargas and McCarthy, 2001). Typically in DEM simulations it is assumed that all of the energy is transferred by Rayleigh waves and the critical time step based on the propagation of Rayleigh waves is given by

$$\Delta t_c = \frac{\pi R_{\text{eff}}}{0.8766 + 0.163\nu} \sqrt{\frac{\rho}{G}}, \quad (3.30)$$

where ρ is the density of the material (Li et al., 2005).

The time step used in DEM simulations should be decided based on both of the above constraints. In practice, a maximum value for v_r can be estimated based on the type of simulation (e.g. dropping spheres) and then later verified from the simulation output. As the other parameters are defined before the simulation, the contact time and Rayleigh critical time can be calculated and the smaller of these selected as the determinative constraint. It is then typical to use a simulation time step in the order of 10 % of the determinative time (see, e.g., Li et al. (2005)).

3.4 Data analysis methods

The packing density or packing fraction ϕ and its opposite parameter porosity $\varepsilon = 1 - \phi$ are the parameters of interest in this work. Other parameters, such as the

coordination number, characterising sphere packings are not investigated in the context of this work. Below, data analysis methods are established to analyse the packing density of numerical pebble beds at various spatial scales ranging from the average packing density of the whole pebble bed to the packing fraction of an individual pebble.

3.4.1 Average packing density

The average packing density $\bar{\phi}$ is calculated as the ratio of the solid volume of pebbles and the total volume they are enclosed inside. The average packing density reveals how densely packed the pebble bed is in general but does not give any information regarding local packing density variations.

3.4.2 Area based packing density profiles

Profiles of packing density variations along different coordinate axis directions can be formed to extract more detailed information of a packed bed. In a Cartesian coordinate system it is rather straightforward to form cutting planes at regular intervals along a coordinate axis direction, for example x , so that the plane sphere intersection areas (circles) are calculated and summed together to give the total solid area. The area of the solids is then divided by the total area to obtain the area based packing density at the current position as

$$\phi_A(x) = \sum_i \frac{A_i(x)}{A_{\text{tot}}(x)}, \quad (3.31)$$

where the summation is taken over all pebbles i which intersect with the current plane located at x . A_i is the intersection area of the pebble i and the cutting plane and A_{tot} is the total surface area of the cutting plane inside the container.

As the typical container geometry of pebble beds is cylindrical the packing density profiles need to be calculated also in the radial direction of the cylindrical coordinate system. In cylindrical geometries, packing density profiles in the radial coordinate direction can be extracted with a method presented by Mueller (2010). Several concentric cutting cylinders are formed with radii r inside the container. In this case intersection areas between spheres and cylinders are calculated. In this work, the radial profiles are formed only for annular geometries and thus the integral equation presented by Mueller (2010) to calculate the intersection areas can be simplified to

$$A_i(r) = 4 \int_{\frac{r_i^2 + r^2 - R_i^2}{2r_i}}^r \sqrt{\frac{R_i^2 - r^2 + 2xr_i - r_i^2}{r^2 - x^2}} r dx, \quad (3.32)$$

which can be solved numerically.

When interpreting the area based packing density profiles it should be noted that they represent areal densities which can be significantly higher than the maximum

volumetric packing density of $\pi/\sqrt{18} = 0.74048$ for mono-sized spheres. This is typically seen at the near wall regions where the packing is highly ordered. Area based profiles are, however, often used to analyse the packing structures in wall bounded packings and to compare with experimentally obtained results.

3.4.3 Local packing density

Packing densities at the scale of individual pebbles can be obtained by first forming a three-dimensional Voronoi decomposition (Voronoi, 1907) to the pebble bed and then dividing the pebble volume with the volume of the corresponding Voronoi polyhedron. A Voronoi polyhedron of a pebble consists of the volume that is closer to it than to any other pebble. An example of a Voronoi decomposition around pebbles is shown in Figure 3.2.

There are several code implementations for calculating Voronoi volumes. The open source software library Voropp by Rycroft (2009) is used in this work. In addition to normal Voronoi tessellation it is capable of forming the so called radical Voronoi tessellation which is essential if the packing consists of polydisperse spheres. In Voropp convex walls can be defined that cut the Voronoi volumes at the boundaries. For non-convex walls, such as the inner wall of the annular reactor core geometry, a specific technique utilising copied pebbles can be used to form the boundary where the Voronoi cells are cut (see Suikkanen et al. (2014b)).

The Voronoi decomposition method can be used for pebble scale packing fraction (denoted by ϕ_{vor}) analyses.

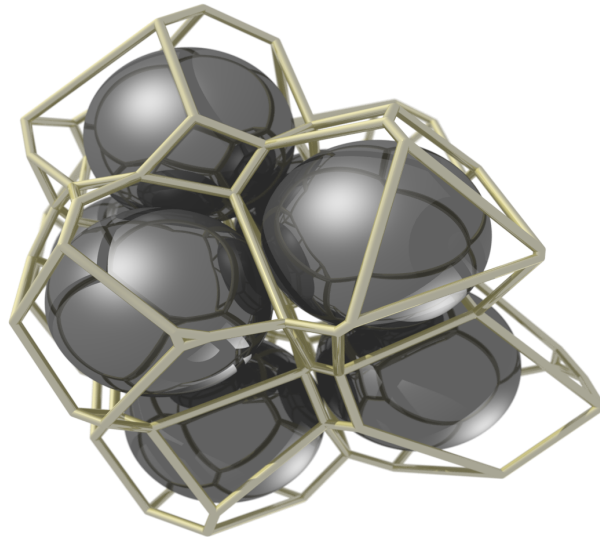


Figure 3.2: Spheres surrounded by their Voronoi tessellation.

4 Pebble packing studies for an annular reactor core geometry

DEM simulations were performed where selected parameters were varied to find out their effect on the packing density of the resulting pebble bed after compaction in the packing simulation. Main motivation in these studies was to gain experience on how to produce numerical pebble beds that have a pre-specified average packing density and also how to analyse them in more detail using the data analysis methods introduced in Chapter 3. Another objective was to test the performance of an in house DEM code, which was designed specifically for cylindrical pebble bed geometries.

The DEM simulations were done for an annular cylinder geometry representing a real size PBR core with a solid centre reflector. A total of 450,000 pebbles were compacted inside the geometry in the simulations. The investigated parameters included the friction and restitution coefficients and the packing density of the initial pebble column before it was collapsed inside the reactor geometry. In addition, the effect of pebble size distribution was studied. A comparison with available experimental data was also done to add confidence to the results obtained with the code. In addition to this thesis, this work has also been discussed in Suikkanen et al. (2014b).

Several DEM implementations exist from general purpose codes to highly specialised tools and from commercial closed source software to free to use open source codes. The DEM code used in these simulations is an in-house implementation of the method described in Chapter 3. It is written in C++ and parallelised using OpenMP directives to utilise multicore processors on a single computing node. The link cell neighbour search algorithm (see e.g. Pöschel and Schwager (2005)) in the code uses a cylindrical coordinate system making it more optimised for cylindrical geometries typical for PBRs.

4.1 Calculation model

An annular container geometry representing the core of the PBMR-400 reactor design (Venter and Mitchell, 2007) was defined with the inner and outer radii of the annulus having the dimensions specified for the real reactor geometry. The constant parameters and material properties used in the model are given in Table 4.1. Contrary to the real reactor geometry where the bottom of the core cavity would transform into narrow pipes for pebble outlet, a flat bottom plate was defined. There is no data openly available regarding the details of the bottom geometry and also the domain of interest in this work was the main core region. For the packing density analysis the bottom and also the top regions of the packings were excluded so that the obtained results represent the region unaffected by the bottom wall boundary and the free surface at the top of the pebble bed. This way the results are comparable between each other as exactly the same bed height is considered. The analysed

region starts from 10 pebble diameters and ends to 160 pebble diameters above the bottom plate.

The simulations were started with an initial dilute configuration inside the annulus generated with a random number generator algorithm. The initial column contained all of the pebbles and it was checked that no overlaps between them existed. In the DEM simulation the initial configuration of pebbles was collapsed due to gravitational force and the pebbles settled into a dense static packing. This packing method does not replicate the actual packing process that would be used to fill the reactor cavity but it was considered a suitable compromise between realism and computational effort. Dropping a huge number of pebbles individually from feed locations realistically would require prohibitively long simulations. Based on the time step requirements discussed in Chapter 3 a time step size of $5 \cdot 10^{-6}$ s was selected for the packing simulations.

The effect of the packing density of the initial configuration $\bar{\phi}_{\text{init}}$, the friction and restitution coefficients μ_f and e , respectively, and the pebble size distribution were investigated. The maximum initial packing density that was investigated was 0.25, which is already close to the densest packing that can be produced with the packing algorithm in a reasonable time. Friction and restitution coefficients were both varied from 0.01 to 0.99 and the same values were used between a pebble and a wall as between the pebbles. The restitution coefficient affects how much of the kinetic energy is conserved in contacts between the pebbles. In the final set of simulations the effect of the pebble size distribution was investigated in the range that should cover size differences arising from manufacturing tolerances. The same number of pebbles was used as in the other simulations but their radii was defined based on a mean value and a standard deviation σ so that the pebble radii were normally distributed. The mean value was the same radius that was used for the mono-sized pebbles and the standard deviation of R was varied from 0.01 mm to 1 mm. The list of values used for the variable parameters is given in Table 4.2. The base values which are in bold typeface were considered to represent somewhat realistic values for graphite pebbles. When one of the three parameters ($\bar{\phi}_{\text{init}}$, μ_f or e) was varied, the other two were kept at this base value.

Table 4.1: Parameters used in the DEM packing simulation.

Parameter	Symbol	Value
Container inner radius	R_{inner}	1.00 m
Container outer radius	R_{outer}	1.85 m
Number of pebbles	N	450,000
Pebble (mean) radius	R	30 mm
Pebble density	ρ	1,857 kg/m ³
Pebble Young's modulus	E	10 GPa
Pebble Poisson's ratio	ν	0.13

Table 4.2: Parameters varied in the packing simulations.

Constant radius		Normally distributed radius	
$\bar{\phi}_{\text{init}}$	μ_f	e	σ [mm]
0.10	0.01	0.01	0.01
0.15	0.05	0.10	0.10
0.20	0.10	0.20	1.00
0.25	0.20	0.30	
	0.30	0.40	
	0.40	0.50	
	0.50	0.60	
	0.60	0.70	
	0.70	0.80	
	0.80	0.90	
	0.90	0.95	
	0.99	0.99	

4.2 Packing simulation results

The packing simulations were run until the pebbles had formed a static column inside the annulus. The kinetic energy of the pebble system was monitored during the simulations to determine when a static state had been achieved. While the time needed to obtain a static packing was dependent on the investigated parameters, such as the restitution coefficient, roughly 5,000 CPU hours were required to obtain a static packing. The simulations were performed using various computer resources but mostly utilising 16 parallel tasks in a computer cluster with Intel Xeon E5-2660 processors.

4.2.1 Comparisons with experimental data

A comparison with experimental data was made to increase confidence in the results obtained with the in-house DEM implementation. Experimental results presented by du Toit (2008) were used as they are for the same annular geometry as was used in the simulations. The experiments PBR-1 and PBR-2 were performed in a scaled facility representing PBMR-400 core geometry using lead spheres. Radial packing density profiles were extracted with a method described by Goodling et al. (1983). The influence of the bottom boundary and the free surface at the top were excluded similarly as was done with the numerical pebble beds in this work. The results by du Toit (2008) were presented as porosities ε which were converted to packing densities by noting that $\phi = 1 - \varepsilon$.

Numerically obtained pebble beds with the same bulk packing densities, that is, average packing density between 5 and 9 pebble diameters in the radial direction, were selected for comparison. The radial packing density profiles resulting from the DEM simulations are compared with the experimental profiles in Figure 4.1. As can

be seen, the wall region oscillations are matching with a relatively good accuracy considering the scatter in the experimental data. The scatter is visible in the bulk region especially in the experiment PBR-1. According to du Toit (2008) the amount of scatter is within a typical range of the experimental method which was used to obtain the results.

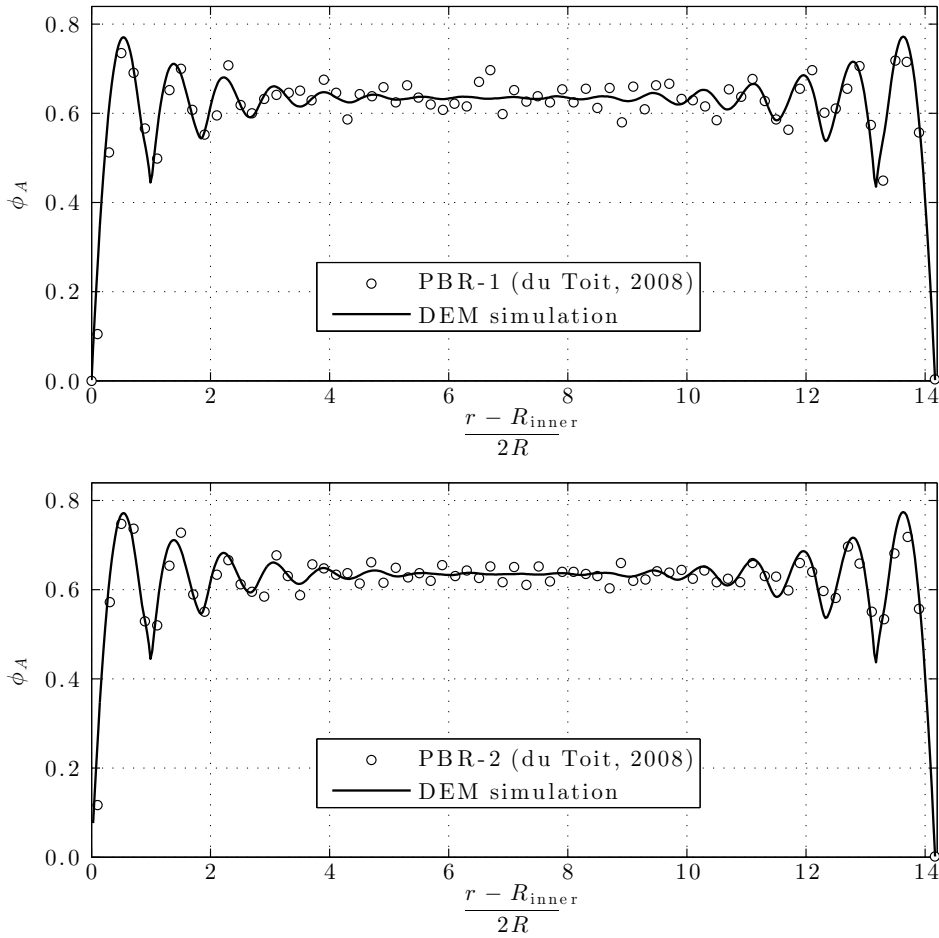


Figure 4.1: Comparison of radial packing density profiles of calculated pebble beds with experimental data by du Toit (2008) (Suikkanen et al., 2014b).

4.2.2 Average packing densities

The initial packing density of the pebble column had a small effect on the resulting pebble bed. With the most dilute initial configuration ($\bar{\phi}_{init} = 0.10$) the densest

packing of $\bar{\phi} = 0.630$ was obtained. When $\bar{\phi}_{\text{init}}$ was increased the packing density of the final pebble bed decreased slightly. Value of $\bar{\phi} = 0.628$ was obtained with the highest initial density $\bar{\phi}_{\text{init}} = 0.25$. The effect is explained by the potential energy difference between the initial states. The more dilute the initial configuration is, the higher the pebble column and its potential energy. However, the density difference is quite small and a longer simulation is needed for a higher column to settle.

Friction coefficient is affected by various things, such as the gas atmosphere and dust between the pebbles (Xiaowei et al., 2010). Thus it is a parameter that varies significantly between the contacts. The effect of friction coefficient to the packing density was examined between 0.01 and 0.99. The results are shown in Figure 4.2. It can be seen that with values higher than approximately 0.4 the friction coefficient does not have much effect on $\bar{\phi}$ and its value is approximately 0.628. However, below 0.4 when approaching zero friction, the packing density starts to increase as the pebbles slide between each other more easily. The maximum value of $\bar{\phi} = 0.632$ was obtained with $\mu_f = 0.01$. Although the friction coefficient has a relatively small effect when generating a static packing, it can be assumed to be a very important parameter when simulating the flow of pebbles as noted, for example, by Yang et al. (2012).

From the investigated parameters the restitution coefficient was found out to have the strongest effect on the resulting packing density. These results are also shown in Figure 4.2. The packing density varied from 0.620 obtained with a small value of $e = 0.01$, to 0.636 obtained with $e = 0.99$. When e is small the pebble bed stabilises faster resulting in a relatively dilute configuration. As e is increased the packing density increases steadily at first and then steeply when approaching $e = 1$.

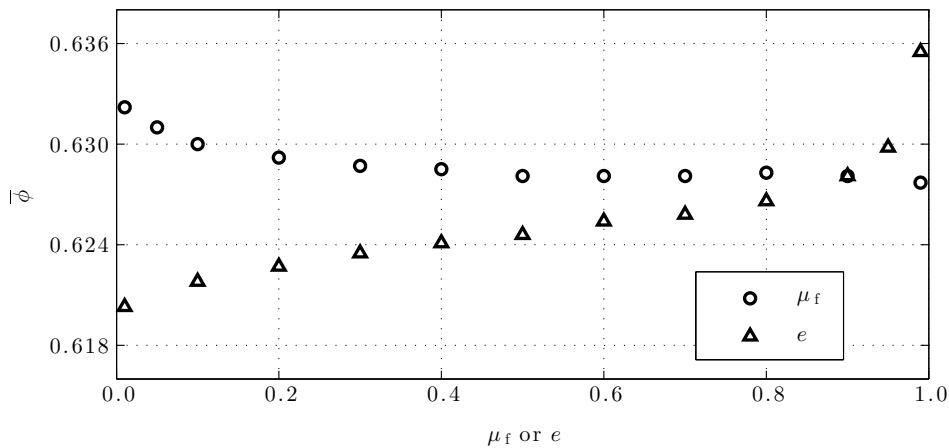


Figure 4.2: Effect of the friction and restitution coefficients to the average packing density.

The series of simulations that was run with pebbles having a size distribution did not result in any differences in the $\bar{\phi}$ until the standard deviation of R was increased to 1 mm. With standard deviation below 1 mm the resulting $\bar{\phi}$ was 0.628. With a standard deviation of 1 mm, $\bar{\phi} = 0.629$ was obtained. Thus, the small size differences that can be expected due to manufacturing tolerances of the pebbles would not seem to have much effect on the packing density.

The results show the effect of the investigated parameters on the packing density of the annular pebble bed when the packing is formed by collapsing an initial dilute configuration by gravity. The parameters, especially e can be tuned to result in a pebble bed with a desired average packing density. Based on the results obtained varying the friction and restitution coefficients, an additional packing was simulated with the aim of constructing a very dense packing. By using values of $\mu_f = 0.01$ and $e = 0.99$ a very dense packing with $\bar{\phi} = 0.638$ was obtained.

4.2.3 Local packing structures

Pebble beds with significantly different average packing densities were selected for a more detailed packing structure analysis. Pebble beds with $\bar{\phi} = 0.620$, $\bar{\phi} = 0.628$ and $\bar{\phi} = 0.636$ which correspond to cases with the varied values of $e = 0.01$, $\mu_f = 0.99$ and $e = 0.99$ (see Table 4.2), respectively, were selected.

Packing density variations in the radial direction were calculated using the area based method described in Chapter 3. The packing density profiles are shown in Figure 4.3 for the three selected pebble beds. First of all, one can observe the effect of the walls as oscillations propagating from five to six pebble diameters from the walls. As the total width of the annulus is only slightly over 14 pebble diameters, more than two thirds of the pebble bed thickness belong to the wall affected region. When comparing the profiles of the packings with different average densities between each other it can be seen that the amplitude of the oscillations increases as the average density increases. Also, the oscillations seem to propagate slightly further away from the walls in the case of high densities.

To investigate the packing structures of the pebble beds at the scale of individual pebbles, the Voronoi decomposition method described in Chapter 3 was used to extract local packing densities. The probability density functions showing the distribution of the Voronoi based packing fractions are plotted in Figure 4.4 and the result for the two extremes ($\bar{\phi} = 0.620$ and $\bar{\phi} = 0.636$) are visualised for a small region of pebbles in Figure 4.5. The increase in the average density can be seen as a shift towards right in the density function plot and as an increase of ordered or "crystallised" clusters of pebbles near the walls.

The data obtained from the Voronoi decomposition was also used to plot radially averaged packing density "maps" which show the variations in the axial z and circumferential θ directions and reveal more information about local densification. The maps were produced for the full packing (Figure 4.6) and for slices with a thickness of two pebble diameters for the centre region (Figure 4.7) and the inner (Figure 4.8) and outer (Figure 4.9) wall regions. The increase in $\bar{\phi}$ is seen as a general darkening

of the colour. Based on especially Figure 4.6, it seems that the most dilute pebble bed has a clear decrease in the packing density towards the top of the column while the other two pebble beds seem to be more homogeneous. Individual darker regions start to form into bigger clusters as $\bar{\phi}$ increases. These can be localised mostly into the near wall regions when looking at Figure 4.7, 4.8 and 4.9, as the centre regions appear to be relatively homogeneous. In general, the near wall regions are more dilute than the centre region but the local densifications are more pronounced.

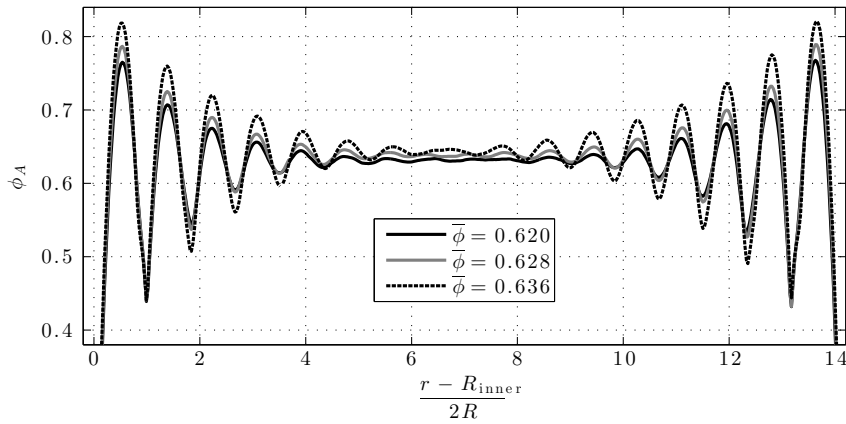


Figure 4.3: Area based radial packing density profiles for annular pebble beds with different average packing densities (Suikkanen et al., 2014b).

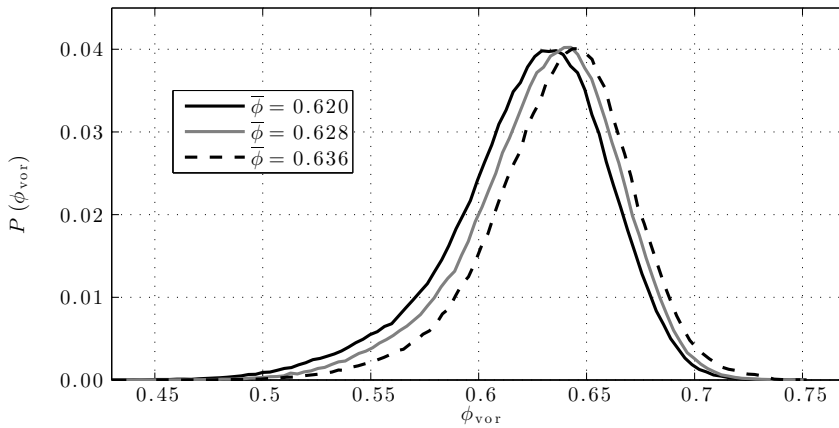


Figure 4.4: Probability density functions for three pebble beds with different average packing densities (Suikkanen et al., 2014b).

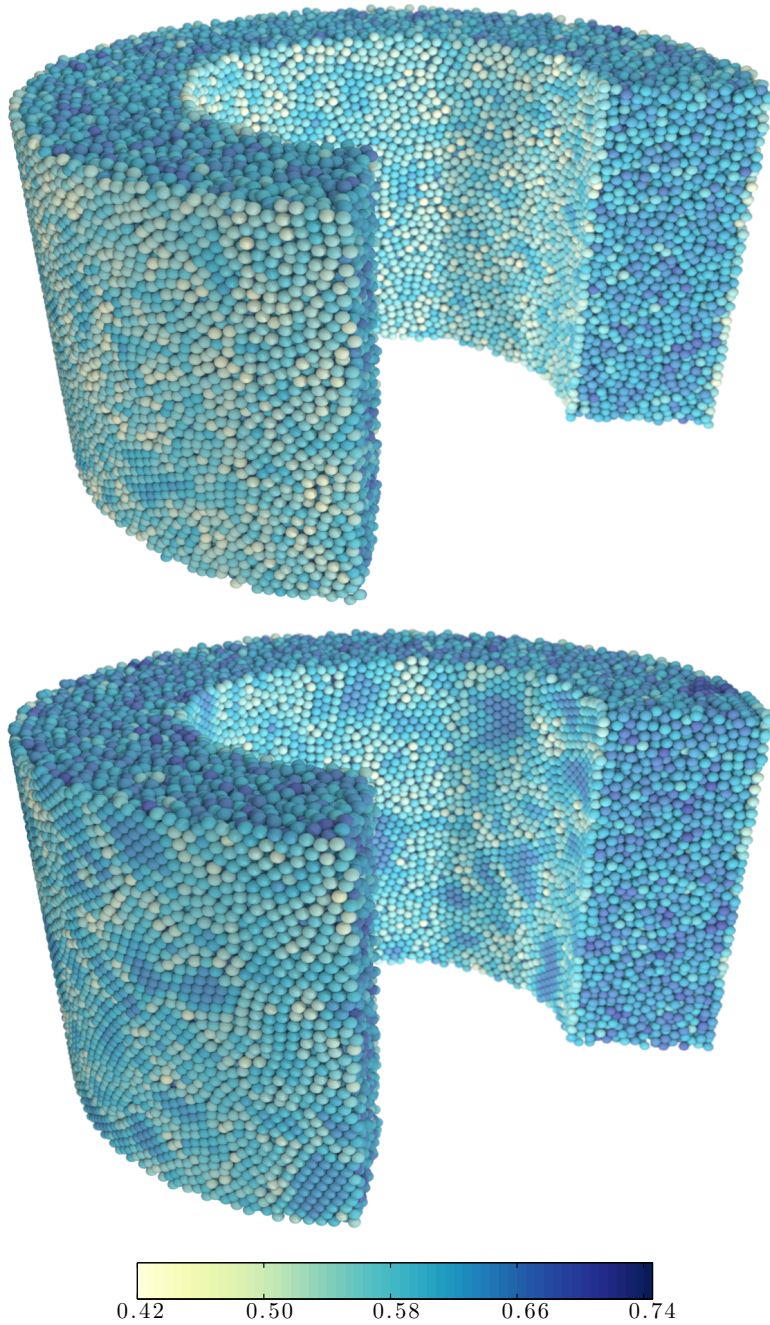


Figure 4.5: Small sections of the pebble beds with $\bar{\phi} = 0.620$ (top) and $\bar{\phi} = 0.636$ (bottom) with pebbles coloured by their local packing fractions obtained after a Voronoi decomposition.

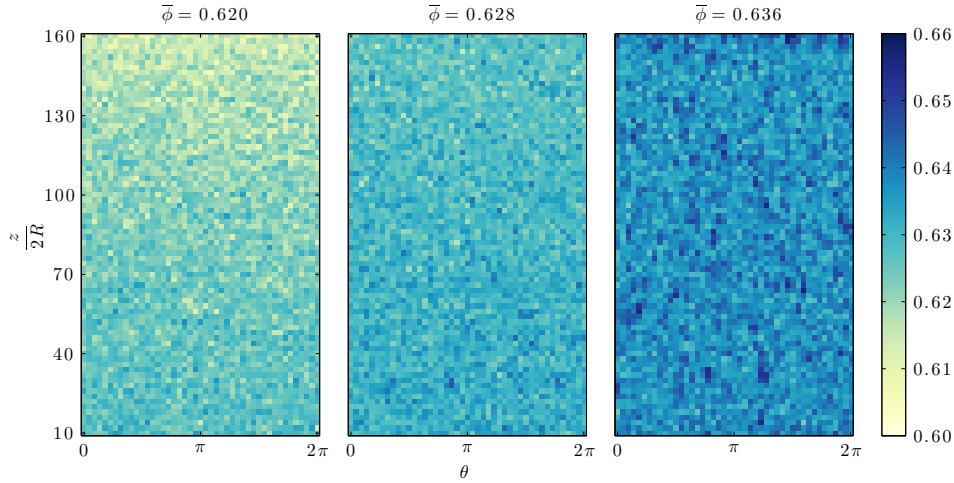


Figure 4.6: Radially averaged packing density maps for pebble beds with different average packing densities based on the pebble scale packing fractions obtained from Voronoi decomposition (Suikkanen et al., 2014b).

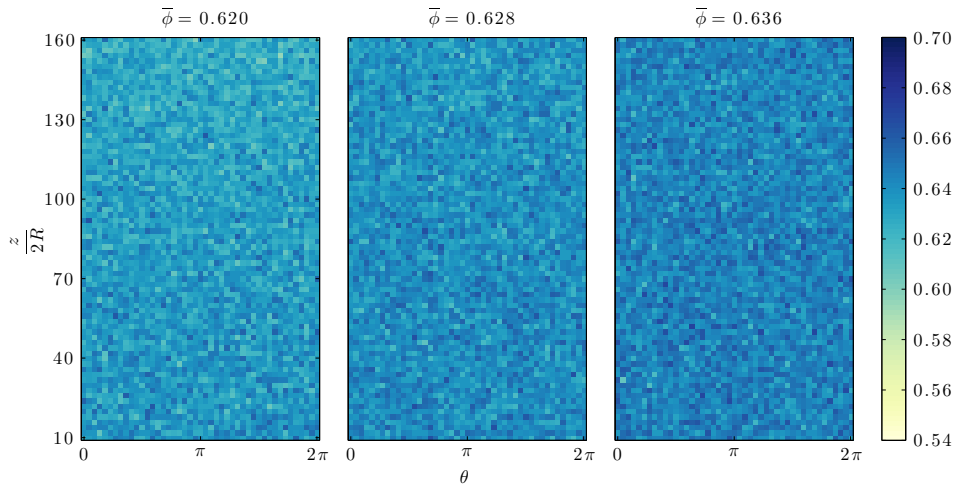


Figure 4.7: Radially averaged packing density maps for pebble beds with different average packing densities based on the pebble scale packing fractions obtained from Voronoi decomposition (Suikkanen et al., 2014b). Data of a slice with a thickness of $4R$ extracted from the centre of the annulus.

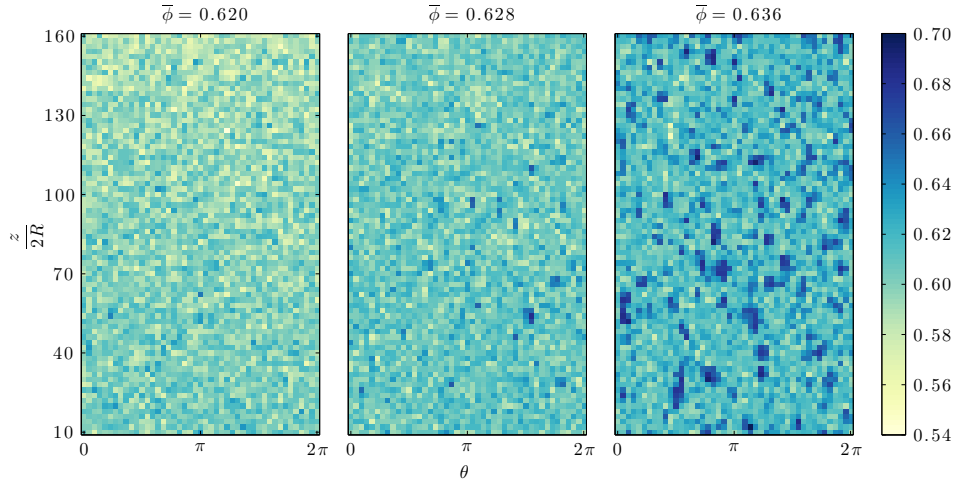


Figure 4.8: Radially averaged packing density maps for pebble beds with different average packing densities based on the pebble scale packing fractions obtained from Voronoi decomposition (Suikkanen et al., 2014b). Data of a slice with a thickness of $4R$ extracted from the annulus inner wall region.

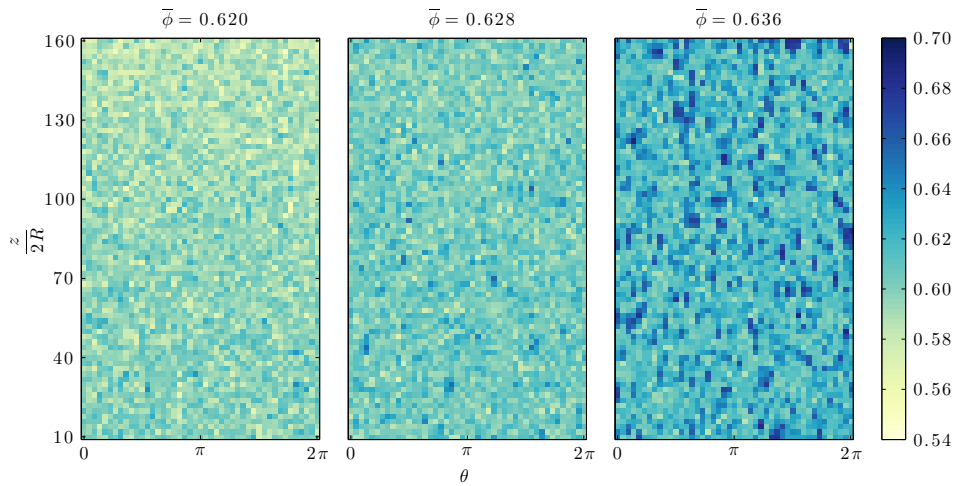


Figure 4.9: Radially averaged packing density maps for pebble beds with different average packing densities based on the pebble scale packing fractions obtained from Voronoi decomposition (Suikkanen et al., 2014b). Data of a slice with a thickness of $4R$ extracted from the annulus outer wall region.

5 Enhancing neutronics analyses with realistic pebble packing data

Packed pebble beds obtained from DEM simulations were used to demonstrate the stochastic geometry capabilities of the reactor physics code Serpent, especially for PBR calculations. Serpent is a continuous energy Monte Carlo code developed at VTT Technical Research Centre of Finland with specific features that make it especially well suited for pebble bed calculations (Leppänen, 2007).

One major advantage of Monte Carlo method based reactor physics codes over deterministic ones is the possibility to define the calculation model geometry in a very high level of detail. In addition, the method scales efficiently for parallel computation. With the increase in computational power and availability of parallel computing it has become a very attractive method for PBR related analyses, where the geometrical details range from the millimetre scale coated particles randomly dispersed inside the fuel pebbles to the scale of the reactor core where the pebbles are as well in a random configuration. In Monte Carlo models it is possible to define this full scale of geometric details. However, due to the enormous number of geometric entities, the fuel particles inside the pebbles and the pebbles inside the core have traditionally been defined in regular lattice configurations to have an adequate computational performance for the neutron tracking. Even experiments have been done in the past with regularly stacked pebbles to allow direct comparison with calculations. As an example, Difilippo (2003) performed Monte Carlo calculations with the code MCNP of criticality experiments that were done in the PROTEUS facility for regularly stacked pebble beds.

The regular lattice approach, however, is an approximation of the real configuration. It does not include the effects of randomness in the calculations which can result in unrealistic neutron streaming effects (Lieberoth and Stojadinović, 1980) and typically results in clipping the particles/pebbles at the boundaries unrealistically. Various methods have been used to overcome these issues. To introduce stochasticity, methods have been developed such as the stochastic geometry model implemented into MCNP (Brown and Martin, 2004) where the regular lattice is retained but the geometry object inside is translated within the bounds of the lattice cell. Another approach is to sample fuel particles from a probability distribution during the transport of a neutron (Murata et al., 1997). A simple solution for the clipping issue is to leave the lattice cells intersecting with bounding surfaces empty (Şeker and Çolak, 2003). However, the recommended approach in Serpent is to define the stochastic positions of the fuel particles and the pebbles explicitly beforehand. Serpent uses specific methods, such as the Woodcock delta tracking (Leppänen, 2010) and a search mesh for fuel particles and pebbles (Rintala et al., 2014), which make the computational effort feasible despite the enormous number of individually defined geometrical entities.

Criticality experiments performed in the ASTRA facility in the Russian Research Center (RRC) Kurchatov Institute between 2003 and 2004 and documented by

Ponomarev-Stepnoi et al. (2008) were calculated with Serpent. Stochastic pebble bed configurations for the Serpent calculations were constructed with discrete element packing simulations. Because of the rather complicated container geometry with detector channels and a control rod channel inside the pebble bed, the in-house DEM code that was used in the work presented in Chapter 4 was not used due to its limitations in defining wall boundaries. Implementing the code with a more general wall definitions was not deemed worthwhile in this context. Rather, two different open source DEM codes were tested, namely ESyS-Particle and LIGGGHTS, both which support wall geometries constructed from triangles.

Packing simulations were first done with ESyS-Particle and the resulting pebble bed configurations were used as inputs in the Serpent calculations. However, as the packing simulations did not result in quite as dense packings as described for the experimental setup, the study was later revisited and new enhanced packing simulations were done with LIGGGHTS. The investigations performed using ESyS-Particle have been discussed also in Suikkanen et al. (2010) and the LIGGGHTS simulations in Rintala et al. (2014).

5.1 Discrete element simulation codes

ESyS-Particle (Abe et al., 2004), formerly known with the names Lattice Solid Model and LSMEarth, is a code developed at the Centre for Geoscience Computing at the University of Queensland. ESyS-particle has been developed for geo-scientific research and thus includes specific models, such as bonded particles, useful for rock fragmentation studies. The code can, however, be used also for sphere packing and flow simulations.

LIGGGHTS (LAMMPS improved for general granular and granular heat transfer simulations) (Kloss et al., 2012) is a DEM code built on top of the molecular dynamics code LAMMPS (Large-scale atomic/molecular massively parallel simulator) (Plimpton, 1995). LIGGGHTS is maintained by DCS Computing GmbH. The development of LIGGGHTS aims at improving the basic DEM simulation capabilities in LAMMPS to make it a suitable tool for industrial applications. Compared to ESyS-Particle the approach in LIGGGHTS development is more towards a general purpose DEM tool.

In addition to a more flexible definition of boundary wall geometries, the two open source DEM codes have several useful features and modelling capabilities that have not yet been implemented to the in-house DEM code used in Chapter 4. Both open source codes have domain decomposition based MPI (message passing interface) parallelisation while the in-house code has a shared memory parallelisation limiting the distribution of parallel tasks to a single multi-core computing node. With the MPI parallelisation ESyS-Particle and LIGGGHTS simulations can be distributed also between several nodes making their performance potential greater than that of the in-house DEM code. Both codes also come with several interaction laws and models and are thus more versatile tools for DEM simulations in general. This is especially true with LIGGGHTS as it is built on top of the widely used LAMMPS

molecular dynamics code and includes all its features and efficient algorithms. With a wider user and developer base they are also more extensively verified and validated than the in-house code.

5.2 ASTRA packing simulation models

The ASTRA facility used in the experiments at RRC consisted of a steel cylinder inside which graphite blocks were assembled to form bottom, side and centre reflector regions so that an octagonal annular cavity was formed (Ponomarev-Stepnoi et al., 2008). A variable number of pebbles were then poured inside the cavity depending on the experiment. Several small diameter metallic tubes were fixed inside the cavity between the pebbles for measurement instrumentation. One larger tube was also located inside the cavity to house a control rod. The wall geometry that was built for the DEM packing simulations is shown in Figure 5.1. It includes all the details of the experimental configuration, such as the instrumentation and control rod tubes. However, the projections on top of the bottom reflector graphite blocks were not included in the simulations with ESyS-Particle but were added to the later model used in the simulations with LIGGGHTS. For both DEM codes the wall geometry can be defined using interconnected triangles. For ESyS-Particle the wall geometry was constructed manually and written in the correct format into a file using MATLAB, while the LIGGGHTS geometry with the more complex bottom boundary was built using the Gambit meshing software by ANSYS Inc. and imported to LIGGGHTS in STL (stereolithography) format.

Ponomarev-Stepnoi et al. (2008) did not explain the details of the core loading process so it was assumed that the core was loaded by dropping the pebbles from some kind of feed tubes. Also the surface of the core was most likely flattened to get an even core height throughout the cavity. In the ESyS-Particle simulations the same packing method as described in Chapter 4 was used, that is, an initial dilute configuration of pebbles was sampled inside the geometry and let to compact due to the gravitational force. To get an even surface, more pebbles were initially compacted than in the actual critical configurations and a number of top pebbles was removed so that the number of remaining pebbles corresponded to that of the specific critical configuration. In the later simulations with LIGGGHTS it was decided to mimic a real loading process by dropping the pebbles from specified feed locations. Four inlet locations were defined in the north-east, south-east, south-west and north-west parts of the geometry from which pebbles were dropped into the cavity. It was, however, noticed that both packing methods produced slightly too high pebble beds, that is, too dilute packings, which would suggest that some additional measures were done in the experiments to achieve a denser packing than would result from simply dropping the pebbles from the top of the container. Regardless of the deviation from the core heights of the experimental configurations, the pebble beds obtained from the ESyS-Particle simulations were used in the subsequent Serpent calculations as such.

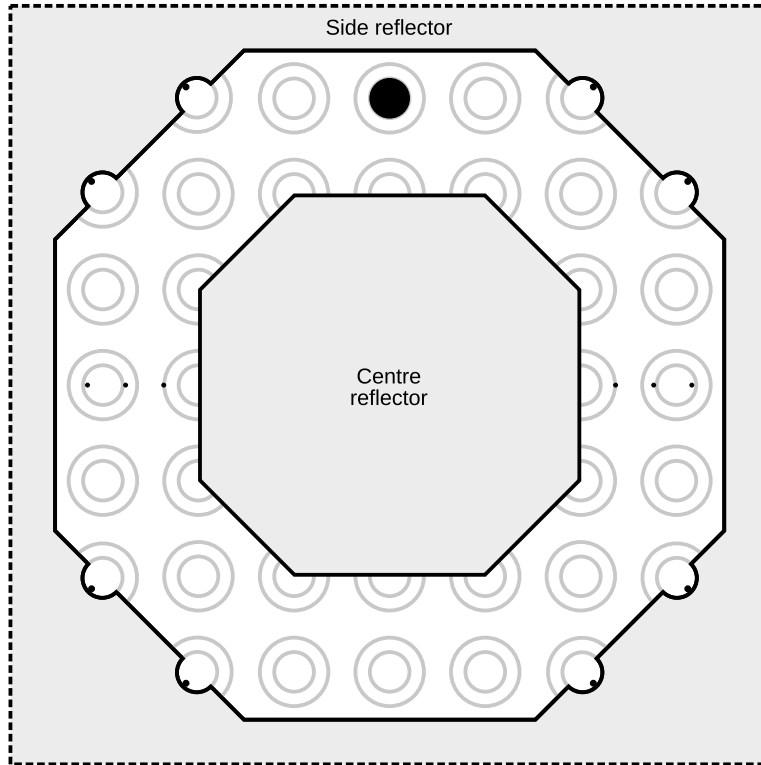


Figure 5.1: ASTRA wall geometry used in the DEM packing simulations. Pebbles were packed inside the annulus between the centre and side reflectors. The in-core control rod channel is shown as a big black circle while the small black dots mark the detector channels. The grey circles represent the 14 mm high ring-shaped projections on top of the bottom reflector blocks included in the simulations with LIGGGHTS.

In the LIGGGHTS simulations, however, in addition to including the above mentioned structures to the bottom boundary which affect the packing of the pebbles, the domain walls were subjected to a high frequency oscillating motion after the compaction of the initial packing. This was done to obtain denser pebble beds as vibration induces additional densification in the packing (An et al., 2009). Thus, for the construction of the ASTRA configurations the LIGGGHTS simulation had four phases. In the first phase, 36,000 pebbles were packed inside the cavity by dropping them from the inlets. In the second phase, the pebble bed was vibrated for a suitable amount of time. In the third phase, a number of top pebbles was removed so that the number of remaining pebbles was that of the particular experimental configuration. This way an even top surface was obtained. In the fourth phase the DEM simulation was continued to let the modified pebble bed relax to a stable state.

In total five critical configurations were calculated. The last ASTRA configuration had a top reflector made of graphite pebbles so that a thin plate was separating the fuel and the moderator pebbles. In the packing simulations an additional wall was defined on top of the highest fuel pebble of the fourth core configuration and a layer of moderator pebbles was formed on top of it in the same way as the fuel pebble configurations were formed. The number of pebbles used in each configuration is given in Table 5.1.

Values as given by Ponomarev-Stepnoi et al. (2008) were used for pebble densities and diameters. A Gaussian distribution of pebble diameters using the mean value and the standard deviation was used. The small variation in the pebble diameters was not considered to have any real effect in either the DEM packing simulation (as found out in Chapter 4) or the subsequent reactor physics calculation but it was included to emphasise that each pebble can be made unique also in the reactor physics model. The densities were used to calculate the mass of each pebble and for the fuel pebbles the density was that of the homogenised mixture of fuel particles and graphite. For other material properties, realistic values were used as suggested, for example, by Xiaowei et al. (2010) for the friction coefficient. All properties of the pebbles are given in Table 5.2.

Table 5.1: Number of fuel and moderator pebbles in the ASTRA critical configurations.

Core No.	1	2	3	4	5
Fuel/moderator pebbles	16,897	20,287	27,671	30,432	30,432/9,512

Table 5.2: Parameters used for the pebbles in the DEM packing simulations of the ASTRA critical configurations.

Parameter	symbol	Value	Unit
Fuel and moderator pebble diameter	d_p	5.985 ± 0.002	cm
Fuel pebble density	ρ_p	1,908	kg/m ³
Moderator pebble density	ρ_m	1,681	kg/m ³
Young's modulus	E	10	GPa
Poisson's ratio	ν	0.3	-
Restitution coefficient	e	0.9	-
Friction coefficient	μ_f	0.3	-

5.3 ASTRA packing simulation results

The packing simulation where 32,000 pebbles were compacted with ESyS-Particle took roughly 48 CPU hours with four parallel tasks on an Intel Core i7 processor. A time step size of $1 \cdot 10^{-5}$ s was used in the simulations. In the LIGGGHTS simulations, four parallel tasks on an Intel Xeon E5-2660 processor were utilised and the total time to compact the initial 36,000 pebbles inside the ASTRA geometry took 42 CPU hours when using a time step size of $5 \cdot 10^{-6}$ s. Some additional simulation time was then needed to vibrate and stabilise the pebble beds to obtain the individual packing configurations used in the subsequent reactor physics calculations.

The core height in the ASTRA experiments was determined by using a measuring device with a square metal plate that was lowered to the surface of the pebble bed (Ponomarev-Stepnoi et al., 2008). The height was determined as the distance from the top of the bottom reflector projections to the surface of the pebble bed. The height was taken as an average of measurements from eight positions. A similar approach was used to determine the average height of the simulated pebble beds so that the average height was determined based on eight locations. As the bottom reflector was smooth in the ESyS-Particle simulations, the height of the projections was subtracted from the heights of the simulated configurations to get comparable values. In the LIGGGHTS results the core heights were measured from the top of the projections as in the experiments.

For visualisation, a pebble bed obtained from a DEM simulation is shown in Figure 5.2. The core heights of the pebble beds obtained from the DEM simulations are given in Table 5.3 along with the core heights of the experimental configurations. As can be seen, the ESyS-Particle results differ quite significantly from the experimental configurations. The first configuration with the smallest number of pebbles is closest to the experimental one. The last simulated configuration which includes the top reflector spheres is over 1.1 pebble diameters higher than the experimental configuration. With the procedure used in the LIGGGHTS simulations, results matching within the measurement uncertainty were obtained for all core configurations.

Table 5.3: Heights of the ASTRA pebble bed configurations in the five experiments and as obtained from the DEM simulations with ESyS-Particle (Suikkanen et al., 2010) and LIGGGHTS (Rintala et al., 2014). All heights are in centimetres. For the experimental configurations also the measurement uncertainty is given. The relative differences between the experimental cores and the calculated cores are given as percentages.

Core No.	Experiment	ESyS-Particle		LIGGGHTS	
	Height	Height	Difference	Height	Difference
1	179.36 ± 0.53	180.32	0.54	179.52	0.09
2	214.14 ± 0.53	216.31	1.01	214.04	-0.05
3	291.59 ± 0.48	294.36	0.95	291.57	-0.01
4	320.05 ± 0.41	323.45	1.06	319.92	-0.04
5	421.58 ± 0.19	428.43	1.62	421.46	-0.03

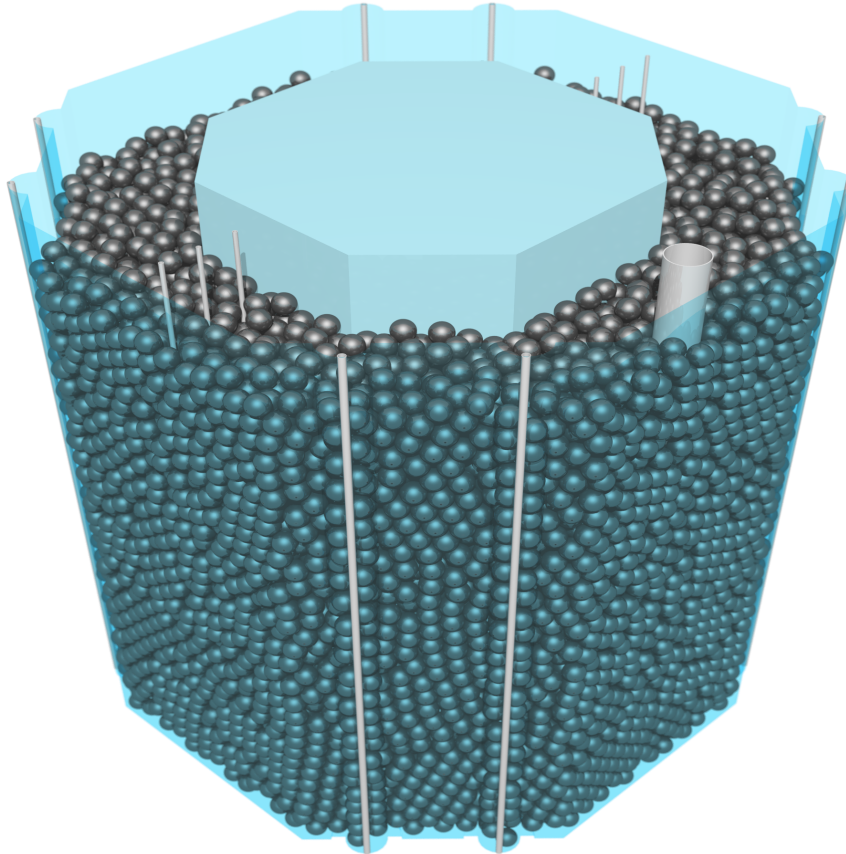


Figure 5.2: A pebble bed corresponding to ASTRA core configuration 1 with 16,897 pebbles calculated with the DEM code LIGGGHTS.

Compared to the annular pebble bed geometry investigated in Chapter 4 it is somewhat more challenging to examine the packing structure of the ASTRA pebble bed configurations. Although replicating the idea of a pebble bed reactor with a solid centre reflector, the ASTRA annulus is formed of octagonal instead of circular shapes. In addition, there are recesses in four sides of the outer reflector and the control rod and detector channels inside the pebble bed which disrupt the packing. Due to these features it is not feasible to form packing density profiles in the radial direction the same way that was done in Chapter 4. Instead, a smaller region of pebbles on the opposite side of the control rod was extracted, for which the area based packing density distribution between the inner and outer reflector walls was calculated. Also, to see how the inclusion of the graphite block projections at the bottom boundary affect the packing, packing density profiles were calculated in the axial direction. Although, in addition the Voronoi volume based packing

densities could be obtained, the complicated wall geometry of ASTRA still presents a challenge as how to cut the Voronoi cells properly at the boundaries. In Chapter 6, a method is developed that can be used to study packing structures inside more complex container geometries. The method was tested with the ASTRA geometry and the result is shown in Figure 6.10.

The packing density profiles between the inner and outer walls extracted from both, ESyS-Particle and LIGGGHTS simulation results of the ASTRA core configuration 1 are shown in Figure 5.3. There are only slight differences between the two profiles, most notably near the inner wall. Perhaps the most interesting observation that can be done from both of the profiles, however, is that the packing density oscillations caused by the bounding walls are seen throughout the whole width of the pebble bed. It was noted in Chapter 4 that the walls affect the packing approximately $5d_p$ from the wall. As the width between the walls in this case is less than $6.5d_p$ there is not enough space for the packing to stabilise before it is already affected by the opposite wall. Therefore the packing inside the ASTRA cavity is highly ordered.

Packing density profiles in the axial direction are presented in Figure 5.4. The effect of the bottom structures is clearly visible. There is a small peak at the height of the projections ($0.23d_p$) and there are clear differences in the shapes of the profiles.

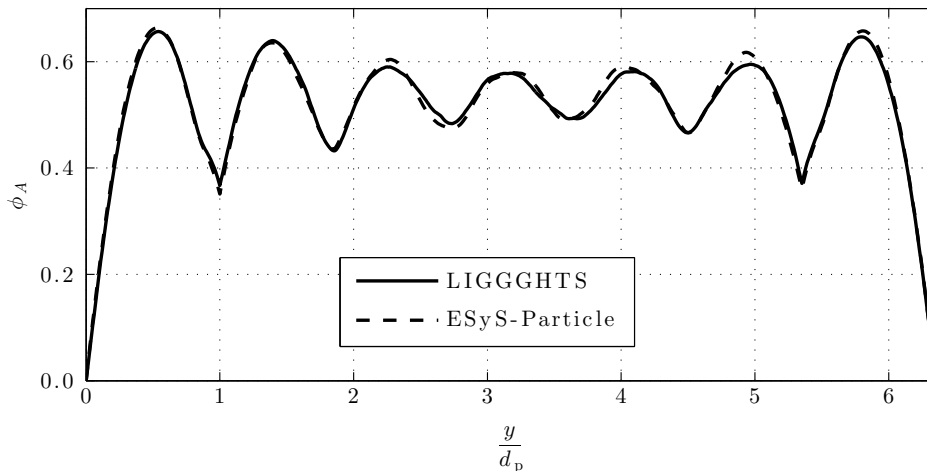


Figure 5.3: Area based packing density profiles in the y coordinate direction of the ASTRA core configuration 1. Profiles are for a column of pebbles extracted from the opposite side of the control rod channel. The plotting direction is from the outer reflector wall ($y = 0$) to the inner reflector wall. The column width and height are approximately $9d_p$ and $21d_p$, respectively and the pebbles were extracted approximately $5d_p$ away from the bottom and top boundaries.

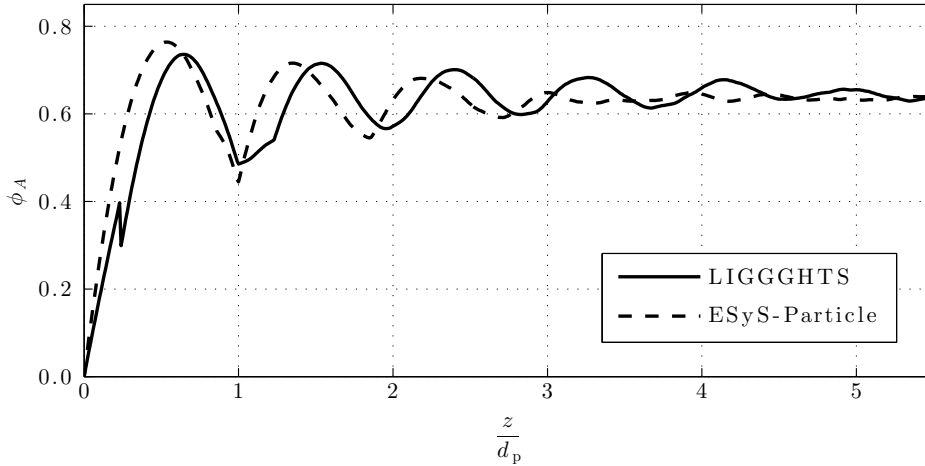


Figure 5.4: Area based packing density profiles in the axial direction for the bottom region of the ASTRA core configuration 1 showing the effect of the bottom reflector projections included in the LIGGGHTS simulations but not in the ESyS-Particle simulations.

5.4 Feedback from reactor physics calculations

The pebble bed configurations produced in the DEM simulations were provided as inputs for the criticality calculations with Serpent. Importing pebble position data to Serpent is straightforward. The data is imported in a text file containing the pebble centre coordinates, radii and "universes" in separate columns. Data is typically exported in a similar format from a DEM simulation by default.

The Serpent model of ASTRA used in the criticality calculations was as detailed as was practical to construct from the data provided by Ponomarev-Stepnoi et al. (2008). In addition to the realistic pebble beds produced in DEM simulations, the coated fuel particles inside the pebbles were sampled random positions using a random number generation algorithm. A total of 10 different fuel particle configurations was generated and these were distributed randomly among the pebbles. Despite the vast number of details the Monte Carlo calculations did not require insurmountable computational resources or computing time due to the specific features of Serpent discussed before. The Serpent calculations were performed with a computer cluster consisting of Intel Xeon E5-2660 processors and typically 64 parallel tasks were used. The total CPU time was case dependent but no more than 300 hours for any case. Calculation times with random pebble beds have been found out to be only 10 % or less longer than when using a regular lattice for the fuel particles and spheres (Rintala et al., 2014).

Serpent results calculated with JEFF-3.1.1 cross section library are given in Table 5.4 and those calculated with TENDL-2012 and JENDL-4 are given in Table 5.5. The Serpent models using pebble beds from ESyS-Particle and LIGGGHTS simula-

tions had some slight differences between each other in addition to different densities of the pebble beds, such as the bottom reflector structures that were included only in the calculations with LIGGGHTS pebble beds. Thus, the differences in the Serpent results between the ESyS-Particle and LIGGGHTS pebble beds are not solely due to the differences in the packing densities. However, there is a difference in the effective multiplication factor k_{eff} as large as 300 pcm between the ESyS-Particle and LIGGGHTS pebble beds in the core configuration 4, which is undoubtedly mostly because of the different core heights. Still it cannot be determined, what is exactly the effect of having a more dense pebble bed, as a part of the effect comes from the relative position difference between the control rods and the pebble bed.

Table 5.4: Results of the criticality calculations with Serpent using JEFF-3.1.1 cross section library and pebble beds from ESyS-Particle (Suikkanen et al., 2010) and LIGGGHTS (Rintala et al., 2014) packing simulations compared with the experimental results and sample calculations (Ponomarev-Stepnoi et al., 2008) with the MCU code using DLC/MCUDAT-2.2 cross sections.

Core	$k_{\text{eff}} \pm 1\sigma$ experiment	$k_{\text{eff}} \pm 1\sigma$ sample results MCU-REA1	$k_{\text{eff}} \pm 1\sigma$ ESyS core Serpent	$k_{\text{eff}} \pm 1\sigma$ LIGGGHTS core Serpent
1	1.0000 ± 0.0036	0.9912 ± 0.0005	1.01052 ± 0.00008	1.00805 ± 0.00008
2	1.0000 ± 0.0036	0.9936 ± 0.0005	1.01040 ± 0.00008	1.01038 ± 0.00008
3	1.0000 ± 0.0036	0.9977 ± 0.0005	1.01086 ± 0.00008	1.01216 ± 0.00008
4	1.0000 ± 0.0036	0.9989 ± 0.0005	1.01005 ± 0.00008	1.01305 ± 0.00008
5	1.0000 ± 0.0036	1.0006 ± 0.0005	1.01096 ± 0.00008	1.01403 ± 0.00008

Table 5.5: Results of the criticality calculations with Serpent using TENDL-2012 and JENDL-4 cross section libraries and pebble beds from LIGGGHTS packing simulations (Rintala et al., 2014) compared with the experimental results and sample calculations (Ponomarev-Stepnoi et al., 2008) with the MCU code using DLC/MCUDAT-2.2 cross sections.

Core No.	$k_{\text{eff}} \pm 1\sigma$ experiment	$k_{\text{eff}} \pm 1\sigma$ sample results MCU-REA1	$k_{\text{eff}} \pm 1\sigma$ TENDL-2012 Serpent	$k_{\text{eff}} \pm 1\sigma$ JENDL-4 Serpent
1	1.0000 ± 0.0036	0.9912 ± 0.0005	0.99922 ± 0.00008	0.98963 ± 0.00008
2	1.0000 ± 0.0036	0.9936 ± 0.0005	1.00256 ± 0.00008	0.99292 ± 0.00008
3	1.0000 ± 0.0036	0.9977 ± 0.0005	1.00537 ± 0.00008	0.99520 ± 0.00008
4	1.0000 ± 0.0036	0.9989 ± 0.0005	1.00633 ± 0.00008	0.99620 ± 0.00008
5	1.0000 ± 0.0036	1.0006 ± 0.0005	1.00772 ± 0.00008	0.99726 ± 0.00008

The absolute values of the multiplication factor in the Serpent calculations had a strong dependence on the used material library. Multiplication factors above unity were obtained with JEFF-3.1.1 and below unity with JENDL-4 material libraries. Calculations with TENDL-2012 library resulted in k_{eff} values in between these. By replacing the graphite library in TENDL-2012 with that used in JENDL-4, the difference in the results between TENDL-2012 and JENDL-4 practically disappeared. This strongly suggests that graphite cross sections are the main cause for the differences obtained with different material libraries (Rintala et al., 2014).

The results obtained using the pebble beds from LIGGGHTS simulations are more in line with the results of the reference Monte Carlo calculations with the MCU code (Ponomarev-Stepnoi et al., 2008) than those obtained using the more dilute pebble beds from ESyS-Particle simulations. Both, the reference calculation results and the Serpent calculation results with LIGGGHTS pebble beds have an increasing trend in the multiplication factor as the core height increases. In the reference calculations this was explained to be mostly due to using a regular lattice representation for the pebbles and fuel particles. The Serpent calculations with a more realistic geometric representation have the same increasing trend between the cases, which suggests that the regular lattice representation is at least not the main cause.

The use of DEM to obtain randomly packed pebble beds adds realism to the Monte Carlo reactor physics analyses as it removes two issues encountered with the modelling of pebble beds. First, additional artificial neutron streaming paths will not be introduced to the model when using the random configuration of pebbles instead of an ordered lattice. Second, pebbles are not clipped at the boundaries nor are any additional measures required to organise the pebbles near the boundaries to avoid clipping and ensure correct amount of materials in the domain. By using DEM it is possible to fill even complicated geometries, such as the demonstrated ASTRA case, with a correct number of pebbles. With additional measures in the DEM packing simulation, such as shaking the configuration or altering modelling parameters (see Chapter 4), it is possible to obtain a packing density corresponding to the experiments or otherwise specified values.

Some simpler algorithms are capable of producing stochastic pebble beds with packing density profiles in a good agreement with those obtained from DEM simulations and experiments (see, e.g., Auwerda et al. (2010)). Thus, equally accurate results can be expected from reactor physics calculations utilising pebble beds produced with such algorithms as with DEM. Also, the small overlaps between the pebbles in DEM results can be troublesome for some reactor physics codes and it might be necessary to use a packing method resulting in non-overlapping spheres. Although the overlaps are not problematic for Serpent, they lead to a small loss of material in Serpent calculations. However, this loss of graphite was quantified (see Suikkanen et al. (2010)) to be so small that it has a negligible effect in reactor physics calculations.

6 Mapping discrete pebble bed data to continuum volume elements

A novel method was developed to extract three dimensional porosity data of pebble beds obtained from DEM simulations directly to the calculation mesh elements of the volume averaged thermal-hydraulic models where the governing equations of fluid flow and heat transfer have been formulated for mesh elements with a porosity ε . This was done for the purpose to develop a code system coupling a Monte Carlo reactor physics code with a thermal-hydraulic solver, both using pebble packing data resulting from a DEM simulation.

For example, in the porous media model in the CFD code ANSYS Fluent (ANSYS Inc., 2013b) the continuity and momentum equations are

$$\frac{\partial}{\partial t} (\varepsilon \rho_f) + \nabla \cdot (\varepsilon \rho_f \mathbf{v}) = 0 \quad (6.1)$$

and

$$\frac{\partial}{\partial t} (\varepsilon \rho_f \mathbf{v}) + \nabla \cdot (\varepsilon \rho_f \mathbf{v} \mathbf{v}) = -\varepsilon \nabla p + \nabla \cdot (\varepsilon \boldsymbol{\tau}) + \varepsilon \mathbf{F}_B - \left(\frac{\varepsilon^2 \mu}{K} \mathbf{v} + \frac{\varepsilon^3 C}{2} \rho_f |\mathbf{v}| \mathbf{v} \right), \quad (6.2)$$

where t is the time, ρ is the density, \mathbf{v} is the velocity vector, p is the pressure, $\boldsymbol{\tau}$ is the stress tensor, \mathbf{F}_B represents the body forces, μ is the dynamic viscosity, K is the permeability and C is the inertial resistance coefficient. The subscript f is used to denote the fluid phase. The last term represents the momentum losses due to the obstacles not modelled in detail, that is pebbles. In the case of pebble bed, the permeability and inertial resistance terms can be obtained, for example, from a correlation such as suggested by Ergun (1952) or in the standard KTA 3102.3 (1981).

Additionally, energy equations are formed for the fluid and the solid representing pebbles. The energy equation of the fluid phase is

$$\frac{\partial}{\partial t} (\varepsilon \rho_f h_f) + \nabla \cdot (\varepsilon \rho_f \mathbf{v} h_f) = \nabla \cdot (\varepsilon \lambda_f \nabla T_f) + h_{fs} A_{fs} (T_s - T_f) \quad (6.3)$$

and the energy equation of the solid phase is

$$\frac{\partial}{\partial t} [(1 - \varepsilon) \rho_s h_s] = \nabla \cdot [(1 - \varepsilon) \lambda_s \nabla T_s] + h_{fs} A_{fs} (T_f - T_s) + S_h, \quad (6.4)$$

where h is the specific enthalpy, λ is the thermal conductivity, T is the temperature, h_{fs} is the interfacial heat transfer coefficient, A_{fs} is the specific interfacial area and S_h denotes additional energy source terms, such as nuclear heating. The two energy equations are linked together by the convective heat transfer coefficient h_{fs} acting on their common interfacial surface A_{fs} .

A method was developed and implemented as a MATLAB code `Spheres2Mesh.m` to directly utilise the packing data obtained from DEM simulations in the reactor

core porous media models. In addition to porosities, the code can map other useful data, such as the pebble-wise power, into the mesh elements. Furthermore, the code can be used as a tool for investigating packing structures in general. A description of the method and the implementation is given below followed by some examples of its application to pebble bed calculations.

6.1 Description of the method

The flowchart illustrating the general structure of `Spheres2Mesh.m` is given in Figure 6.1. The program requires three text files as input. The first file contains a list of the radii and the Cartesian coordinates of all spheres. The second file lists the Cartesian coordinates of the mesh corner nodes. The third file defines the mesh elements as a list of nodes for each element. The file defining the spheres can be exported from a DEM simulation. The mesh can consist of hexahedral and/or tetrahedral volume elements and it can be built using typical CFD meshing tools (see Figure 6.2 for illustration).

If hexahedral elements are given as the input, each of them will be decomposed into 12 tetrahedrons. The identifier to the base hexahedron of each tetrahedron is kept to later combine the calculated data for the base element. Tetrahedron is used as the volume entity inside which the sphere volumes are calculated as with four faces it is the simplest convex polyhedron. Three points define the face of a tetrahedron while the faces of hexahedral elements have four points. Due to, for example, numerical imprecision these four points are not necessarily on the same plane which can cause complications for the volume calculation.

The volume calculation progresses one tetrahedron at a time until all of them have been processed. A list of spheres that are possible candidates to intersect with the current tetrahedron is formed. The number of candidates is reduced by forming a bounding box for the tetrahedron and finding spheres that are inside or within a certain distance (maximum sphere radius) of the bounding box. This reduces the number of sphere-tetrahedron contact evaluations and thus speeds up the code significantly when the total number of the spheres is large. After the sphere list has been made, a second loop goes through each sphere in the list. To further simplify calculations, the current sphere is considered to be at the origin and the tetrahedron is translated accordingly.

The actual calculation of the intersection volume of a sphere and a tetrahedron makes use of the fact that the intersection volume of any two convex volumes is also convex. As both volume elements, sphere and tetrahedron, are convex, so is their intersection volume. Intersection curves between the sphere and the faces of the tetrahedron are calculated and points are generated to approximate the part of the sphere surface that is inside the tetrahedron. Together with the points of the tetrahedron that are inside the sphere, the sphere surface points form an approximation of the intersection volume which becomes more accurate the more points are used to approximate the sphere surface. A triangulation can be formed of all the points defining the intersection volume. The intersection volume can then be calculated

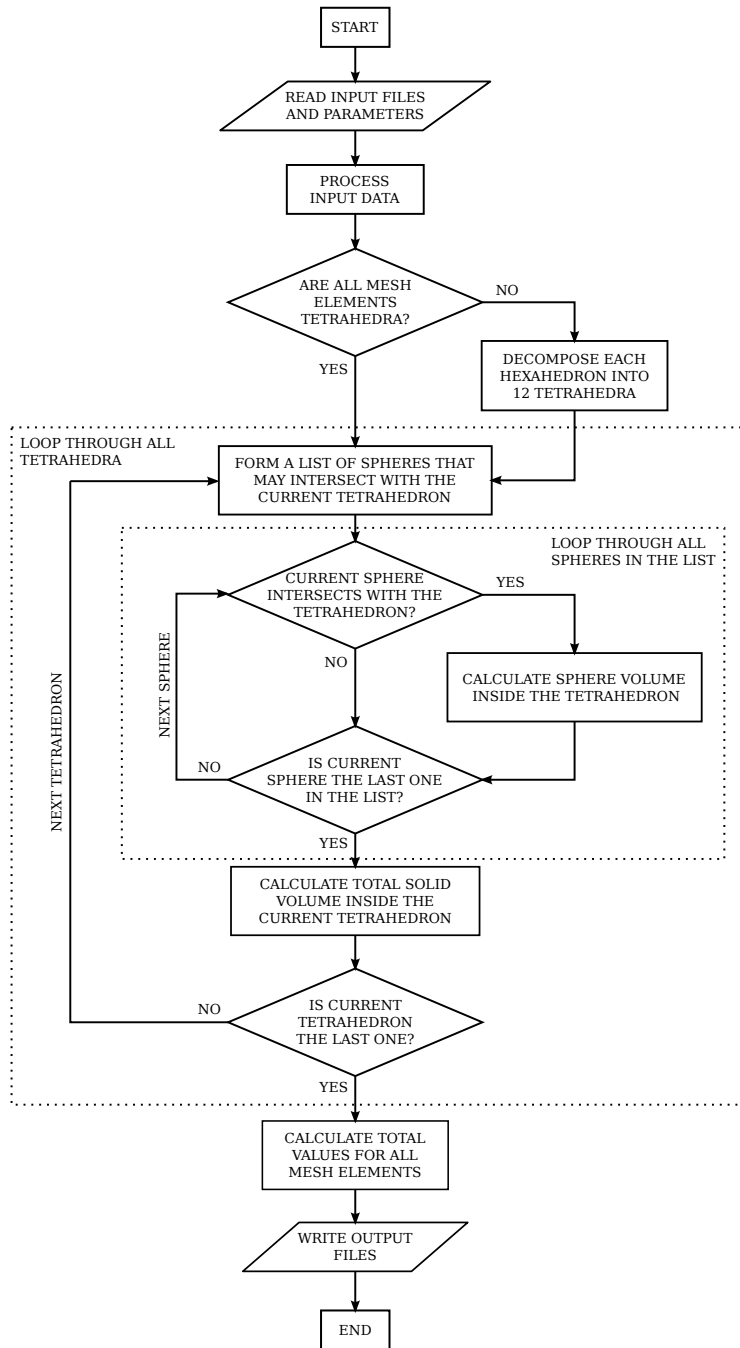


Figure 6.1: Flowchart of Spheres2Mesh.m code.

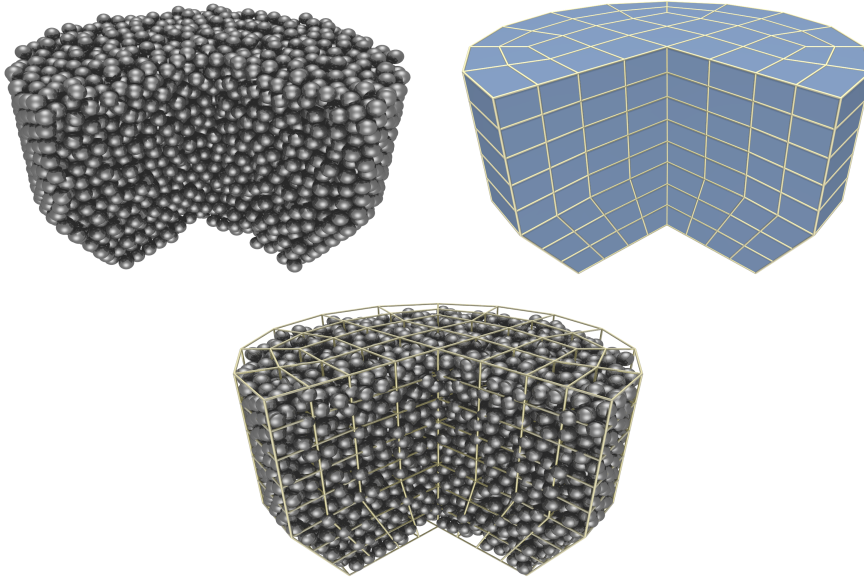


Figure 6.2: A CFD mesh constructed over a pebble bed obtained from a DEM simulation.

from this triangulation. For triangulation and calculation of the corresponding volumes a MATLAB function `convhulln` is used, which uses the Qhull code (Barber et al., 1996) for the calculation of convex hulls, Delaunay triangulations and other parameters related to computational geometry.

The calculated intersection volumes are summed up to form the total solid volume inside each tetrahedron. After all tetrahedrons have been processed, the data of the tetrahedrons that are parts of a hexahedron are combined to yield the solid volume inside these larger elements. Packing fraction of an element is then obtained by dividing the solid volume inside an element by its total volume.

Some verification calculations were performed to have confidence that the results obtained with `Spheres2Mesh.m` are correct. The individual functions forming the code were tested separately and the correctness of the volume calculation was checked by tests with regular sphere packing structures for which analytical solutions could be easily calculated. As the code is based on approximating the sphere surface with triangles formed from points generated on its surface, the volume is slightly underestimated. The estimation improves when the number of points is increased but at the same time the calculation time increases. With a reasonable number of points the volume discrepancy, however, is rather small and does not have any significant effect on the calculated porosity values. An example is shown in Figure 6.3 where the volume of a sphere is calculated with different triangulation resolutions. The percentage error in the sphere volume estimated with 10,000 points

is -0.058 and with 100,000 points -0.0058 . In practice it was found out feasible to calculate volumes even with the latter resolution.

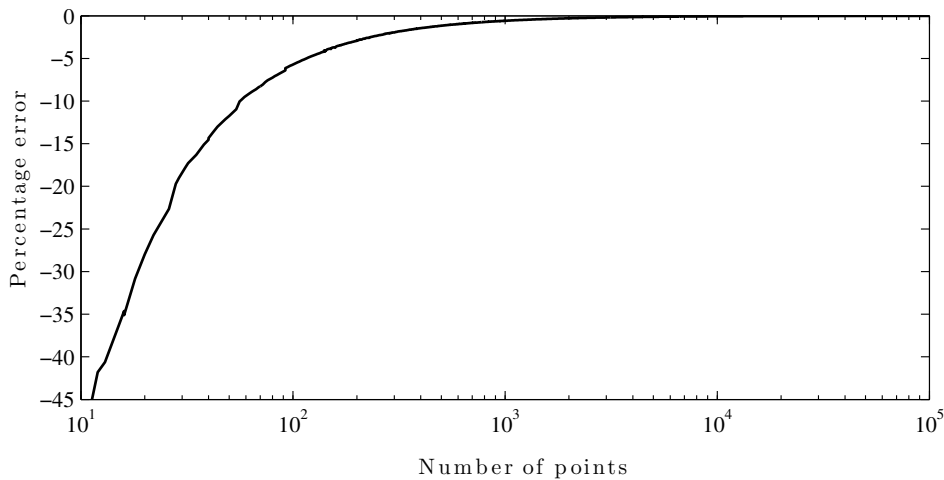


Figure 6.3: Error in the approximated sphere volume as a function of points used in the surface triangulation.

6.2 Application examples

The main motivation behind the development of `Spheres2Mesh.m` was for it to be a part of a code system used for coupled pebble bed core calculations (see Figure 6.4 for illustration). In this coupled calculation system the objective is to form realistic pebble beds with DEM that are used directly as exact pebble coordinates in the Monte Carlo reactor physics calculations (as demonstrated in Chapter 5) and mapped into the thermal-hydraulic calculation model as porosities. The reactor physics and thermal-hydraulics solvers then exchange data between each other in iterations until converged power and temperature fields in the core are obtained. In this calculation system, `Spheres2Mesh.m` is to be used not only to calculate porosities for the thermal-hydraulic model, but also to distribute the power produced in the pebbles, as calculated by the reactor physics code, into the mesh elements of the thermal-hydraulic model. The first application example gives a demonstration of calculating the porosity and power data for the mesh elements. This work has also been discussed in Suikkanen et al. (2014a).

Additionally, `Spheres2Mesh.m` can be used as a general tool for investigating the packing structures of numerically obtained sphere packings. This is demonstrated in the second example.

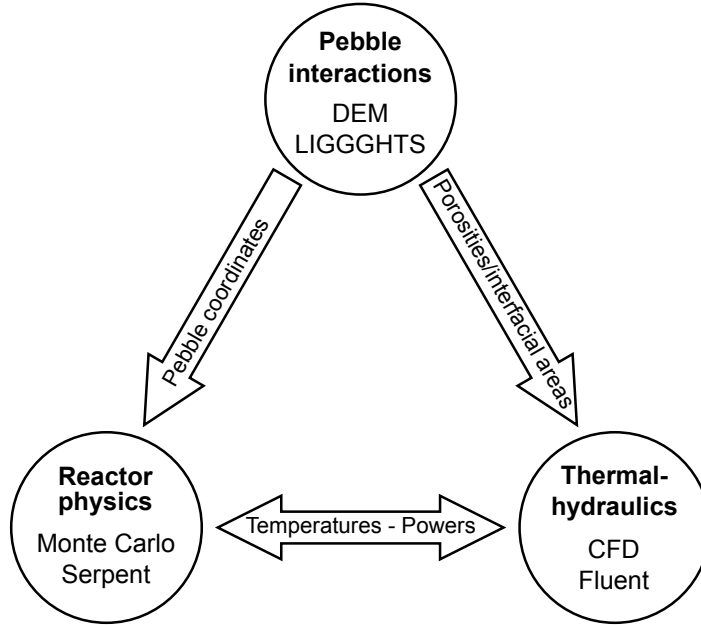


Figure 6.4: A coupled code system for pebble bed core calculations.

6.2.1 Mapping data from discrete to continuum models

As a demonstration case of the main intended use of `Spheres2Mesh.m` a calculation model representing a real size HTR-PM (Zhang et al., 2009) pebble bed reactor was constructed. A cylindrical wall geometry with a diameter of three meters transforming into a cone with a narrow outlet tube at the bottom was constructed with the CFD geometry construction and meshing software Gambit by ANSYS Inc. Next the wall geometry was exported into the DEM code LIGGGHTS in STL format. A total of 430,000 pebbles were then dropped inside the cylindrical core geometry in a DEM simulation. Due to the large number of pebbles they were dropped from the top of the geometry at specified time steps in clusters consisting of several pebbles. After all pebbles had been inserted to the simulation the column was let to settle into a stable packing. All pebbles were given a diameter of 60 mm and other parameters as defined in Table 5.2. The packing simulation was performed utilising 36 parallel tasks in a computer cluster with Intel Xeon X5650 processors. The total CPU time needed for the packing simulation was 1,785 hours when a time step size of $1 \cdot 10^{-5}$ s was used. The pebble bed resulting from the DEM packing simulation is shown in Figure 6.5.

In the second phase, a coarse CFD mesh consisting of hexahedral elements was

constructed over the pebble bed with Gambit (see Figure 6.5). Because the pebble bed is treated as a continuum in the thermal-hydraulic models based on the porous media approach, some attention to the size of the mesh elements was paid. In the continuum treatment of fluid flow in general, the calculation mesh needs to have a fine enough resolution to resolve all the desired scales of turbulence, yet much larger than the molecular length scale in order for the continuum assumption to be valid. Similarly, for porous media, typically a representative elementary volume (REV) is defined, which should be much larger than the pores (or the pebbles), yet much smaller than the macroscopic length scale defined by the calculation domain (Vafai, 2000). Also there can be restrictions for a valid porosity range in the pressure drop and heat transfer correlations that are typically used with porous media models. Further work would be needed to investigate what is the most suitable mesh element size adhering to the continuum treatment principles and validity of the used pressure drop and heat transfer correlations, but gives the maximum resolution possible.

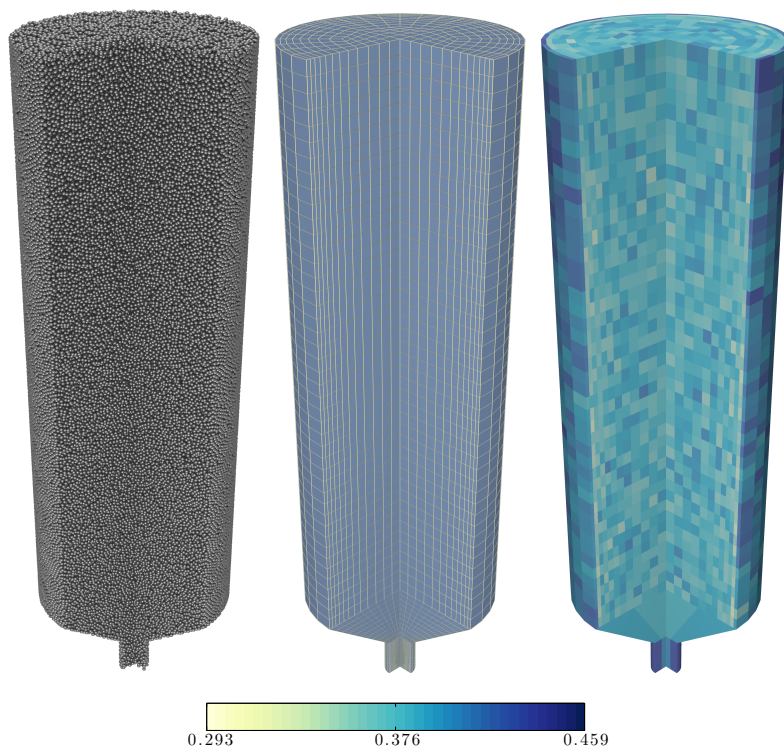


Figure 6.5: Three quarters of a pebble bed consisting of 430,000 pebbles produced in a DEM packing simulation with LIGGGHTS (left). A CFD calculation mesh constructed over the pebble bed (middle). Porosities calculated for each mesh cell with `Spheres2Mesh.m` (right). The porosities in the bottom cone and outlet pipe have been averaged into larger regions due to the small cells resulting from the structured meshing approach used to construct the mesh.

In this case the mesh elements in the main pebble bed were given a size that encloses multiple pebbles inside them. The mesh was refined towards the walls to capture some of the effect that the walls have on the packing. The elements next to the wall were given a thickness of one pebble diameter in the wall normal direction and in the two other coordinate directions the elements had side lengths of four pebble diameters. Due to the structured meshing approach that was used, the elements at the bottom cone and the outlet tube narrow down to be even smaller than the pebbles. For the reasons discussed above, instead of assigning the porosities calculated for these cells, which could be even 0 or 1, the bottom region cells were combined into four larger regions for which average porosities were calculated. The porosity value of each larger region was then assigned to the group of cells forming the region. This way, even if the individual mesh cells are smaller than the pebbles or the pores, a more reasonable porosity value is used in these cells and the 0 or 1 porosities are avoided. Another way to ensure reasonable porosities in the bottom cone geometry would be to construct an unstructured mesh in this region with larger mesh cells for which porosities are calculated.

The pebble coordinates and the mesh were read as inputs into `Spheres2Mesh.m` where porosities were calculated for the mesh elements. The calculations were performed utilising 12 parallel tasks in a single computing node of a computer cluster with an Intel Xeon E5-2660 processor. The total CPU time was 190 hours when the triangulation resolution for the spheres in `Spheres2Mesh.m` was set as 100,000 points and the number of cells in the CFD mesh for the pebble bed region was 25,600. The mesh elements coloured by their porosities are shown in Figure 6.5. Local variations can be seen in the porosity plot and especially the wall boundary cells can be seen to have higher porosities and the elements next to the wall elements somewhat lower porosities than in the bulk region.

The mapping of pebble-wise power data to the mesh elements was also tested. Power produced in each pebble was obtained from calculations with the Monte Carlo reactor physics code Serpent where the pebble coordinates from the DEM simulation were used as an input. Subsequently, also the core temperature distribution was calculated with a porous media model in ANSYS Fluent. The Serpent and Fluent models contained some additional geometry structures, such as the solid graphite reflectors and pressure vessel walls. Details of these models have been left outside the discussion in this context as the purpose here is only to demonstrate the method developed for the data transfer between the models. Further details of the Serpent and Fluent models and calculations are available in Suikkanen et al. (2014a).

The thermal power produced in the pebbles due to the nuclear fissions as calculated by Serpent is shown in Figure 6.6. As can be expected, the highest power is produced in the pebbles located in the centre of the pebble bed. The power is divided to the elements of the CFD mesh with `Spheres2Mesh.m` using the information of the fractions each pebble is divided between the mesh elements intersecting it. Mesh elements coloured by their power densities are shown in Figure 6.6. As can be seen, the general form of the power profile is retained when mapped to this coarser level. A thermal-hydraulic calculation with ANSYS Fluent was then performed using the

power density distribution as the energy source term in the energy equation (see Eq. 6.4). Coolant helium flow downwards through the porous media representing the pebble bed was calculated and the resulting core temperature distribution is shown in Figure 6.7. The temperature in each thermal-hydraulic calculation mesh cell was then mapped into the pebbles having their centres in the cell as shown in Figure 6.7.

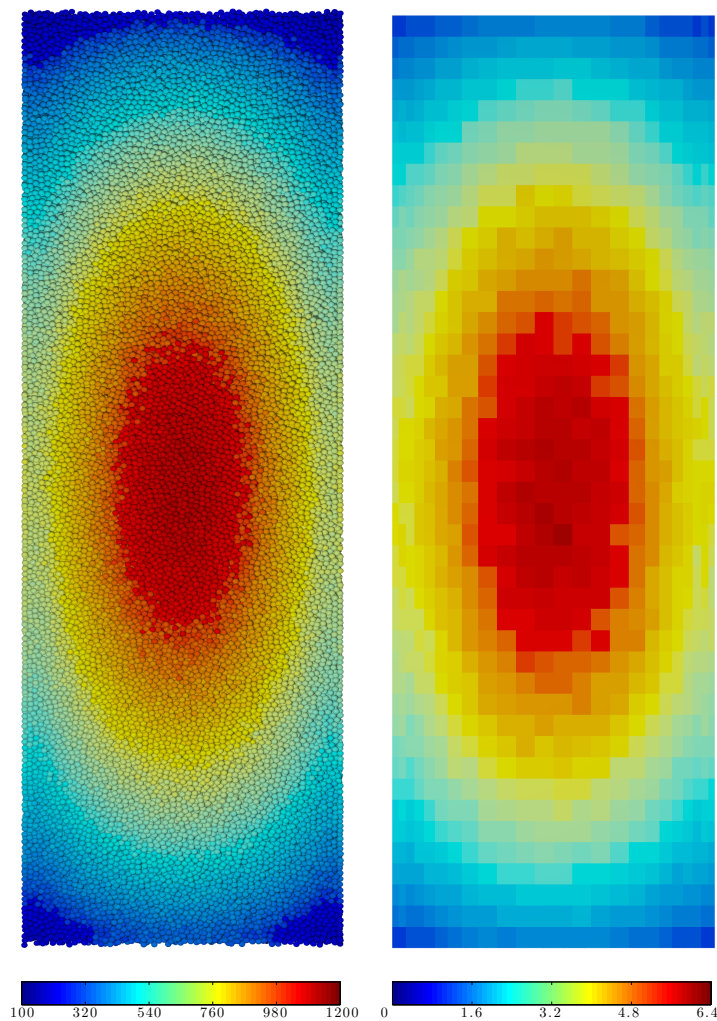


Figure 6.6: Power [W] produced in pebbles as calculated with Serpent (left) and power density [MW/m^3] mapped into the mesh cells of the thermal-hydraulic model with `Spheres2Mesh.m` (right). The plots are from the same position from the centre of the core.

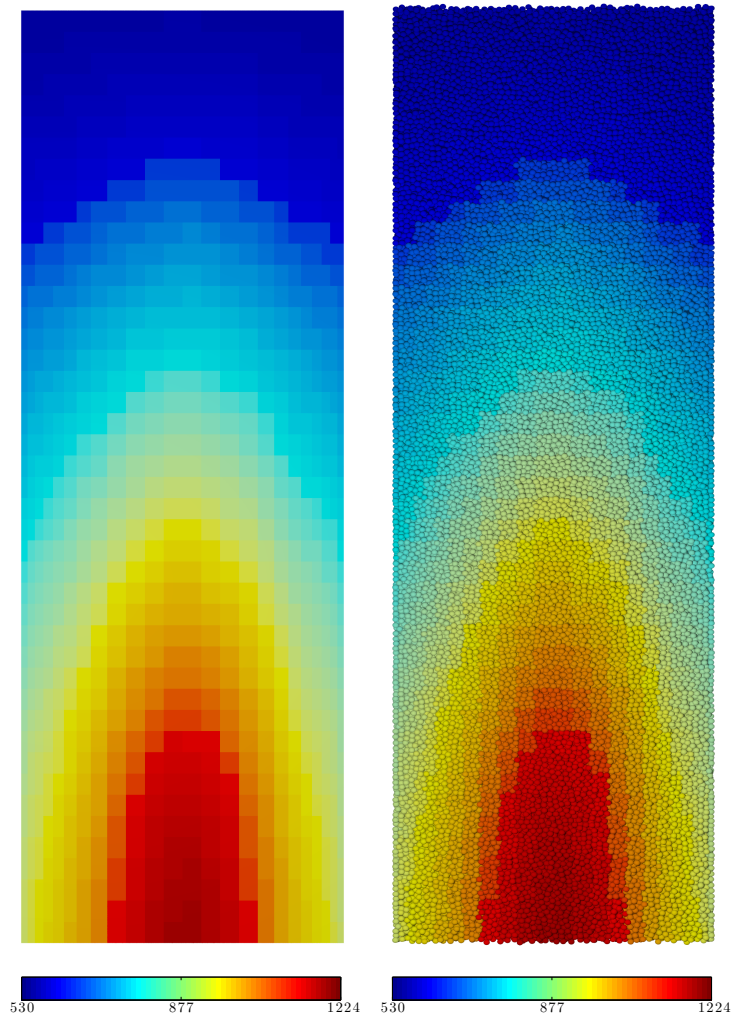


Figure 6.7: Core temperature distribution [K] obtained from the thermal-hydraulic calculation with the porous media approach in ANSYS Fluent (left) and the temperatures [K] mapped into the pebbles with `Spheres2Mesh.m` (right). The plots are from the same position from the centre of the core.

6.2.2 Extracting volumetric packing density data

An annular pebble bed compacted with DEM in Chapter 4 and a pebble bed formed inside the ASTRA geometry in Chapter 5 were selected to illustrate how the `Spheres2Mesh.m` code can be used for packing structure analyses. It can be used to form similar packing density profiles in different coordinate directions as

shown in Figures 4.1 and 4.3, but with a volume based approach more versatile than the area integral method. As the code is based on subdividing the container with an arbitrary grid that can be generated with typical meshing tools, it makes it possible to investigate packing structures in geometrically complicated containers, which would hardly be possible with the area based method and difficult with the Voronoi decomposition.

A mesh consisting of hexahedral elements was constructed over the annular pebble bed obtained from the DEM simulations. The mesh was divided with regular intervals of approximately one quarter of a pebble diameter in the radial direction. With the pebble coordinates and the mesh data as an input, `Spheres2Mesh.m` was then used to calculate the packing densities of the individual mesh cells. By combining data of consecutive cells, averages over different coordinate directions were calculated. A radial packing density profile was formed by summing up volume data of cells with the same radial coordinate. The profile is shown in Figure 6.8 along with a comparison to the corresponding profile calculated with the area based method for the same packing. As can be observed from Figure 6.8, the density profile calculated using `Spheres2Mesh.m` matches well with the one calculated using the area based method. This reproduction of the packing density profile adds confidence to the results obtained with `Spheres2Mesh.m` and acts as a verification case for the code.

Data averaged only in the axial direction is plotted in Figure 6.9, where the radial density oscillations near the walls can also be seen. A similar plot was formed for the more complicated ASTRA geometry and is shown in Figure 6.10. The ordering of the pebbles caused by the walls can be seen to be specifically pronounced in the ASTRA packing density map. This is due to the small distance between the inner and outer walls. The scale in the ASTRA plot ranges from 0 to 0.9. The zero packing density elements coincide with the detector channels which do not contain any volume. The very high packing densities are due to pebbles having a very high ordering especially in the side wall recesses and the small size of the mesh elements.

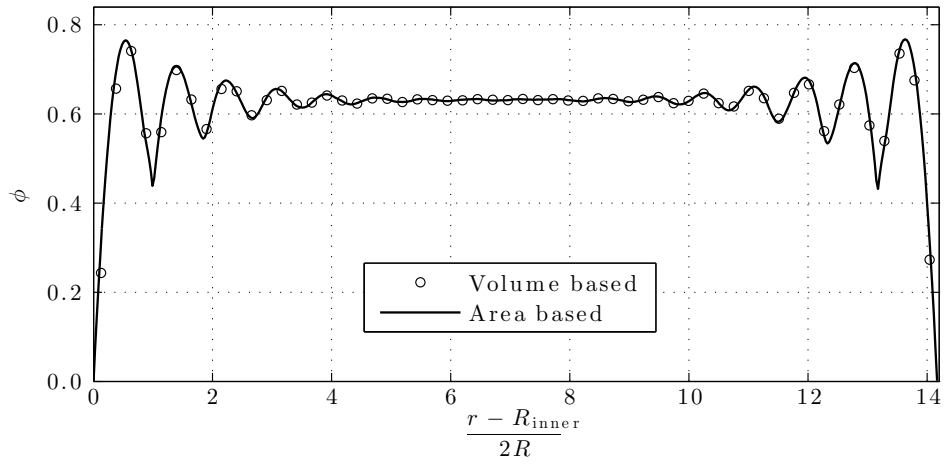


Figure 6.8: Comparison of radial packing density profiles calculated using the volume based approach and the area based approach.

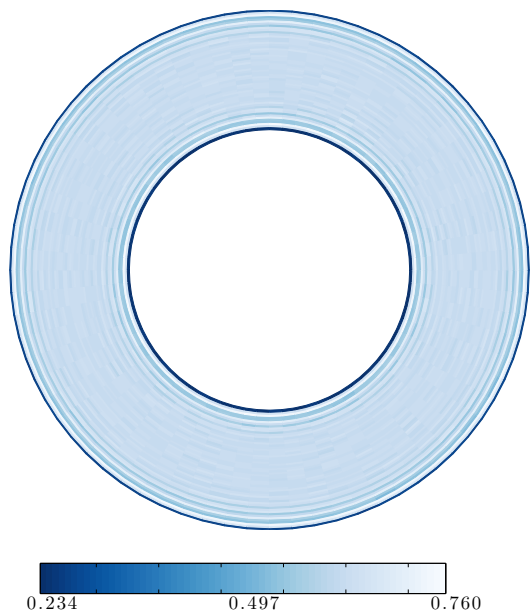


Figure 6.9: Axially averaged packing density profile of an annular pebble bed.

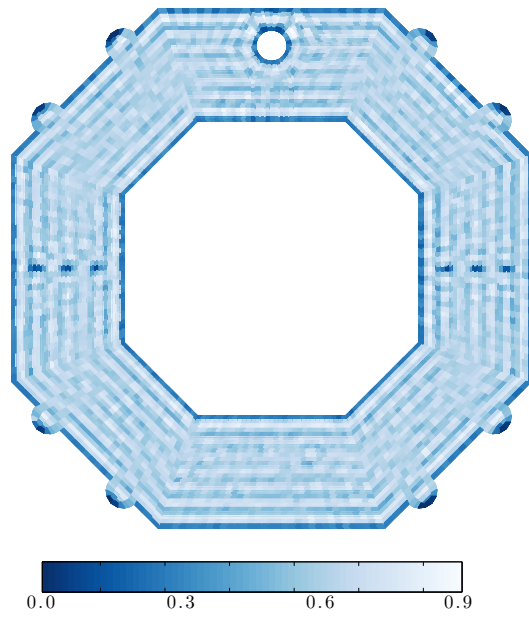


Figure 6.10: Axially averaged packing density profile of the ASTRA pebble bed.

7 Summary and conclusions of Part I

Pebble bed reactors differ from other nuclear reactor types in a significant way due to the spherical fuel elements that are piled in a stochastic configuration to form a critical core through which helium gas is led. To be able to plan the operation and predict the behaviour of such a reactor in normal and abnormal situations requires some insight on the behaviour of the pebble bed as a mechanical system. Some researchers have used experimental methods in trying to obtain this insight, while others have approached the topic with analytical or numerical methods. The approach in this work was to use a numerical discrete element simulation technique based on tracking the individual fuel pebbles in a Lagrangian reference frame and resolving their contact mechanics with force models formulated for pairwise contacts of overlapping spheres.

In Chapter 4, packing simulations were done with an in-house DEM implementation for a full size annular reactor core geometry. Various parameters were varied in simulations where the pebbles were collapsed by gravity. From the tested parameters, the restitution coefficient was found out to be the one with most effect on the average packing density of the resulting pebble bed and high packing densities were obtained with values of e close to one. Setting a very small friction coefficient also resulted in a dense packing. The other investigated parameters, that is, the density of the initial configuration and pebble size distribution, did not have a significant effect on the packing density.

Outside the investigated parameters, it would be possible to use different values, for example, for Young's modulus. However, in this work it was decided not to modify this parameter as it is more of a material property than, for example, the friction coefficient. Also, Young's modulus affects the deformations between the pebbles and thus giving it too small values would lead to unrealistically high overlaps between the pebbles in the simulations.

The information of how the tested parameters affect the density of the final packing can be useful in later work when a pebble bed with a certain density is needed. Also one way to obtain higher packing densities is to shake the packing in the simulation as was done in the work in Chapter 5. Even pebble beds with unrealistically high packing densities could be useful inputs for subsequent conservative reactor physics or thermal-hydraulics analyses.

The more detailed packing structure analyses confirmed the influence of walls which is especially pronounced in the annular pebble bed geometry with pebbles packed between a relatively narrow thickness. The different packing characteristics at the near wall regions should be taken into account especially in thermal-hydraulic core analyses where the flow and heat transfer undoubtedly differ from those at the bulk region. While the bulk of the pebble bed seems to be rather homogeneous, the near wall regions have interesting structures. While the near wall region in general is more dilute than the bulk of the bed, locally highly ordered regions can manifest. These regions became more apparent as the average density of the pebble bed increased.

The in-house DEM code used in the simulations performed well and the obtained packed pebble beds were found out to be realistic when comparisons with available experimental data were made. There are benefits in own code development, such as the possibility to customise and optimise the code to specific needs. However, the effort required might be too much especially for a small user and developer group.

Although DEM has been used for pebble bed related analyses by several other investigators as reviewed in Chapter 2, it would seem that most interest has concentrated on analysing the flow of the pebbles through the core. Also the local packing structure details have not received too much attention, especially from the viewpoint of reactor physics, fluid dynamics and heat transfer.

In Chapter 5, packing simulations were performed with two freely available open source DEM codes ESyS-Particle and LIGGGHTS to supplement Monte Carlo reactor physics calculations with the Serpent code. As the packing simulations for the ASTRA criticality analyses required inclusion of rather complex wall boundaries, the implementation of more versatile wall boundary definitions to the in-house DEM code used in the previous work (Chapter 4) would have required major modifications to its source code. Thus, alternatives were searched for. From the two open source DEM codes that were tested, especially LIGGGHTS proved out to be a well suited tool for pebble bed related simulations. A highly detailed model of the ASTRA core could be defined, which included even details such as detector channels and graphite block alignment projections. As all these details were present also in the subsequent reactor physics model, the pebble distributions obtained from the DEM packing simulation could be directly used in Serpent.

After successful utilisation of the produced pebble beds in the Serpent code, it can be concluded that DEM can be used to provide realistic packed pebble beds to enhance the realism and accuracy of the reactor physics analyses. Two typical modelling artefacts are automatically avoided when the pebble beds are produced in DEM simulations instead of specifying them in ordered lattice configurations. First, the pebbles are not clipped at the boundaries. Second, no artificial streaming paths for neutrons are introduced. Although other investigators have reported introducing stochasticity in Monte Carlo reactor physics analyses of pebble bed geometries with various means, no previous work would seem to be documented in public literature where specifically DEM would have been used for this purpose. As DEM models the dynamics of sphere systems using physically more correct models than simpler packing algorithms it can be used to produce realistic pebble configurations inside virtually any container geometry and also for more advanced investigations. The pebble bed can, for example, be shaken to introduce additional densification if the effects of packing density on the core physics needs to be studied.

In Chapter 6, a method was developed and implemented as `Spheres2Mesh.m` code to calculate porosities (or packing densities) in hexa/tetrahedral mesh elements of arbitrary size. The code is mainly intended for mapping packing structure data from DEM simulation results to the calculation cells of volume averaged thermal-hydraulic models with as high resolution as possible and also to transfer pebble-wise data, such as power obtained from Monte Carlo reactor physics calculations, to the

mesh cells accurately. In a fully coupled reactor physics and thermal-hydraulics calculation also the temperatures calculated for the cells can be mapped to the correct pebbles in the reactor physics model based on the calculated data of pebble locations relative to the mesh cells.

Additionally `Spheres2Mesh.m` can be used to analyse sphere packing structures in general in any container geometry that can be meshed with the above mentioned mesh elements. It adds a new volumetric scale in between the average over the whole packing and single pebble scale obtained from Voronoi decomposition at which packing density variations can be analysed. When using mesh elements smaller than the spheres, it can also be used to obtain packing density profiles in different coordinate directions similar to ones obtained using the area based analysis method described in Chapter 3.

Although calculating sphere volumes (and surface areas) inside the cells of a CFD calculation mesh constructed over a computer generated packed bed would seem an intuitive way of obtaining porosities and other derived data directly into the mesh cells, no previous published work where exactly this would have been done could be found. The only somewhat similar work found was done by Nandakumar et al. (1999), who developed a similar tool to obtain porosities of triangulated packing objects in sample volumes. However, Nandakumar et al. (1999) only used the tool for post-processing purposes to obtain porosity profiles of packed beds.

In further development of `Spheres2Mesh.m`, in addition to hexahedra and tetrahedra, support for other mesh element types that can be divided into tetrahedra could rather easily be included. Also to improve accuracy in heat transfer analyses the code could be modified to include the calculation of exact interfacial surface areas in each mesh element which is needed, for example, in the calculation of convective heat transfer when the so called thermal non-equilibrium model is used in the porous media (see Equations 6.3 and 6.4). One important development effort would also be to optimise the code to improve calculation speed and thus make it more practical to use. To make the code a more general tool also for application outside pebble bed reactors, it could be extended to handle other packing shapes in addition to spheres.

As a whole, the work presented in the first part of the thesis paves the way for multi-physics analyses of pebble bed reactors where DEM is used to provide realistic pebble packing data with specified packing densities for three dimensional Monte Carlo reactor physics and porous media thermal-hydraulics models, which also exchange data between each other, and together provide an accurate numerical estimation of the state of the reactor.

Part II

CFD modelling for gas cooled fast reactors

8 Background and state of art

Designing a gas cooled fast reactor (GFR) meeting the Generation IV principles (NERAC, 2009) of economic competitiveness while ensuring sufficient cooling of the fuel during abnormal events, such as depressurisation of the primary circuit, remains a specific challenge of the reactor type. It is essential to pressurise the helium coolant to 7–10 MPa to improve the core heat transfer during operation (Waltar et al., 2012). Also in the case of a break in the primary circuit it is necessary to have a back up pressure provided by the so called guard containment and/or by injecting heavier gas than helium into the system to ensure sufficient decay heat removal (Epiney et al., 2010). Whether it is possible to achieve efficient enough cooling using decay heat removal loops operating only by natural circulation depends on the design.

In addition to high coolant gas pressure, another efficient way to enhance heat transfer is to increase the convective heat transfer by inducing turbulence with artificial surface roughness manufactured on the heat transfer surfaces. This at the same time will increase the pressure drop through the reactor core, hindering especially natural circulation and increasing pumping costs. Therefore, an optimisation between the heat transfer efficiency and the pressure losses is needed if additional turbulence inducers are to be used.

This issue is addressed in this part of the thesis. The enhancement of heat transfer with artificial surface roughness elements in a rod geometry is numerically investigated. The numerical work has been done in parallel with the related experiments performed with the L-STAR (Luft, Stab, Abstandshalter, Rauheiten) facility at the Karlsruhe Institute of Technology (KIT). The numerical study is by nature a benchmark calculation performed within the European project THINS (Thermal-Hydraulics of Innovative Nuclear Systems) with the objective of qualification of the numerical models and their application practices for the specific topic (Roelofs et al., 2012). Thus, the numerical results are compared with the experimental ones to draw conclusions of the performance and adequacy of the numerical models and tools that can be used in the design and development of the European demonstration reactor ALLEGRO. This work along with some of the results is also discussed in Gómez et al. (2014b).

8.1 A brief review of related work

Ground work in studying the effects of surface roughness to turbulent fluid flow was conducted by Nikuradse (1933). He did experiments for turbulent flow in pipes having uniform sand grains glued to provide roughness. He then measured the pressure drops for different roughness heights. Later, Dipprey and Sabersky (1963) performed experiments using similar type of roughness investigating also heat transfer. For correlating their results they made use of the similarity between momentum and heat transfer.

More related to the topic of rib-type roughness, Webb et al. (1971) did experiments on rib roughened tubes with various rib height to pipe diameter and rib pitch

to height ratios. Based on the experimental results and the ideas by Nikuradse (1933); Dipprey and Sabersky (1963) they proposed correlations for the friction factor and the heat transfer coefficient. Similar experimental work has been carried out since then for different rib shapes and other parameters by several investigators (see e.g. Han et al. (1978)). Most relevantly, work related specifically to GFR fuel rods and the annular geometry studied in this work, was done as a joint effort by the EIR (Eidgenössisches Institut für Reaktorforschung) and KfK (Kernforschungszentrum Karlsruhe) during 1970's (Dalle Donne et al., 1978; Dalle Donne and Meyer, 1977). Experiments to obtain friction and heat transfer coefficients were done for a single rod that was roughened with ribs and cooled using either helium, nitrogen or air. At the time also rod bundles consisting of several roughened rods were investigated (Dalle Donne et al., 1977; Hudina and Markôczy, 1977). More recent rod bundle experiments and supporting numerical investigations have been done utilising the ESTHAIR facility at CEA (Commissariat à l'énergie et aux énergies alternatives) where a rod bundle representative of one planned for the ALLEGRO demonstrator reactor was investigated (Berthoux and Cadiou, 2010). Also more recent experimental work on rib roughness including measurement with optical techniques has been done, for example, by Rau et al. (1998).

Numerical investigations on rib roughness has been done, for example, by Cui et al. (2003) who investigated turbulent flow in a channel with a few ribs by LES (large eddy simulation). Miyake et al. (2001) and Nagano et al. (2004) performed similar investigations with DNS (direct numerical simulation) studying also heat transfer. Ryu et al. (2007a,b) did RANS (Reynolds averaged Navier-Stokes) simulations for a two dimensional geometry. Many investigators have disregarded thermal conduction in the ribs and in the solid materials below and imposed a simplified thermal boundary condition of constant heat flux on these surfaces. Iaccarino et al. (2002) studied the effect that solving conduction in the ribs has on the heat transfer results and found out that the local Nusselt numbers are strongly affected by the thermal boundary condition, that is, solving conjugate heat transfer improves the heat transfer results. Specifically for gas cooled reactor fuel rods with ribs, Takase (1996) performed axisymmetric RANS simulations using periodic boundary conditions and Keshmiri (2011) did simulations for AGR fuel elements with rib roughness using a non-linear eddy viscosity model.

It can be noted from the above listed numerical investigations that all of them have been done with a relatively simple geometrical model, that is, either a three dimensional model in a region of a single or few ribs has been investigated or an axisymmetric model has been defined. In the present work the investigated geometry is the full three dimensional geometry of a fuel rod inside a hexagonal cross section channel and the effects of different heat transfer mechanisms, that is conduction, convection and radiation are all considered.

8.2 Description of the related experiments

The purpose of the L-STAR experimental campaign at KIT is to investigate heat transfer and its enhancement by artificial surface structure elements in a gas cooled annular channel (Gomez et al., 2013). The experiments are to provide high quality measurement data for the qualification of numerical simulation tools, especially CFD codes, and to collect experimentally derived friction factors and heat transfer coefficients in a database for the development of physical models. CFD grade validation data is extracted, for example, by using optical measurement techniques, such as laser Doppler anemometry (LDA), which can provide flow field data at the scale of the surface structure elements. The results of the experiments and validated computer codes can then be used to tackle thermal-hydraulic issues of GFR designs, such as the ALLEGRO (Poette et al., 2009) GFR technology demonstrator.

The L-STAR experimental facility (see Figure 8.1) is a gas loop using air as the operating gas. It has been designed for a maximum temperature and pressure of 473 K and 0.3 MPa, respectively, and for Reynolds numbers below $2.5 \cdot 10^5$. The essential part of the facility is the vertically oriented hexagonal flow channel (Figure 8.1 bottom), inside which an electrically heated rod instrumented with thermocouples is fixed in the centre position. The width between the sides of the hexagon is 67.54 mm. The flow channel has been designed to replicate a sub-channel of a single fuel rod of a GFR.

The flow enters the test section at the bottom and leaves from the top. The horizontal inlet and outlet pipes have an angle of 65.5° between each other and the vertical distance between their centre axes is 3,246 mm. The heated rod replicating a fuel rod has an outer diameter of 34.55 mm and contains six individual heater elements inside. The total length of the rod is 3,780 mm of which approximately 2,500 mm is heated. Additional details with measures are shown in Figure 8.1.

Air is circulated through the loop by a blower and there are two heat exchangers to cool down the gas. The gas mass flow rate is measured with a Coriolis mass flow meter and there is a power control unit used to adjust the power in the electric heater elements. Data is recorded from various temperature and pressure measurement locations with a separate data acquisition system.

The L-STAR experiments considered within the context of this work consist of investigations with two different rod geometries; one with a smooth surface and one with a surface covered with equally distributed rings with a square cross section. In some of the experimental cases heating is not applied and only the inlet mass flow rate is varied. The nominal conditions for the experimental cases are given in Table 8.1. In all cases the inlet gas temperature is 293 K and the absolute pressure is 0.15 MPa. All of the experimental cases are run into steady state conditions before any data is measured.

Table 8.1: The L-STAR experimental cases (Arbeiter et al., 2013b). The experiments are performed for a smooth and a roughened rod.

Case ID	Mass flow rate [g/s]	Heating power [W]
Cold rod		
Case 1	6.32	-
Case 2	12.6	-
Case 3	25.3	-
Case 4	37.9	-
Case 5	50.5	-
Heated rod		
Case 1	25.3	1016
Case 2	25.3	677
Case 3	25.3	1354
Case 4	12.6	508
Case 5	37.9	1523

9 Flow and heat transfer models

This chapter presents the governing equations of fluid flow and heat transfer and the models that are used to solve turbulent flow and heat transfer in the context of this work. The equations are presented using the Einstein summation convention with indices i , j and k .

9.1 Governing equations

In the following, the governing equations of fluid flow and heat transfer are given. A low Mach number flow ($Ma < 0.3$) is considered in the context of this work, yet the temperature dependency of the density is accounted for.

The conservation of mass or the continuity equation is

$$\frac{\partial \rho}{\partial t} + \frac{\partial}{\partial x_i} (\rho v_i) = 0 \quad (9.1)$$

where ρ is the density, t is the time and v is the velocity (Wilcox, 2006). The transport equation of momentum or the Navier-Stokes equation is

$$\frac{\partial}{\partial t} (\rho v_i) + \frac{\partial}{\partial x_j} (\rho v_i v_j) = -\frac{\partial p}{\partial x_i} + \frac{\partial t_{ij}}{\partial x_j} + F_i, \quad (9.2)$$

where p is the pressure, t_{ij} is the viscous stress tensor and F represents additional body forces (e.g. gravity) (Wilcox, 2006). For incompressible flow the viscous stresses are given by

$$t_{ij} = 2\mu s_{ij}, \quad (9.3)$$

where μ is the dynamic viscosity and s_{ij} is the strain-rate defined as

$$s_{ij} = \frac{1}{2} \left(\frac{\partial v_i}{\partial x_j} + \frac{\partial v_j}{\partial x_i} \right). \quad (9.4)$$

The conservation equation of thermal energy formulated for incompressible ideal gas and omitting energy source due to viscous dissipation is given by

$$\frac{\partial}{\partial t} (\rho c_p T) + \frac{\partial}{\partial x_i} (v_i \rho c_p T) = \frac{\partial}{\partial x_i} \left(\lambda \frac{\partial T}{\partial x_i} \right) + S_h, \quad (9.5)$$

where c_p is the specific heat capacity, T is the temperature, λ is the thermal conductivity and S_h represents additional thermal energy sources. In solid materials Equation 9.5 simplifies to a conduction equation and the convection term on the left hand side disappears.

9.2 Turbulence modelling

Turbulent flow and its modelling is discussed in various textbooks. Based on White (2006) and Wilcox (2006) a brief summary of the subject is given.

Turbulence consists of a continuous range of scales and the ratio between the smallest and largest turbulent eddies increases with an increasing Reynolds number. Turbulent eddies exchange energy in a cascade process in which the larger eddies transmit energy to the smaller ones and eventually kinetic energy is dissipated into heat due to viscosity. The smallest scales of turbulence are characterised by the so called Kolmogorov scales of length, time and velocity. A solution process where turbulent flow is resolved in the resolution of these smallest scales by the direct solution of Equations 9.1 and 9.2 is called direct numerical simulation (DNS). It is, however, computationally very demanding as it requires spatial and temporal discretisation in the order of the Kolmogorov scales. Thus, it is currently not very useful for practical applications.

A computationally less demanding, yet still highly accurate method to solve turbulent flow is referred to as large eddy simulation (LES). In LES the turbulent scales are resolved to a certain extent and the smaller scales are modelled. Compared to DNS it is much cheaper in computational terms as the mesh density requirements are not as high. However, LES is still far too expensive method for many practical applications.

The next step towards modelling turbulence at a more practical level are the Reynolds averaged Navier-Stokes (RANS) models. A multitude of RANS models exist, which have a varying level of complexity and application areas in which they can be used. They are, however, based on the Reynolds averaged form of the continuity and the momentum equations which are obtained by disassembling the variables, for example, velocity into a mean component \bar{v} and a fluctuation component v' and performing time averaging for the equations.

The Reynolds averaged continuity and momentum equations are

$$\frac{\partial \rho}{\partial t} + \frac{\partial}{\partial x_i} (\rho \bar{v}_i) = 0 \quad (9.6)$$

and

$$\frac{\partial}{\partial t} (\rho \bar{v}_i) + \frac{\partial}{\partial x_j} (\rho \bar{v}_i \bar{v}_j) = -\frac{\partial \bar{p}}{\partial x_i} + \frac{\partial}{\partial x_j} (2\mu \bar{s}_{ij} - \overline{\rho v'_i v'_j}), \quad (9.7)$$

where the additional term $-\overline{\rho v'_i v'_j}$ consisting of the fluctuating components of the velocity is known as the Reynolds stress tensor for which a model is needed in order to close the equation system.

RANS models can basically be divided into eddy viscosity models and Reynolds stress models (RSM). In RSM, transport equations are formed for each of the Reynolds stress components $\overline{v'_i v'_j}$, which means six equations in addition to the continuity, momentum, turbulence kinetic energy and, for example, dissipation rate equations. Thus, RSM is computationally a rather complicated and expensive method, although it is capable of accounting for some flow features, such as anisotropic turbulence, that the eddy viscosity models are inherently incapable of.

The eddy viscosity models are based on the Boussinesq eddy viscosity approximation in which the turbulent stresses are modelled with a gradient term in analogy with molecular diffusion as

$$-\rho \overline{u'_i u'_j} = \mu_t \left(\frac{\partial \bar{v}_i}{\partial x_j} + \frac{\partial \bar{v}_j}{\partial x_i} \right) - \frac{2}{3} \rho k \delta_{ij}, \quad (9.8)$$

where μ_t is the eddy or turbulent viscosity, k is the turbulence kinetic energy and δ_{ij} is the Kronecker delta tensor. Models are then formed for the eddy viscosity. There are several eddy viscosity models ranging from algebraic (zero equation) models to two equation models. It is these models, especially the two equation models, that currently provide a sufficient level of accuracy with a tolerable computational requirements for most practical calculations.

There are also models that situate in between the common two equation and Reynolds stress models, such as algebraic stress models (ASM) and non-linear eddy viscosity models. These are, however, not as commonly used and may not be readily available in typical CFD codes.

In this work, a two equation eddy viscosity model and an RSM model are used. These models are presented in more detail in the following.

9.2.1 Realisable $k - \epsilon$ model equations

The realisable $k - \epsilon$ model (Shih et al., 1995) is used in this work. In this model, equations for the transport of turbulence kinetic energy k and dissipation rate ϵ are solved. They are presented below in the form they are given in the theory manual of the CFD solver used in this work (ANSYS Inc., 2013a) but by omitting terms irrelevant in this context.

The transport equation of turbulence kinetic energy is

$$\frac{\partial}{\partial t} (\rho k) + \frac{\partial}{\partial x_j} (\rho k \bar{v}_j) = \frac{\partial}{\partial x_j} \left[\left(\mu + \frac{\mu_t}{Pr_k} \right) \frac{\partial k}{\partial x_j} \right] + G_k + G_b - \rho \epsilon, \quad (9.9)$$

where Pr_k is the turbulent Prandtl number for k (default value $Pr_k = 1.0$), and G_k and G_b are terms for the generation of turbulence kinetic energy due to the mean velocity gradients and buoyancy, respectively. The turbulent viscosity is given by

$$\mu_t = \rho \frac{C_\mu k^2}{\epsilon}, \quad (9.10)$$

where C_μ is calculated as a function of mean strain and rotation and k and ϵ instead of being a constant value as in the standard $k - \epsilon$ model. Further details are available in Shih et al. (1995). In Equation 9.9 the term G_k is calculated as

$$G_k = 2\mu_t \bar{s}_{ij} \bar{s}_{ij} \quad (9.11)$$

and G_b in the case of ideal gases is given by

$$G_b = -g_i \frac{\mu_t}{\rho Pr_t} \frac{\partial \rho}{\partial x_i}, \quad (9.12)$$

where g is the gravitational acceleration and Pr_t is the turbulent Prandtl number for energy.

The transport equation of turbulence dissipation rate in the realisable $k - \epsilon$ model is

$$\begin{aligned} \frac{\partial}{\partial t} (\rho\epsilon) + \frac{\partial}{\partial x_j} (\rho\epsilon\bar{v}_j) &= \frac{\partial}{\partial x_j} \left[\left(\mu + \frac{\mu_t}{Pr_\epsilon} \right) \frac{\partial \epsilon}{\partial x_j} \right] + \rho C_1 \sqrt{2\bar{s}_{ij}\bar{s}_{ij}}\epsilon \\ &\quad - \rho C_2 \frac{\epsilon^2}{k + \sqrt{\frac{\mu\epsilon}{\rho}}}, \end{aligned} \quad (9.13)$$

where Pr_ϵ is the turbulent Prandtl number for ϵ (default value $Pr_\epsilon = 1.2$), the coefficient C_1 is

$$C_1 = \max \left[0.43, \frac{\sqrt{2\bar{s}_{ij}\bar{s}_{ij}} \frac{k}{\epsilon}}{\sqrt{2\bar{s}_{ij}\bar{s}_{ij}} + 5} \right] \quad (9.14)$$

and the coefficient C_2 is constant (default value $C_2 = 1.9$).

9.2.2 Reynolds stress model equations

In Reynolds stress turbulence modelling, transport equations for the individual Reynolds stress terms $\overline{\rho v'_i v'_j}$ are formed as

$$\begin{aligned} \frac{\partial}{\partial t} (\overline{\rho v'_i v'_j}) + \frac{\partial}{\partial x_k} (\overline{\rho \bar{v}_k v'_i v'_j}) &= \frac{\partial}{\partial x_k} \left[\mu \frac{\partial}{\partial x_k} (\overline{v'_i v'_j}) \right] + D_{ij} + E_{ij} + \Pi_{ij} \\ &\quad - \rho \left(\overline{v'_i v'_k} \frac{\partial \bar{v}_j}{\partial x_k} + \overline{v'_j v'_k} \frac{\partial \bar{v}_i}{\partial x_k} \right) + B_{ij}. \end{aligned} \quad (9.15)$$

In the above equation, the second term on the left represents stress transport by convection, the first term on the right represents stress transport by diffusion and the fifth term on the right is the term for stress production. These terms can be solved directly. However, the remaining tensor terms D_{ij} , E_{ij} , Π_{ij} and B_{ij} represent turbulent transport, dissipation, pressure-strain and buoyancy production, respectively, which need to be modelled to close the equation system. The turbulent diffusion term is

$$D_{ij} = -\frac{\partial}{\partial x_k} (\overline{\rho v'_i v'_j v'_k} + \overline{p' v'_i} \delta_{jk} + \overline{p' v'_j} \delta_{ki}). \quad (9.16)$$

The dissipation term is

$$E_{ij} = -2\mu \overline{\frac{\partial v'_i}{\partial x_k} \frac{\partial v'_j}{\partial x_k}} \quad (9.17)$$

and the pressure-strain term is

$$\Pi_{ij} = \overline{p' \left(\frac{\partial v'_i}{\partial x_j} + \frac{\partial v'_j}{\partial x_i} \right)}. \quad (9.18)$$

When heat transfer is significant, the stress production due to buoyancy is included in the equation, which for ideal gases can be written as (ANSYS Inc., 2013a)

$$B_{ij} = -\frac{\mu_t}{\rho Pr_t} \left(g_i \frac{\partial \rho}{\partial x_j} + g_j \frac{\partial \rho}{\partial x_i} \right). \quad (9.19)$$

9.2.3 Near wall treatment

The turbulent boundary layer is described using dimensionless wall units. A dimensionless wall normal distance y^+ is defined as

$$y^+ = \frac{y v_\tau \rho}{\mu}, \quad (9.20)$$

where y is the normal distance from the wall and v_τ is the friction velocity calculated with the wall shear stress τ_w as

$$v_\tau = \sqrt{\frac{\tau_w}{\rho}}. \quad (9.21)$$

Also a dimensionless velocity can be defined as

$$v^+ = \frac{v}{v_\tau}. \quad (9.22)$$

The turbulent boundary layer can be divided into separate regions (see e.g. Wilcox (2006) and White (2006)). The first region from the wall extends to approximately $y^+ = 5$ and is called the viscous sublayer in which $v^+ = y^+$ holds. Between $5 \leq y^+ \leq 30$ is a region called the buffer layer connecting viscous sublayer to a region called the logarithmic layer where the so called law of the wall holds. The upper limit of the logarithmic layer depends on the Reynolds number. The law of the wall for smooth walls is

$$v^+ = \frac{1}{0.41} \ln y^+ + 5.0. \quad (9.23)$$

There are two main approaches used to treat wall regions in turbulent flow calculations. One option is to resolve the boundary layer all the way down to the wall, which requires a calculation mesh that is fine enough to contain cells in the viscous sublayer (a so called low Reynolds number mesh). Another option is the wall function approach, in which the viscous sublayer and the buffer layer are not resolved by mesh but represented by algebraic formulas. The wall function approach then does not require as high near wall resolution from the calculation mesh. In fact, the first calculation point should be located outside the viscosity affected region (wall function mesh). Although the wall function approach is computationally less expensive than the wall resolving approach, they do not perform well in all cases involving separated flows or heat transfer (Patel et al., 1985).

With the low Reynolds number approach the problem in addition to increased computational requirements is that some turbulence model equations are not valid

in the viscous sublayer. While models based on the specific turbulence dissipation rate ω can be solved throughout the boundary layer, the widely used ϵ based models cannot. However, means have been developed to perform wall resolving simulations also with the ϵ based turbulence models.

The approach that is used for the near wall modelling with the ϵ based turbulence models in the CFD solver used in this work is based on a concept referred to as the two layer model (ANSYS Inc., 2013a). In this type of model, the fully turbulent region is solved normally with the $k - \epsilon$ or the RSM and the near wall region is solved using a separate one equation model, specifically one proposed by Wolfstein (1969).

9.3 Turbulent heat transfer modelling

As with the continuity and momentum equations, the instantaneous temperature T can be separated into an average \bar{T} and a fluctuation T' component and the Reynolds averaged energy equation can be formed. The Reynolds averaged form of the energy equation is

$$\frac{\partial}{\partial t} (\rho c_p \bar{T}) + \frac{\partial}{\partial x_i} (\rho c_p \bar{v}_i \bar{T}) = \frac{\partial}{\partial x_i} \left(\lambda \frac{\partial \bar{T}}{\partial x_i} - \rho c_p \overline{v'_i T'} \right) + S_h, \quad (9.24)$$

where the term $-\frac{\partial}{\partial x_i} (\rho c_p \overline{v'_i T'})$ represents the turbulent heat flux and requires modelling as the Reynolds stress term in the time averaged momentum equation. The same approach that was used to model the Reynolds stress term is used with the turbulent heat flux term. A turbulent thermal conductivity λ_t is defined, which is related to the turbulent viscosity through the definition of a turbulent Prandtl number Pr_t . The turbulent thermal conductivity is then calculated as (White, 2006)

$$\lambda_t = \frac{c_p \mu_t}{Pr_t}. \quad (9.25)$$

Contrary to the molecular Prandtl number, which is a material property, Pr_t is a flow property which in reality has some local variation but for which typically a constant value close to unity is used in calculations (White, 2006). The energy equation solved together with the RANS turbulence models introduced above now becomes

$$\frac{\partial}{\partial t} (\rho c_p \bar{T}) + \frac{\partial}{\partial x_i} (\rho c_p \bar{v}_i \bar{T}) = \frac{\partial}{\partial x_i} \left[(\lambda + \lambda_t) \frac{\partial \bar{T}}{\partial x_i} \right] + S_h. \quad (9.26)$$

10 CFD calculation model

A detailed description of the L-STAR facility and the experiments was provided by the experimental team as a research report (Arbeiter et al., 2013b). The report along with the additional suggestions from the experimental team were followed in the preparation of the calculation models for the smooth and roughened rod geometries. This chapter covers the modelling details.

10.1 Geometry and materials

The hexagonal test section channel of the L-STAR facility with short parts of the inlet and outlet piping was selected as the geometric domain for the CFD calculations so that in addition to all the instrumentation in the test section, it also covers the temperature and pressure measurement locations at the flow inlet and outlet. The calculation domain is shown in Figure 10.1. The geometry model for the CFD calculations was built from the CAD drawings of the facility by excluding minor details and parts irrelevant to the CFD simulations.

The rod inside the test section channel consists of an outer shell enclosing the heater cartridge with six individual heater elements separated from each other by short ceramic plugs. The inner structure of the heater elements is presented as well in Figure 10.1. The outer layer of the heater elements is grade DIN 1.4571 stainless steel. Thin heater wires made of NiCr 8020 embedded in a ceramic glue are coiled around a ceramic support layer and the centre of the heater elements is filled with compressed MgO powder. The short plugs separating the heater elements are made of ceramic material C230.

Due to the unfortunate fact that the actual material data of the ceramic support layer and the glue could not be obtained from the manufacturer of the heater elements, a fully detailed replica of the heater elements could not be built for the CFD simulations. Instead, a simplified model was built where all the ceramic materials inside the heaters were homogenised as a single material for which the properties of MgO were used. The heater wires were modelled as a 0.2 mm thick layer surrounded by the ceramic regions. The cross section of the actual heater element and the simplified model are also shown in Figure 10.1.

The top and bottom parts of the rod outside the heater cartridge were modelled as MgO inside the rod outer shell. The outer shell of the rod is made of grade DIN 1.4404 stainless steel while the flow channel is grade DIN 1.4301 stainless steel. As heat conduction in the flow channel walls was not modelled and the steel grades DIN 1.4404 and DIN 1.4571 (heater element shell) have practically identical thermal properties, the material properties of DIN 1.4404 were used for all metal regions, including the resistive wires. Material property data provided by Arbeiter et al. (2013b) was used for all materials, although the validity of the data was verified from additional sources, such as VDI-Wärmeatlas (1988) and Incropera et al. (2006). Temperature dependency of the specific heat capacities and the thermal conductivities of the heater element materials were accounted for while constant

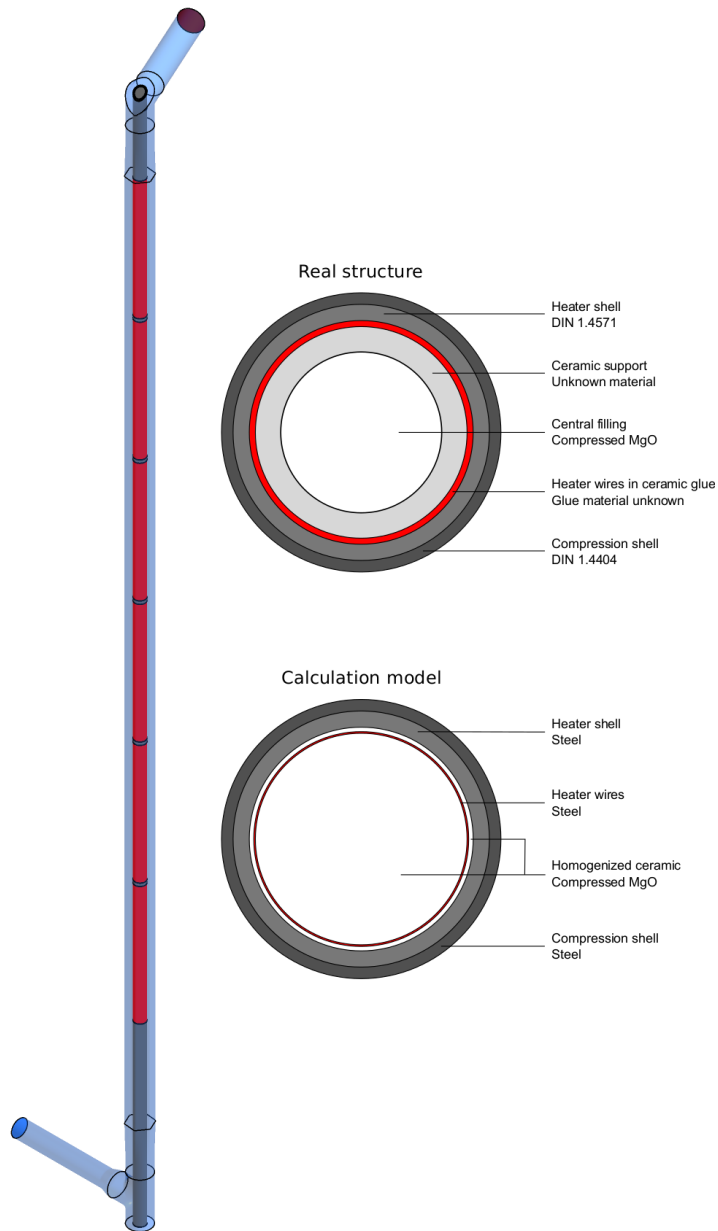


Figure 10.1: Calculation domain consisting of a hexagonal flow channel with the rod inside (left). Flow enters the channel through the pipe at the bottom and leaves through the pipe at the top of the channel. The six heater regions in the rod are highlighted with a red colour. The cross section showing the inner structure of the rod (top right) and the simplified model used in the calculations (bottom right).

properties were used for the insulating C230 plugs.

As the Mach number in the investigated flow range is low, the operating fluid was assumed incompressible. Ideal gas law was used to calculate air density while temperature dependent polynomial functions were used for the specific heat capacity, the dynamic viscosity and the thermal conductivity of air.

10.1.1 Flow conditioner

A flow conditioner consisting of two perforated plates was attached to the bottom part of the test section to improve the uniformity of the flow field in the measurement region where LDA measurements were to be performed. The CAD model of the flow conditioner is shown in Figure 10.2. Due to the additional complexity and increase of mesh elements the detailed inclusion of this part would have introduced to the CFD model, the flow conditioner was not modelled in detail but added into the model as two porous medium regions. The details of the porous model of the flow conditioner will be given later when the cell zone and boundary conditions are discussed.

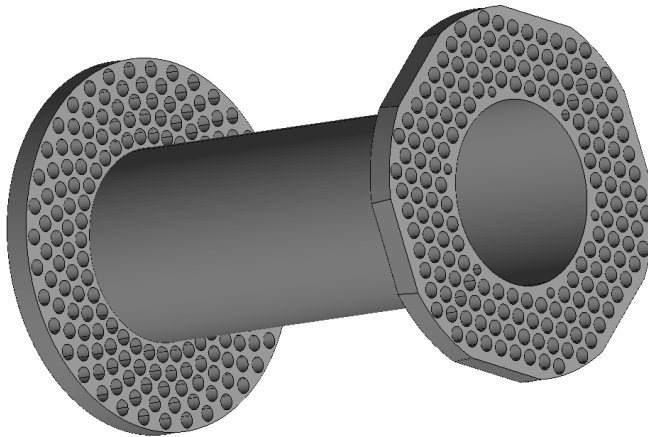


Figure 10.2: CAD model of the flow conditioner located at the bottom part of the test section.

10.1.2 Surface roughness elements

Surface roughness elements with a square cross-section were used to enhance convective heat transfer in the roughened rod cases. A total of 89 rings were attached on the rod surface at regular intervals covering the heated section of the rod. The axial cross section showing the measures of the roughness elements is shown in Figure 10.3. In the calculation model the rings were assumed to be of the same material as the rod surface, that is, DIN 1.4404. Also, no contact resistance between the rod surface and the rings was accounted for.

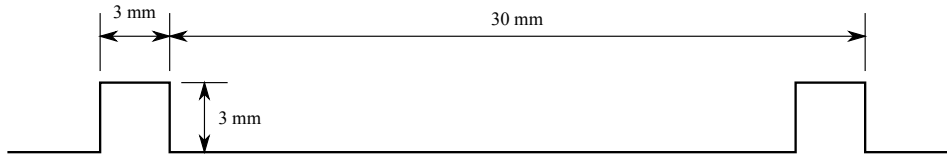


Figure 10.3: The width and height of and the pitch between the square cross section surface roughness elements.

10.2 Calculation mesh

Meshing of the calculation domain was done using the meshing software ANSYS ICEM CFD (ANSYS Inc., 2013d). Fully structured and conformal meshes were constructed for both, the smooth and the roughened rod geometries. This means that also the different material regions inside the rod and the interface between the rod and the fluid regions have continuous mesh lines. Several meshes were made to assess the dependence of the results on the mesh resolution. The results of the mesh dependency studies will be covered in more detail in a later chapter where the reliability of the results is discussed. The meshing approach in general is discussed below.

As obtaining accurate estimations for wall friction and heat transfer coefficients was an objective in this work, wall resolving simulations were pursued as suggested, for example, by Casey and Wintergerste (2000) instead of using a wall function approach. For this reason, so called low Reynolds number meshes were built with the dimensionless wall distance y^+ near or below one. Thus, a very fine mesh near the boundaries was needed. In the smooth rod cases this was achieved with the height of the first cell from the wall being approximately 0.02 mm while for the rib roughened rod the height was reduced at some parts to 0.01 mm. As suggested in best practice guidelines, such as Casey and Wintergerste (2000), the growth ratio between the cells was kept moderate (approx. 1.2) and high aspect ratios in the bulk regions were avoided (high aspect ratios in the wall adjacent cells are unavoidable in the wall resolving approach). In the centre of the flow channel the aspect ratio in the smooth rod case was below 3. In the roughened rod mesh some higher aspect ratio elements were unavoidable also in the bulk regions due to the used meshing approach and refinement due to the ribs. In these mesh cells a maximum aspect ratio of 12 was obtained. The y^+ requirement was adhered strictly on the rod surface and the major part of the test section channel. Maximum y^+ values were seen at the inlet and outlet regions. The near wall resolution is illustrated in Figure 10.4 where the velocity profile scaled by the friction velocity is plotted as a function of y^+ in the case of the smooth unheated rod. It can be seen that a total of seven cell centres lie within the viscous sublayer below $y^+ = 5$ of which two are even below $y^+ = 1$. From this plot it can be concluded that the near wall grid spacing is fine and the overall number of cells high enough for the wall resolving simulations.

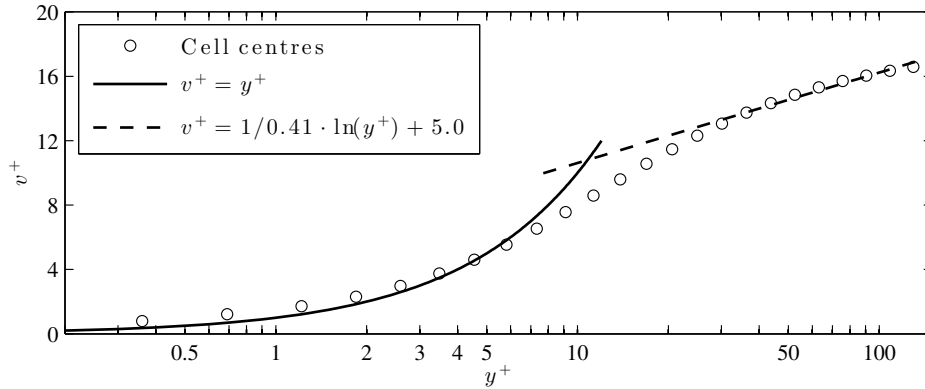


Figure 10.4: Near wall spacing of calculation cells normal to the rod surface for the smooth unheated rod (case 3) calculated with a Reynolds stress model.

The meshes of the smooth and roughened rod models have otherwise identical mesh structures except for the roughness elements in the roughened rod model, which required additional refinement and thus resulted in a significantly higher number of cells. The number of calculation cells in the various meshes is given in Table 11.1. The meshing details at various parts of the domain are shown in Figure 10.5. It is acknowledged that in the vicinity of the roughness elements the mesh is not an optimal one. A small y^+ at the surface around the ribs is obtained but at the same time the structured meshing approach leads to unnecessary refinement in between the consecutive ribs and also between a rib and the channel. A more optimal mesh would be more aligned around the surface roughness structures and have a more even cell distribution growing from the rod surface. This type of mesh optimisation was not done due to the difficulty and time required to construct such a mesh in three dimensions.

10.3 Cell zone and boundary conditions

Nominal conditions defined for the experiments (Arbeiter et al., 2013b) were given for the boundaries and other zones in the calculation domain. An absolute pressure of 0.15 MPa was defined as the operating pressure. A mass flow inlet boundary condition with a specified mass flow rate was defined for the flow inlet. Turbulence conditions were given as a specified turbulence intensity of 5 % and a hydraulic diameter. Uniform profiles for velocity and turbulence were specified. A pressure outlet boundary condition with a zero gauge pressure was defined at the flow outlet. A no slip boundary condition was set for the walls and the domain outer walls were considered adiabatic. The rod outer surface, the roughness elements and the channel surface were also assigned emissivity values for a radiative heat transfer model. For the rod and the roughness elements a value of 0.6 was used while the channel walls

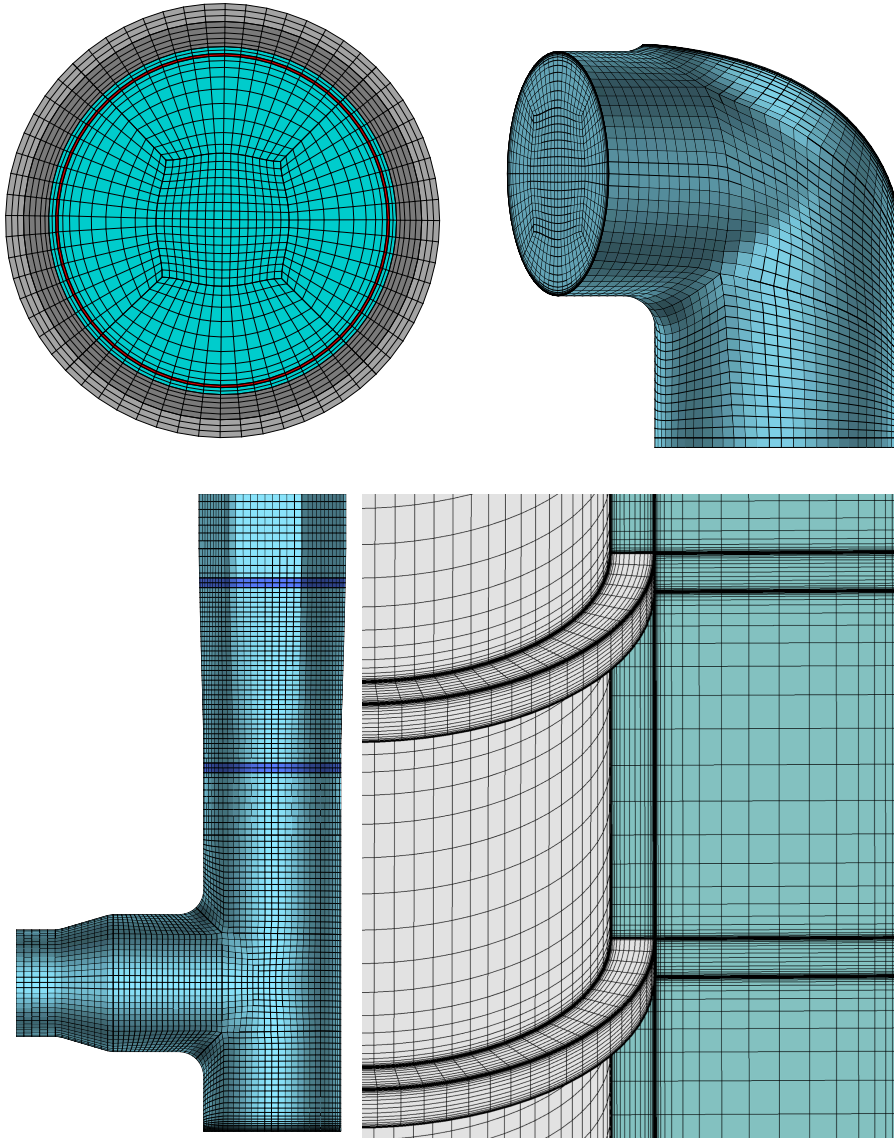


Figure 10.5: Meshing details. Cross section of the mesh of the heated rod showing the different material layers (top left). Mesh at the outlet junction (top right). The surface mesh of the inlet region where the porous medium regions representing the two perforated plates are highlighted with a darker blue colour (bottom left). The mesh around the surface roughness elements (bottom right).

were given a value of 0.25. In cases with the rod heating on, the total heating power was divided equally to the six heater elements and added as energy source terms in the control volumes representing the heater wires. The values of mass flow rates and heating powers in the different cases are given in Table 8.1 .

10.3.1 Porous zones

The flow conditioner was included in the calculation model as two porous medium regions. In the porous medium model of ANSYS Fluent (ANSYS Inc., 2013b), additional momentum source terms are added to the momentum equations. The viscous and inertial resistance coefficients in the porous medium model equations were derived using available pressure drop measurement data for the smooth rod geometry with and without the flow conditioner (R. Gómez, personal communication, December 4, 2013).

The sink terms consist of a viscous and an inertial component. The viscous term is given by (ANSYS Inc., 2013b)

$$\frac{\partial p}{\partial x_i} = -\frac{\mu}{K}v_i, \quad (10.1)$$

where K is the permeability. The inertial part is given by (ANSYS Inc., 2013a)

$$\frac{\partial p}{\partial x_i} = -\frac{1}{2}C\rho|v|v_i, \quad (10.2)$$

where C is the inertial resistance coefficient.

The coefficients K and C were obtained from the measurement data with a method suggested in ANSYS Inc. (2013b). The difference between the pressure drops between the flow inlet and outlet Δp with and without the flow conditioner were calculated and a quadratic function was fitted to the data points so that

$$\Delta p = av^2 + bv. \quad (10.3)$$

The coefficient a in Equation 10.3 represents the inertial term

$$a = \frac{1}{2}C\rho\Delta L \quad (10.4)$$

and the coefficient b represents the viscous term

$$b = \frac{\mu}{K}\Delta L, \quad (10.5)$$

where ΔL is the total thickness of the two perforated plates forming the flow conditioner, that is, the total thickness of the porous medium. From these two equations, the viscous and inertial resistance coefficients can then be solved. Figure 10.6 shows the measured pressure drops over the test section with and without the flow conditioner, their difference and the quadratic curve fitted to the data points.

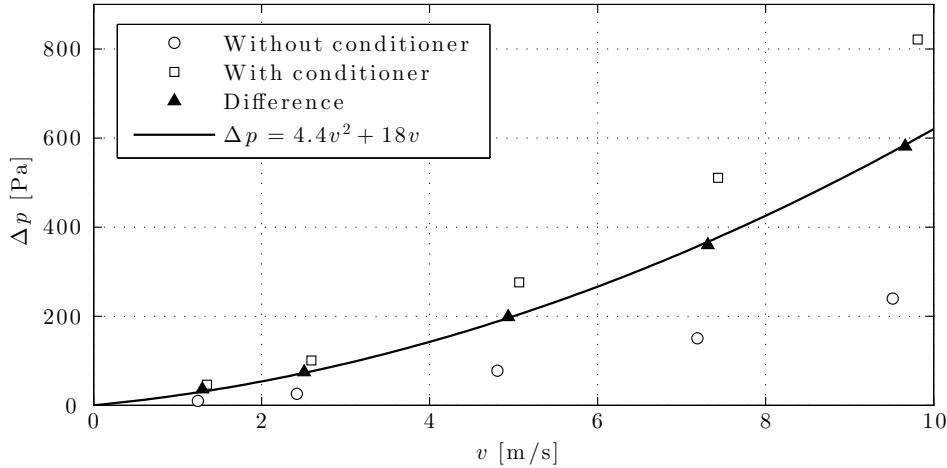


Figure 10.6: Pressure drops measured in the experiments with and without the flow conditioner, their difference and a quadratic function fitted through the data points.

10.4 Turbulence models

The selection of turbulence models in the context of this work was limited to RANS turbulence models which were considered to represent the optimum between computational effort and physical accuracy in the scale of this particular application, that is, the full rod in three dimensions. There is a selection of RANS models available in ANSYS Fluent from one equation Spalart-Almaras model through several variants of the $k - \epsilon$ and $k - \omega$ two equation models to three different Reynolds stress model variants (ANSYS Inc., 2013b). Almost each of these models were tested.

Before any actual simulations it was assumed that the models formulated with the ω equation would show the best performance due to their inherent capability to integrate through the viscous sublayer while ϵ based models need to use a two layer approach and solve the viscous sublayer using a separate one equation model. This would probably be the case when making similar simulations in a more robust geometrical domain. However, it was found out that in this particular geometry the ω based turbulence models could not be converged to a steady state solution with the steady state solver. This was observed as the stalling of the residuals at a high level and as non stabilising oscillations in the monitored solution variables. With additional calculations of the separate regions of the calculation domain, the reason for this behaviour was traced to the inlet region of the geometry where the vertical inlet flow enters the test section channel and hits the rod. It is well known that a fluid flow past a cylinder is inherently unstable and so called oscillating von Kármán vortices (see e.g. White (2006)) are formed behind it. Although in the L-STAR geometry these vortices are damped at the channel walls close to the rod, the slightly unsteady nature of the flow in this region seemed to present an insurmountable

obstacle for the used steady state solver when any ω based turbulence model was used.

The turbulence models based on the ϵ with a two layer approach for the near wall modelling did not suffer from similar convergence problems and could be converged to a steady state solution regardless of the instability at the inlet region. While recognising the unsteady behaviour at the inlet region, it was not considered to affect the results taken far downstream from the inlet in any significant way as long as sufficient convergence could be obtained, which was the case with ϵ based models. For these reasons, the realisable version of the $k - \epsilon$ model and the linear pressure-strain Reynolds stress model were selected from the available turbulence models for the final calculations.

In the ϵ models in Fluent the near wall modelling without wall functions is implemented as a part of the so called enhanced wall treatment (EWT) model. The EWT determines whether to use wall functions or to resolve the viscous sublayer based on the y^+ value of a near wall cell. By ensuring that the calculation mesh has a sufficient resolution near the walls, one can ensure that the EWT uses the wall resolving approach. EWT is available and was used in both the realisable $k - \epsilon$ as well as the RSM calculations.

10.5 Heat transfer models

In the heated rod calculations the energy equation was included in the calculation model. As the rod internals were modelled in detail and the heating was included as energy source terms in the solid mesh cells representing the heater wires, the energy equation was also solved in the solid regions.

Radiation heat transfer was included in the model between the rod and channel surfaces. It was assumed that the absorption to the coolant air would not be significant in this case and thus the surface to surface (S2S) radiation model was selected. The S2S model only considers radiative heat exchange between surfaces and assumes the medium to be fully transparent (ANSYS Inc., 2013a). As an additional input, the radiation model requires view factors between participating surface mesh faces which were calculated before the actual CFD simulation with an additional tool provided along the CFD solver.

10.6 Solver and numerical methods

Calculations were done with ANSYS Fluent 15.0 utilising distributed memory parallelisation in a computer cluster. The solver details and the used discretisation schemes are summarised in Table 10.1.

It was necessary to slightly modify the under relaxation parameters in some cases to converge the simulations. The modification of the under relaxation coefficients was done case dependently and no specific values suitable for all cases were found.

Table 10.1: Solver settings and discretisation schemes used in the calculations.

Parameter	Setting
Solver	
Dimension	3D
Options	Single precision
Type	Pressure based
Time	Steady state
Velocity formulation	Absolute
Discretisation	
Pressure-velocity coupling	SIMPLE
Gradient	Least squares cell based
Pressure	Second order
Momentum	Second order upwind
Turbulent kinetic energy	Second order upwind
Turbulent dissipation rate	Second order upwind
Energy	Second order upwind
Reynolds stresses	Second order upwind

11 CFD calculation results

To allow better comparison with literature correlations as well as experimental results with the boundary conditions slightly deviating from the nominal values, the results obtained from the CFD calculations are presented in dimensionless form. Thus, the dimensionless parameters used to present the results along with the result extraction locations are defined below. To have confidence in the calculation results it is important to assess their numerical reliability and therefore the mesh and the iteration convergences are discussed next. After these preliminaries, the CFD results are given with comparisons to the corresponding experimental results.

11.1 Data extraction locations and dimensionless parameters

Data was extracted from the locations that were specified as measurement locations in the related experiments (Arbeiter et al., 2013b). These locations are shown in Figure 11.1. A radial trajectory is specified for plotting the gas velocity and temperature profiles which start from the rod surface and end to a side of the hexagonal channel. Axially these profiles are taken in the vicinity of z'_2 which corresponds to the centre of the upper optical measurement window installed into the test section. There is also a second measurement window position at z'_1 , which is not used for data extraction in this work. Pressure differences are taken either over the whole test section between p_1 and p_2 , or between the pressure measurement locations p'_1 and p'_2 which are at slightly different axial elevations than z'_1 or z'_2 . In general, the subscript 1 denotes the value at, or closer to, the flow inlet while the subscript 2 is used to refer to the flow outlet. The position of the fifth heater element is highlighted in Figure 11.1 as this region is used to calculate average Nusselt numbers.

Calculated pressure differences are used to derive friction factors between p'_1 and p'_2 and total loss coefficients through the test section between p_1 and p_2 . The frictional losses between the test section windows are characterised by Darcy friction factor (see e.g. White (2003)). It is calculated as

$$f_D = 2 \frac{p'_2 - p'_1}{\rho_1 v_m^2} \frac{d_h}{\Delta z}, \quad (11.1)$$

where d_h is the hydraulic diameter and Δz is the axial length between p'_1 and p'_2 . Density is evaluated at the flow inlet conditions and a mean velocity is used which is calculated based on the mass flow rate \dot{m} and the nominal flow channel cross section A_c as

$$v_m = \frac{\dot{m}}{\rho_1 A_c}. \quad (11.2)$$

The total loss coefficient is calculated over the whole test section as

$$C = 2 \frac{p_2 - p_1}{\rho_1 v_m^2}. \quad (11.3)$$

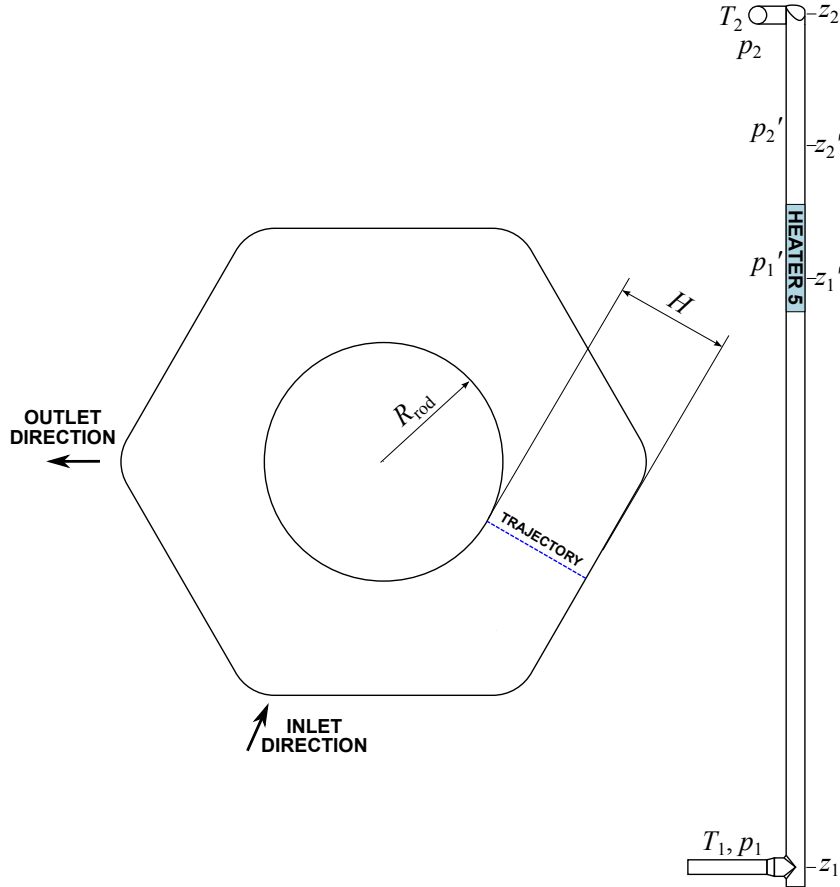


Figure 11.1: Trajectory along which profiles are plotted inside the flow channel (left) and the axial positions from which data is extracted (right).

The average Nusselt number is extracted from the axial length of one heated rod segment (Heater 5). The area-based average of the rod surface temperature T_s is calculated from the wall cell faces and the heat fluxes (convection and radiation) through the same cell faces are extracted. A bulk temperature T_b for the gas is calculated as the volume average of the calculation cells inside the channel around the heater segment. The hydraulic diameter of the flow channel is used as the characteristic length. The Nusselt number is then calculated based on either the total heat flux q''_{tot} or only the convection heat flux q''_{con} as

$$Nu = \frac{q'' d_h}{(T_s - T_b) \lambda}, \quad (11.4)$$

where the thermal conductivity λ is calculated from the fluid calculation cells in the

same way as T_b .

When compared with the Nusselt numbers derived from the experiments it should be noted that a more approximate method was used for calculating Nu from the experimental results. In the experimental Nusselt number the gas bulk temperature was estimated based on the gas inlet temperature and the heat delivered to the gas below the measurement height of the single thermocouple that was used to estimate the rod wall temperature (Gómez et al., 2014a). The experimental Nu naturally includes radiation heat fluxes. It is possible to use more exact methods to calculate the Nusselt number and also to calculate the contribution of radiation heat fluxes from the CFD data. As using identical Nu definition with the experiments would basically reduce to comparing temperatures of a single thermocouple measurement point, which is done anyway by comparing the rod temperature distributions, the more exact method to obtain Nu from the calculations was used.

11.2 Numerical reliability of the results

The numerical reliability of the calculations should be assessed before making any conclusions from the results. The numerical error in the solution of a CFD simulation decreases as the resolution of the calculation mesh is increased. Thus, calculations should be made with several meshes of increasing resolution. This is important even if not to find the mesh resolution at which mesh independent results are obtained, but at least to be able to quantify the error in the simulation results if a coarse mesh needs to be used because of limitations in the available computational power. Another thing affecting the reliability of the results is the simulation convergence. It needs to be ensured that the solution variables have converged and sufficient number of iterations have been performed.

11.2.1 Mesh convergence

Three meshes were built for the smooth rod geometry to investigate the effect of mesh resolution on the results. The number of cells was approximately doubled between the consecutive meshes and the mesh refinement was done in each direction (i.e. radial, tangential and axial). The resolution of the three meshes is visualised in Figure 11.2 and the exact number of elements are given in Table 11.1. The mesh sensitivity analyses were done with the RSM model for the heated rod case 1 (see Table 8.1). As can be seen from Figure 11.3, the profiles obtained with the coarse mesh have a slight deviation from those obtained with the medium and dense meshes, which have virtually overlapping profiles. The gas temperature profiles show a slight temperature increase towards the outer wall, which is due to the radiative heat transfer from the rod surface heating the outer wall. Similarly, it can be seen in Table 11.2 that the obtained Nusselt numbers with the medium and fine meshes are practically identical.

Table 11.1: Number of calculation cells in the meshes used in the mesh dependency analysis. The meshes used to obtain the actual results are highlighted with a bold typeface.

Mesh	Fluid elements	Solid elements	Total elements
<i>Smooth rod</i>			
Coarse	1,666,944	1,361,408	3,028,352
Medium	3,901,860	2,140,920	6,042,780
Dense	7,204,516	4,825,832	12,030,348
<i>Rough rod</i>			
axisymmetric coarse	23,256	14,904	38,160
axisymmetric medium	37,471	37,793	75,264
axisymmetric dense	87,980	62,485	150,465
Full 3D mesh, medium	9,663,680	7,278,464	16,942,144

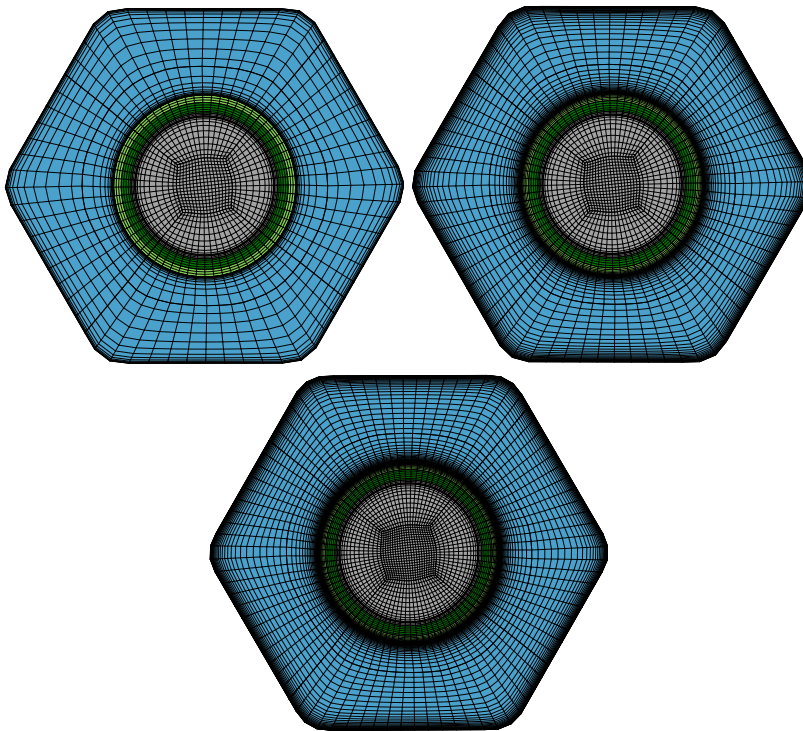


Figure 11.2: Cross sections from the flow channel and the rod visualising the coarse (top left), the medium (top right) and the fine (bottom) meshes used in the mesh dependency analysis for the smooth rod geometry.

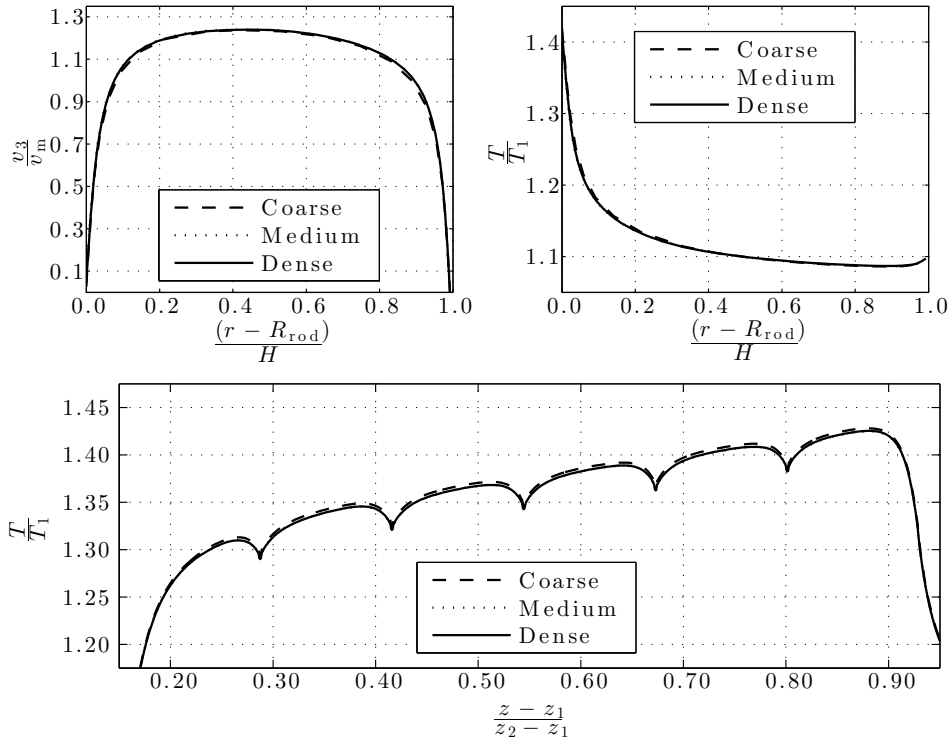


Figure 11.3: Velocity (top left) and temperature (top right) profiles at the flow channel and rod axial temperature profile (bottom) calculated with three different mesh resolutions for the smooth rod geometry.

A simplified mesh sensitivity analysis was done for the roughened rod geometry because of the constraints set by the number of available software licences (which limit the amount of parallel processes that can be used) and the time available for the simulations in general. A low Reynolds number mesh for the rib roughened rod inevitably requires much more calculation cells than a mesh for the smooth rod. In addition, a much slower convergence was observed with the roughened rod geometry and for the aforementioned reasons the mesh used for the roughened rod calculations was limited to approximately 17 million cells. However, to have at least some apprehension of the adequacy of the mesh, a simplified axisymmetric representation of the test section over a single heater section with a total of 13 ribs was constructed. This geometry was then meshed with the same axial and radial resolution as the mesh of the full three dimensional geometry and with half and double resolutions. The number of calculation cells in these axisymmetric meshes and the full three dimensional mesh is given in Table 11.1. A mesh dependency analysis was then performed with these axisymmetric meshes using similar flow and

heating parameters as in the actual full size simulations and realisable $k-\epsilon$ model for turbulence. The gas velocity and temperature profiles and the rod axial temperature profiles calculated with the three axisymmetric meshes are shown in Figure 11.4 and the Nusselt numbers in Table 11.2. It can be seen that there are more differences between the profiles and Nusselt numbers obtained with different meshes. However, the rod temperature profiles obtained with the medium and dense axisymmetric meshes are very close to each other. Due to the simplified mesh dependency analysis considering only one heater with axisymmetric representation, it is possible that the differences in the results obtained with the meshes of similar resolution in a full three dimensional model could be somewhat larger. However it is considered unlikely that these differences would be drastically larger. On this basis it is concluded that the results obtained with the full three dimensional calculation mesh with the medium resolution are likely to include a slight numerical error introduced by the mesh.

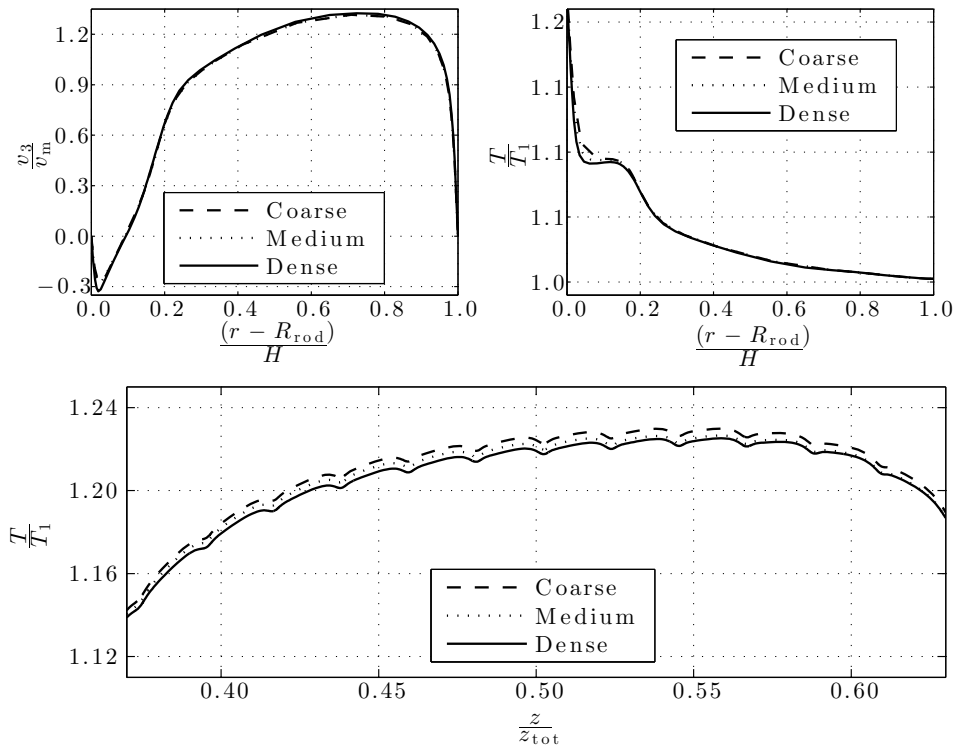


Figure 11.4: Velocity (top left) and temperature (top right) profiles at the flow channel and rod axial temperature profile (bottom) resulting from the simplified mesh dependency analysis with three axisymmetric meshes for the rough rod.

Table 11.2: Effect of mesh resolution on the calculated Nusselt number.

	Coarse	Medium	Fine
Smooth rod	54.04	54.66	54.68
Rough rod (axisymmetric)	73.11	74.13	75.03

11.2.2 Iteration convergence

Several parameters were monitored during the calculations to ensure converged results were obtained. The solver outputs the residuals of the solution variables at specified iteration intervals. The residuals provide one way to monitor solution convergence. By default the solver has pre-specified convergence criteria based on the residual values. However, the default convergence criteria are rather loose and in many cases the solution is not even near an actual convergence when the default convergence criteria are met.

To have more confidence that converged solutions were obtained, additional things were monitored during and after the simulations. These included checking that the integral mass and heat balances were satisfied and monitoring point values of the solution variables at several locations. Thus, the solution convergence was determined based on not only the residuals reaching a level well beyond the solver default level, but also the balances being satisfied and the solution variables remaining at a constant level in successive iterations. An example of the evolution of residuals and temperature and velocity values at monitored locations is shown in Figure 11.5 for a case calculated with the RSM turbulence model. It can be seen especially from the monitored velocity that over 10,000 iterations were needed to reach convergence. The calculations done with the realisable $k - \epsilon$ for the smooth rod geometry generally required much less iterations (approx. 3000). The convergence of the roughened rod geometry with the realisable $k - \epsilon$ required considerably more iterations than the smooth rod (from 10,000 to even 30,000). This slower convergence together with the available software licenses restricting the number of parallel processes¹ was the main reason limiting the number of mesh elements for the simulations. The slow convergence also made it practically impossible to perform the roughened rod simulations with the RSM turbulence model. To give some idea of the required calculation time, approximately 420 CPU hours were required to perform the 3000 iterations in the smooth rod cases calculated with the realisable $k - \epsilon$ model. When using 16 processors this corresponds to roughly one day of real time.

¹There was a cluster of 32 computing nodes with a total number of 448 processor cores (Intel Xeon X5650 and Intel Xeon E5-2600) with a total amount of 3,200 GiB of memory available for the calculations so computer resources were not the bottleneck.

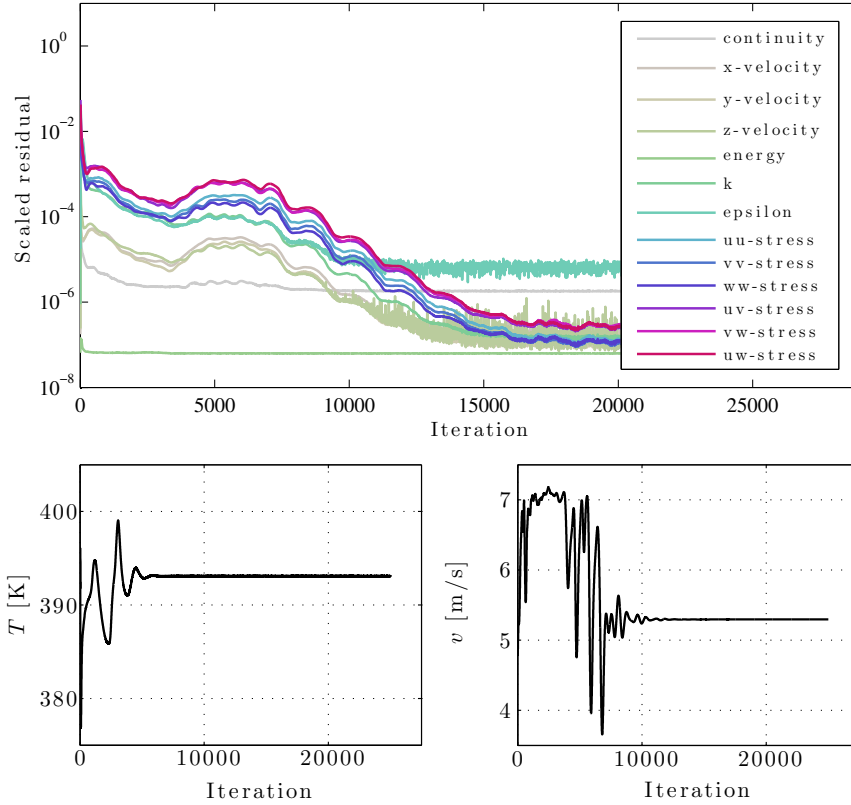


Figure 11.5: Evolution of residuals (top) and rod temperature (bottom left) and gas velocity (bottom right) at monitor points in a smooth rod case calculated with an RSM turbulence model.

11.3 Results and comparisons with experimental data

The results of the CFD calculations of the L-STAR test section with a smooth and roughened rod are presented in the following. Comparisons with the corresponding experimental data are included. It should be noted that for the heated rib roughened rod only cases with different Reynolds numbers were calculated, that is, Cases 1, 4 and 5 (see Table 8.1). Unfortunately optically measured velocity profile data was not available so that more detailed comparisons could have been made.

11.3.1 Total loss coefficients

The flow conditioner introduced into the lower part of the test section causes the major part of the pressure losses as can be seen in Figure 10.6. As the conditioner was modelled using porous media zones to represent the two perforated plates forming the conditioner, the comparison of loss coefficient results calculated with CFD with

the ones obtained from the experiments generally show the calibration accuracy of the resistance coefficients used for the porous media model to obtain a realistic pressure drop through the conditioner.

The total loss coefficients calculated over the test section are plotted for the unheated and heated cases in Figure 11.6. It can be seen that the CFD results are in a relatively good match with the values obtained from the experiments, although there is some over-prediction of C with the lower Reynolds numbers. There are no significant differences between the results obtained with the realisable $k - \epsilon$ and the RSM turbulence models in the smooth rod cases.

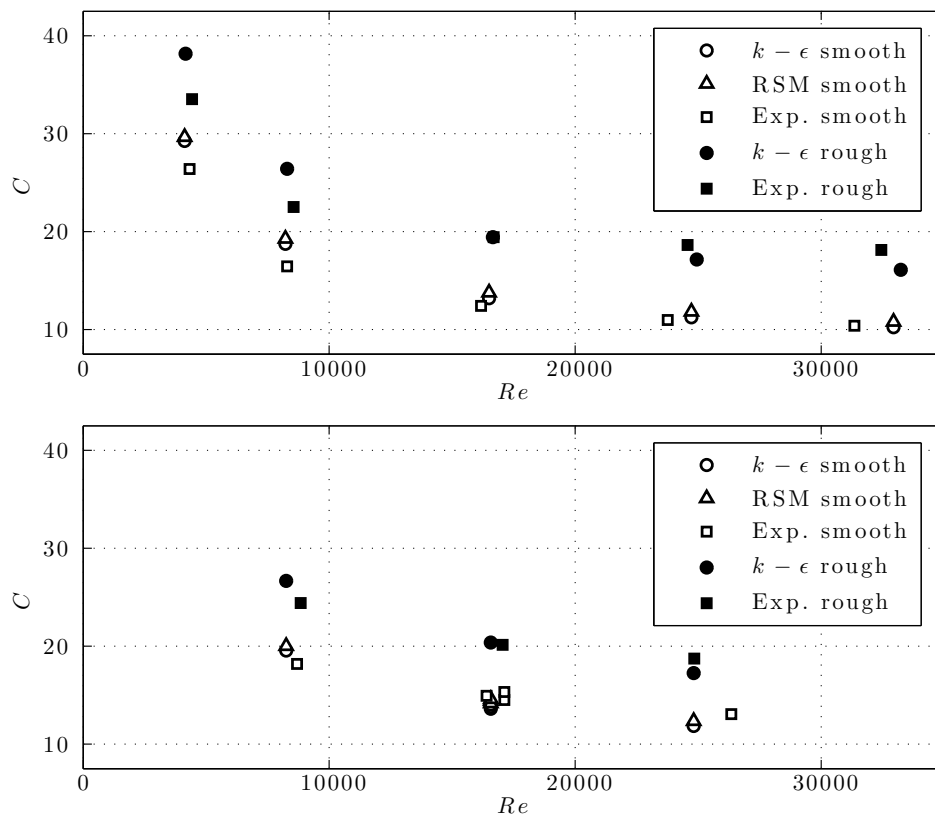


Figure 11.6: Total loss coefficient over the test section for the unheated (top) and heated (bottom) cases calculated with the realisable $k - \epsilon$ for smooth and rough rod geometry and also with an RSM turbulence model for the smooth rod. Experimental results are by Gómez et al. (2014a).

11.3.2 Friction factors

Friction factors calculated based on the pressure difference over the measurement positions p'_1 and p'_2 defined in Figure 11.1 are plotted for the unheated cases in Figure 11.7 and for the heated cases in Figure 11.8. The high experimental uncertainty in the low Reynolds number cases is due to the offset affecting the differential pressure measurements $p'_2 - p'_1$ at low mass flow rates (Arbeiter et al., 2013a). The friction factors calculated for the smooth rod are in a rather good agreement with the measured ones. There are also no significant differences between the results obtained with the two different turbulence models. In the rough rod cases the calculated friction factors are underestimated but they are still within or close to the measurement uncertainties. Heating has a slightly increasing effect on the friction factors as can be seen by comparing the heated and unheated results but the difference between the CFD and experimental results in the heated cases is similar to the unheated ones. The average ratio between the friction factors of rough and smooth cases for the experiments can be calculated as 4.8, while the simulations predict this ratio to be 3.6.

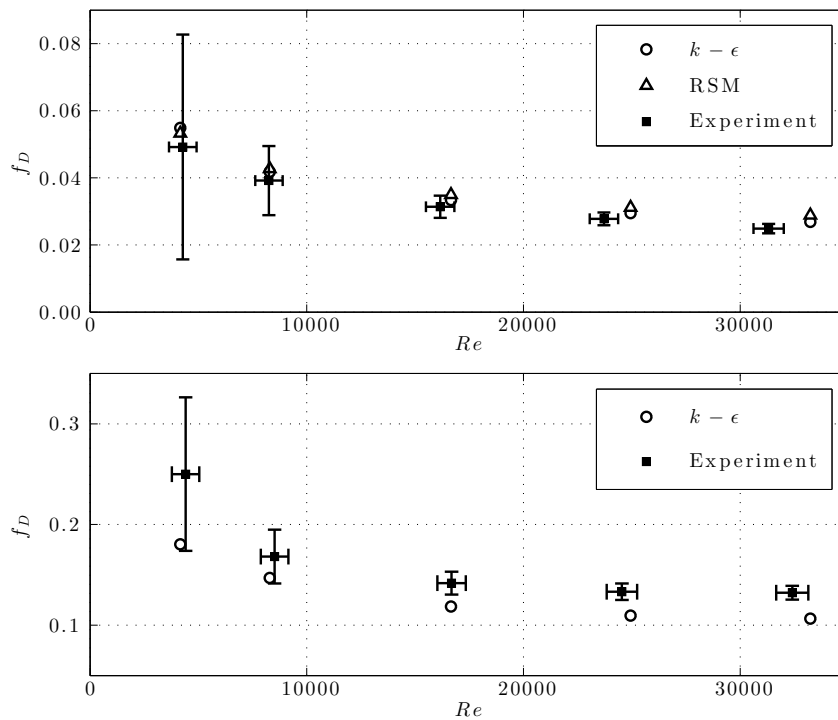


Figure 11.7: Friction factors for the unheated smooth (top) and rough (bottom) rod cases. Experimental results are by Gómez et al. (2014a).

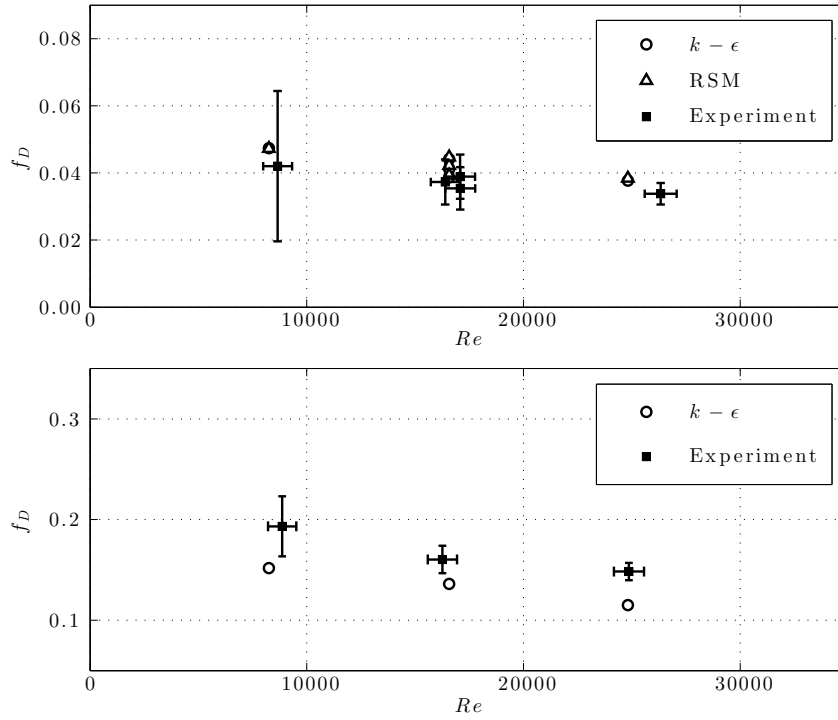


Figure 11.8: Friction factors for the heated smooth (top) and rough (bottom) rod cases. Experimental results are by Gómez et al. (2014a).

11.3.3 Nusselt numbers and rod temperature profiles

Average Nusselt numbers obtained from the calculations with varying Reynolds numbers and heating rates are shown in Figure 11.9 and the rod surface temperatures in Figure 11.10 and 11.11. The Nusselt numbers are calculated based on the total heat flux and on the convective heat flux through the rod surface to see the contribution of radiation heat transfer. In Figure 11.9, also the Nusselt number correlation by Gnielinski (1976) is plotted for reference, which gives the Nusselt number as

$$Nu = \frac{(f/8)(Re - 1000)Pr}{1 + 12.7(f/8)^{1/2}(Pr^{2/3} - 1)}, \quad (11.5)$$

where the friction factor for a smooth surface is calculated from

$$f = (0.79 \ln Re - 1.64)^{-2}. \quad (11.6)$$

The correlations can be used when $0.5 < Pr < 2000$ and $3000 < Re < 5 \cdot 10^6$ (Incropera et al., 2006).

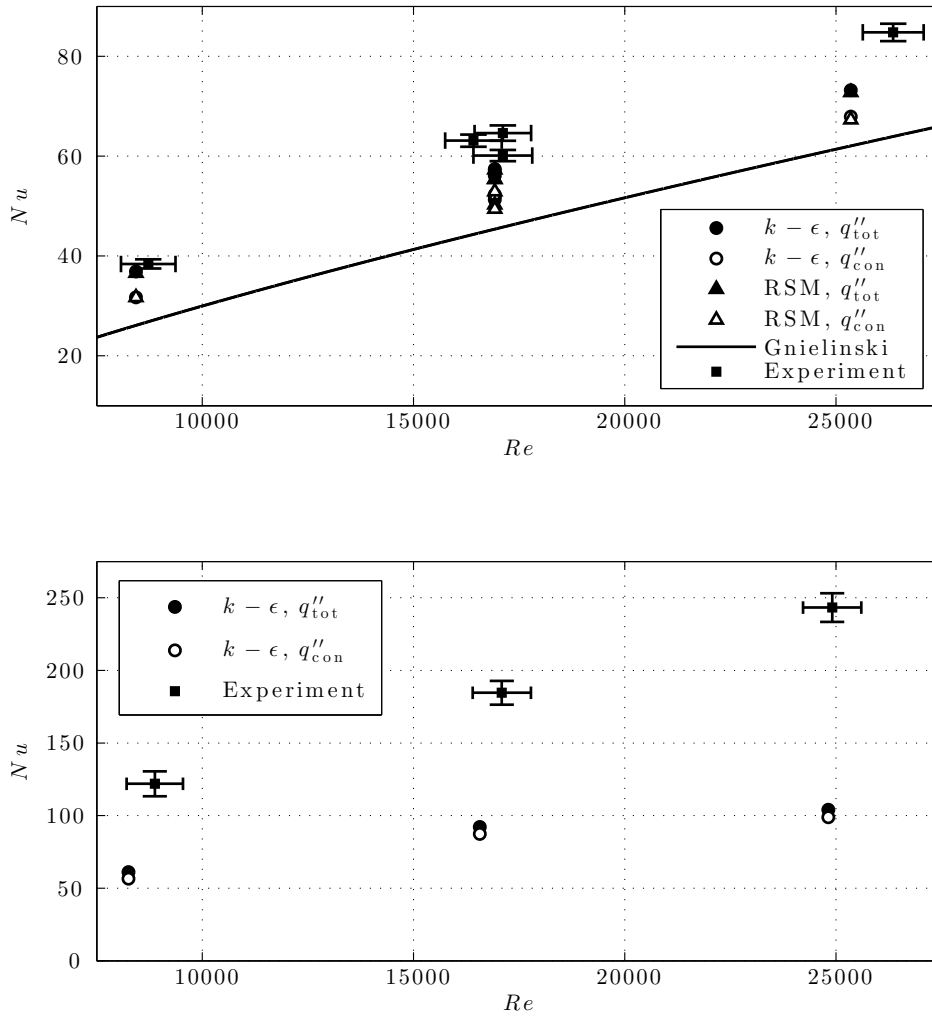


Figure 11.9: Nusselt numbers of the smooth rod calculations compared with experimental results and the correlation by Gnielinski (1976) (top) and the Nusselt numbers of the roughened rod compared with the experimental results (bottom). Experimental results are by Gómez et al. (2014a).

For the smooth rod, both experiments and calculations give Nusselt numbers somewhat higher than the Gnielinski correlation predicts. In the experimental results the radiative heat transfer is included in the heat flux that is used to calculate the Nusselt numbers while from the CFD data it is straightforward to separate the convective and radiative parts. On the average the radiative part in the heat flux increases the Nusselt number by five. There is no significant difference between the

results obtained with the two different turbulence models. Also, overlapping rod axial temperature profiles for the smooth rod cases were obtained with the realisable $k - \epsilon$ and RSM models so only the profiles calculated with the realisable $k - \epsilon$ model are presented in Figures 11.10 and 11.11. The calculated rod surface temperature profiles follow the form of the experimentally obtained profiles but are somewhat overestimated. Depending on the case, this overestimation ranges from approximately 10 K (low heating cases) to almost 20 K (high heating cases). The unheated gaps between the heater elements can be seen clearly in the profiles obtained with CFD and even in the experimental measurements, as one thermocouple was located in such a position (approximately at axial position 0.8 in the profiles).

In the roughened rod cases, the Nusselt numbers are highly underestimated by the CFD calculations and the difference increases with increasing Reynolds number. Correspondingly the rod surface temperatures are drastically overestimated. Again the temperature profiles have the same general form as measured in the experiments and in addition to the locations of the unheated gaps, the individual roughness elements can be seen as small ripples in the profiles.

While at least partly the discrepancies between the experimental and calculated heat transfer results can be covered by unaccounted heat losses, experimental uncertainties and in the roughened rod case also the uncertainty related to the mesh resolution, it is quite apparent that the turbulent heat transfer is poorly predicted in the CFD simulations especially for the roughened rod. With available measurement data of the actual inlet and outlet temperatures (T_1 and T_2) for the smooth rod experiments (Arbeiter et al., 2013a) it is possible to estimate the heat losses by

$$\dot{Q}_{\text{losses}} = \dot{m} (c_{p,1}T_1 - c_{p,2}T_2) + \dot{Q}_{\text{heating}}, \quad (11.7)$$

where \dot{Q}_{heating} is the power delivered by the rod heaters. Based on the values of \dot{m} , T_1 , T_2 and \dot{Q}_{heating} given by Arbeiter et al. (2013a), heat losses for the smooth rod cases were calculated using Equation 11.7. The estimated heat losses are given in Table 11.3. In preliminary calculations of the smooth rod cases the estimated heat losses were included into the calculation model as constant heat flux through the flow channel walls. This decreased the rod surface temperatures very close to the measured temperatures but led to a somewhat tilted axial temperature profile. Due to this distortion, the losses were not included in the calculations presented in this work.

Table 11.3: Estimated heat losses in the heated smooth rod experiments.

	Case 1	Case 2	Case 3	Case 4	Case 5
\dot{Q}_{losses} [W]	139.8	58.9	127.5	71.5	90.1

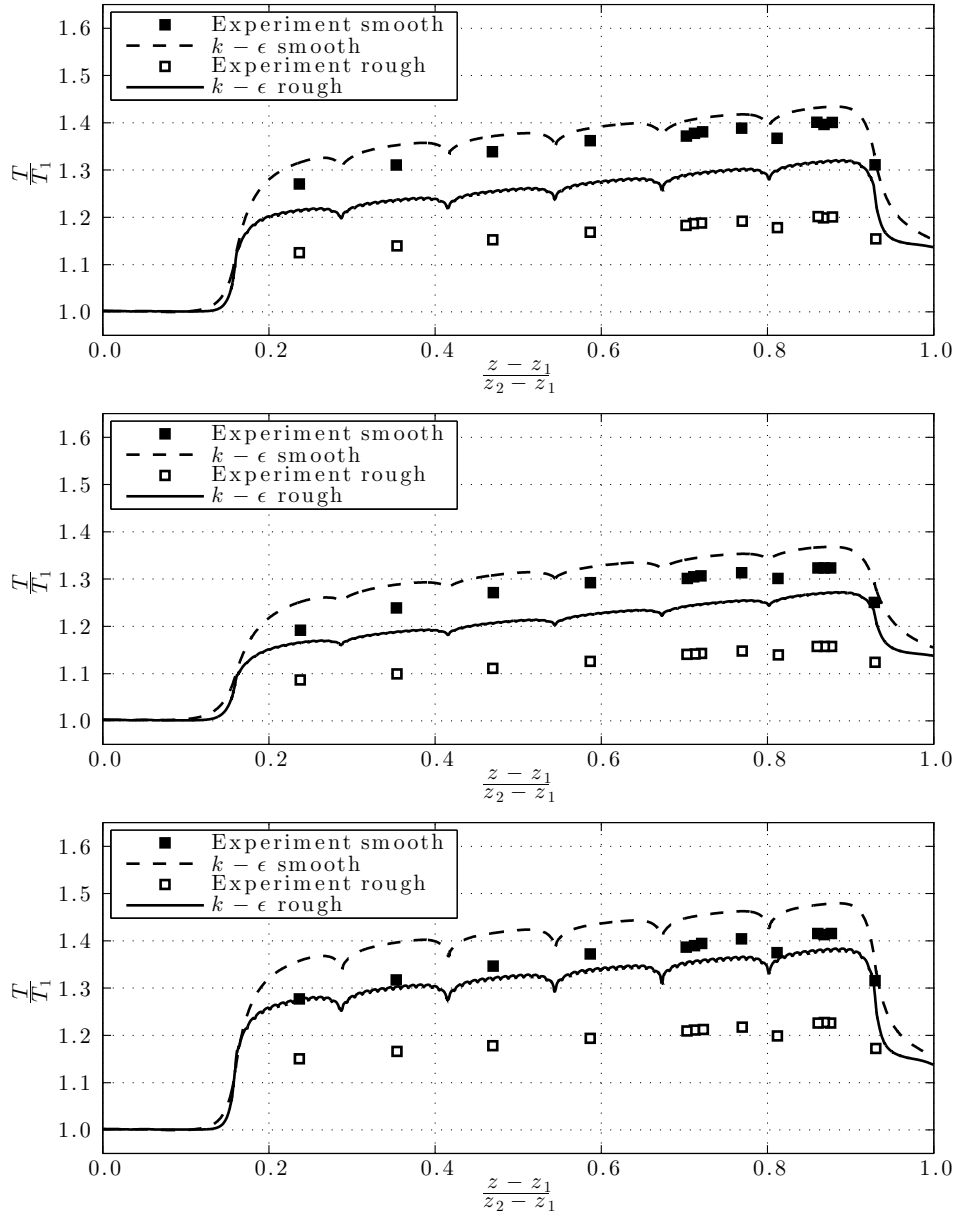


Figure 11.10: Rod temperature profiles for the heated smooth and rough rod cases 1 (top), 4 (middle) and 5 (bottom). Experimental results are by Gómez et al. (2014a).

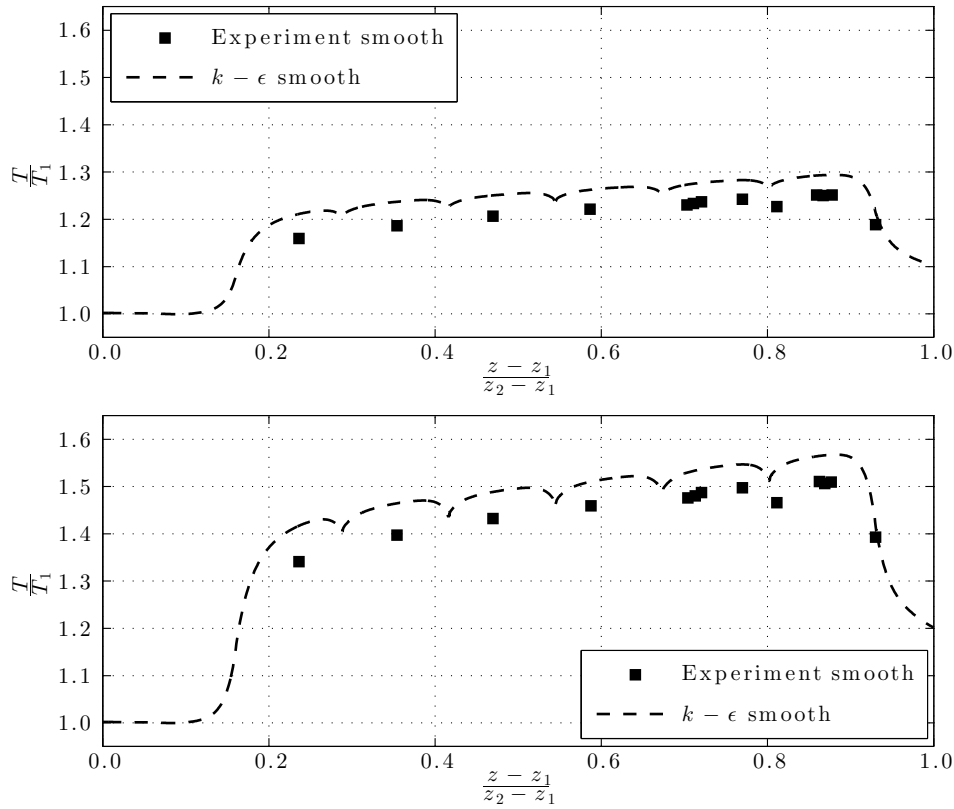


Figure 11.11: Rod temperature profiles for the heated smooth rod cases 2 (top) and 3 (bottom). Experimental results are by Gómez et al. (2014a).

As RSM calculations of the roughened rod cases proved out to be practically impossible to converge, it was not possible to see how the switch from eddy viscosity based turbulence modelling to Reynolds stress modelling would have affected the results. However, alternatives were searched for to have at least some apprehension how using a more advanced turbulence model would affect the heat transfer results. As an alternative to full Reynolds stress modelling, a non-linear eddy viscosity model $v^2 - f$ (Durbin, 1995) available in the used CFD solver with additional license² was tested. This model is a four equation turbulence model that is based on the $k - \epsilon$ model but includes additional equations for the velocity variance scale $\overline{v^2}$ and the elliptic relaxation function f . Unlike $k - \epsilon$, it is capable of accounting for near wall anisotropy and non-local pressure-strain effects. The model has been found out to be more accurate for separated flows as the low Reynolds number $k - \epsilon$ model

²A trial license for $v^2 - f$ turbulence model was obtained for a short period of time making it possible to perform a few calculations.

(White, 2006). A detailed description of the model is given in ANSYS Inc. (2013c).

A calculation with v^2-f model was performed for the heated rod case 5 which had the highest Reynolds number and heating rate. The v^2-f model proved out much easier to converge than the RSM model although not quite as perfect convergence was obtained as with the realisable $k-\epsilon$ as slight oscillation in velocity at a monitor point located at the flow outlet remained. The rod temperature profile resulting from the v^2-f calculation is shown in Figure 11.12. It can be seen that significantly lower rod surface temperatures are obtained when compared to the profile obtained from the realisable $k-\epsilon$ calculation. The corresponding Nusselt number for the v^2-f calculation is 165 when the realisable $k-\epsilon$ estimated a Nusselt number of 104.

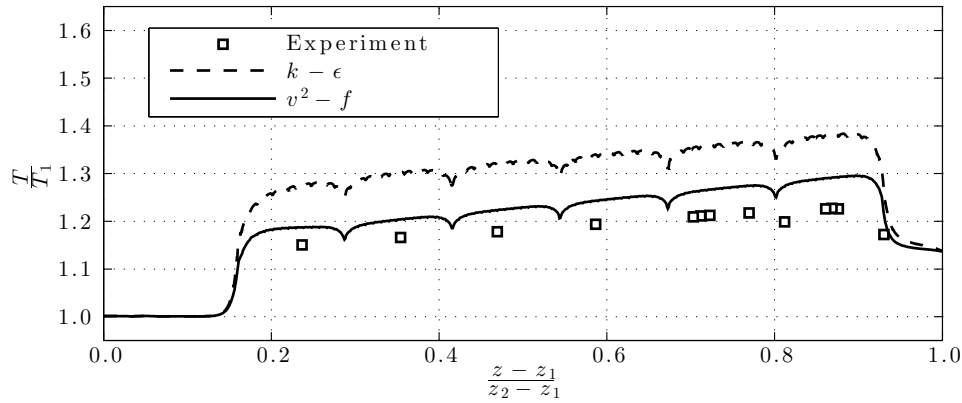


Figure 11.12: Rod temperature profile for the heated roughened rod case 5 obtained with the v^2-f turbulence model. The profile obtained with the realisable $k-\epsilon$ model is plotted for reference. Experimental results are by Gómez et al. (2014a).

12 Summary and conclusions of Part II

Due to the specific features of gas cooled reactors designed for fast neutron spectrum, additional measures are needed to ensure satisfactory heat transfer between the coolant gas and the fuel. One option is to cover the heat transfer surfaces, such as fuel rods, with ribs that induce turbulence and thus augment heat transfer. This will at the same time increase pressure losses and thus some optimisation is needed. CFD calculations provide a cost effective way to investigate this issue, however, before any reliable conclusions can be made based on the results obtained with CFD, the models need to be validated for the specific application.

Three dimensional steady state CFD calculations were performed in conjunction with related experiments for an air cooled rod geometry inside a hexagonal flow channel with the objective to validate CFD models for GFR related analyses. The calculations included investigations for a smooth and a rib roughened rod with and without heating. Calculations were done with the ANSYS Fluent CFD software using the Reynolds averaged turbulence models available in the solver. Due to slightly unsteady behaviour at the flow inlet region, ω based turbulence models turned out to be impossible to converge with the steady state solver. Thus, calculations for the smooth rod geometry were done with turbulence models based on the turbulence dissipation rate, namely the realisable $k-\epsilon$ and the linear pressure-strain RSM. Also due to the significantly slower and elusive convergence with the RSM model in the roughened rod cases this geometry was investigated mainly with the $k-\epsilon$ model, although a single calculation was performed with the v^2-f model.

To avoid making wrong conclusions because of possible numerical error in the results the mesh dependency of the results was investigated using different mesh resolutions. In the roughened rod case this was done using a simplified approach due to external constraints. Also, during the iterative solution process several variables were monitored to be sure that conclusions were made of fully converged results.

Results characterising the pressure losses were in a rather good agreement with the experimental ones; smooth rod results being in a somewhat better agreement. Heat transfer was underestimated in both geometries which was seen as lower average Nusselt numbers and higher rod temperatures than obtained in the experiments. The underestimation of heat transfer in the smooth rod cases can be partly explained by heat losses, which were not accounted for in these calculations but were quantified. Partly the differences between the measured and calculated results can also be due to the uncertainties, for example, in the heated rod composition. The results for the smooth rod are in line with ones obtained by other investigators who have participated the same calculation benchmark using other CFD codes (see, e.g., Gómez et al. (2014b) and Matulik et al. (2014)). No significant differences between the $k-\epsilon$ and the RSM model were seen in the results of the smooth rod cases.

In the rib roughened geometry the realisable $k-\epsilon$ model severely underestimates heat transfer as the average Nusselt numbers are from 2 to almost 2.5 times lower than the ones obtained experimentally. Correspondingly the rod surface temperatures are much higher than the measured ones. Backed up by similar experience

with eddy viscosity based turbulence models and much improved results obtained using an explicit algebraic Reynolds stress model (EARSIM) together with a lower-than-default turbulent Prandtl number of 0.65 in the in-house CFD analyses by the research group performing the experiment (M. Böttcher, personal communication, July 23, 2014), it seems most likely that the main reason for the discrepancies between the calculated and experimentally obtained results is in the turbulence modelling. Indeed, a significant improvement in the predicted heat transfer was obtained when a non-linear eddy viscosity model $v^2 - f$ was tested. Incorrect prediction of the flow separation due to the ribs and reattachment to the rod surface is most likely the main reason for the poor results obtained with the realisable $k - \epsilon$ model. Although envisaged for the L-STAR experiments, velocity profile data measured with optical methods was not available for a more detailed comparison. This type of data would be valuable in future for more detailed model validation to investigate the flow structures in the vicinity of the ribs.

Inclusion of radiation heat transfer was found out to have some effect on the results as it decreased the rod surface temperatures and slightly adjusted the axial temperature profiles to be more aligned with the experimentally obtained profiles. In the roughened rod with more correctly estimated turbulent heat fluxes the contribution by radiation would, however, be lower.

Based on the comparisons between the results obtained with CFD calculations and experimental measurements it seems that further work is needed to improve the heat transfer predictions in this type of application before CFD can be used to make any conclusions regarding the heat transfer performance of rib roughened fuel rod geometries. In further related investigations it is suggested, if possible, to avoid the need to model additional geometry features, such as the inlet junction in this case, which introduce unsteadiness to the flow and complicate the construction of high quality meshes. Calculations comparing different turbulence models in a simplified 3D geometry are suggested. With a high quality mesh in a simpler geometry it would probably be possible to converge also RSM turbulence models which might give improved heat transfer predictions as they are capable of also revealing secondary flow structures contributing to heat transfer.

13 Final comments

In reality many physical phenomena are interlinked and their accurate numerical modelling requires coupled solution of the different processes. As the separate processes are typically solved with separate codes, explicit coupling needs to be implemented to transfer data between the different codes. Data transfer can be rather straightforward if the coupled codes use a similar numerical modelling approach, for example, data is transferred between identical mesh elements or discrete objects as could be done in this work when DEM data was utilised in the Monte Carlo reactor physics model. However, more effort is needed when data needs to be mapped between discrete and continuum models.

More detailed models and multi-physics considerations also add new requirements for experimental data suitable for validation. As an example, the reactor physics benchmark investigated in this work had a very detailed documentation what comes to constructing a Monte Carlo reactor physics model with the conventional approach of having the pebbles in an ordered lattice. However, the actual construction of the randomly packed pebble beds in the experiments was not covered. This would have been helpful for the enhanced approach where the pebble configurations were produced in DEM simulations. Although it is impossible to prepare for all possible future needs regarding the documentation of experiments, it is recommended that effort is put into considering at least the most obvious multi-physical aspects.

As can be concluded from the heat transfer results obtained in this work for the rib roughened rod it is essential to validate numerical models against experimental data. Results obtained with models that are inadequate for the specific problem can deviate significantly from the reality. Although the presented roughened rod results can be considered preliminary, as further work will be required to obtain better agreement with the experimental measurements, they were included in this thesis to emphasise the necessity of model validation. Although a model might be widely used and validated for multiple problems, obtaining good results especially for problems it has not been validated for is not predetermined.

When experiments are conducted with the purpose to produce validation data for numerical models they should be planned very carefully also from the viewpoint of the numerical modelling as not to inadvertently introduce unnecessary complications for the modelling. Examples from this work includes the complicated geometry of the ASTRA facility and the L-STAR test section inlet with unsteady flow behaviour. Construction of a high quality mesh especially for three dimensional calculations can be one of the most difficult and time consuming tasks in a CFD analysis. Planning the experimental configuration geometries also from the viewpoint of meshing is recommended. Challenging numerical simulations can be eased by careful planning and optimisation of the experiments for numerical analyses. Need to include additional details to a calculation model can reduce the resolution at which the more significant regions can be investigated. Details can be added and the resolution increased but eventually the simulation time will be increased to impractically long even for high end computer clusters. At best, experiments and calculations comple-

ment each other as experiments provide reassurance of the validity of calculations and the calculations then provide additional data that cannot be easily measured.

Despite the challenges, new improved approaches to increase understanding of different physical processes should be constantly pursued within the boundaries of available resources.

References

- Abe, S., Place, D., and Mora, P. (2004). A Parallel implementation of the lattice solid model for the simulation of rock mechanics and earthquake dynamics. *Pure and Applied Geophysics*, 161:2265–2277.
- Abedi, A. and Vosoughi, N. (2012). Neutronic simulation of a pebble bed reactor considering its double heterogeneous nature. *Nuclear Engineering and Design*, 253:277–284.
- Allen, M. P. and Tildesley, D. J. (1987). *Computer Simulation of Liquids*. Oxford University Press Inc., New York.
- An, X. Z., Li, C. X., Yang, R. Y., Zou, R. P., and Yu, A. B. (2009). Experimental study of the packing of mono-sized spheres subjected to one-dimensional vibration. *Powder Technology*, 196:50–55.
- ANSYS Inc. (2013a). *ANSYS Fluent Theory Guide, Release 15.0*. Canonsburg, Pennsylvania.
- ANSYS Inc. (2013b). *ANSYS Fluent User's Guide, Release 15.0*. Canonsburg, Pennsylvania.
- ANSYS Inc. (2013c). *ANSYS Fluent V2F Turbulence Model Manual, Release 15.0*. Canonsburg, Pennsylvania.
- ANSYS Inc. (2013d). *ANSYS ICEM CFD User's Manual, Release 15.0*. Canonsburg, Pennsylvania.
- Antypov, D. and Elliott, J. A. (2011). On an analytical solution for the damped Hertzian spring. *Europhysics Letters*, 94:50004.
- Arbeiter, F., Aberle, J., Böttcher, M., Gómez de Leija, R., Imke, U., Jianu, A., Krüßmann, R., and Scherrer, S. (2013a). Progress report on experimental L-STAR results. Internal Report INR 03/13 - NUKLEAR 3455, Karlsruhe Institute of Technology.
- Arbeiter, F., Aberle, J., Heupel, T., Krüßmann, R., Gómez de Leija, R., Jianu, A., Hering, W., and Scherrer, S. (2013b). Definition of the L-STAR/SL benchmark activities. Internal Report INR 34/12 - NUKLEAR 3450, Karlsruhe Institute of Technology.
- Auwerda, G. J., Kloosterman, J. L., Lathouwers, D., and van der Hagen, T. H. J. J. (2013). Macroscopic and microscopic packing properties of experimental and computational pebble beds. *Nuclear Technology*, 183:272–286.

- Auwerda, G. J., Kloosterman, J. L., Winkelman, A. J. M., Groen, J., and van Dijk, V. (2010). Comparison of experiments and calculations of void fraction distributions in randomly stacked pebble beds. In *Advances in Reactor Physics to Power the Nuclear Renaissance, PHYSOR 2010, Pittsburgh, Pennsylvania, USA, May 9 - 14, 2010*.
- Barber, C. B., Dobkin, D. P., and Huhdanpaa, H. T. (1996). The Quickhull algorithm for convex hulls. *ACM Transactions on Mathematical Software*, 22:469–483.
- Baumer, R. and Kalinowski, I. (1991). THTR commissioning and operating experience. *Energy*, 16:59–70.
- Berthoux, M. and Cadiou, T. (2010). The thermal hydraulics in a rod bundle representative of the start-up core of the ALLEGRO Gas cooled Fast Reactor - Experimental and numerical approaches. *Nuclear Engineering and Design*, 240:3372–3386.
- Brey, H. L. (1991). Fort St. Vrain operations and future. *Energy*, 16:47–58.
- Brown, F. B. and Martin, W. R. (2004). Stochastic geometry capability in MCNP5 for the analysis of particle fuel. *Annals of Nuclear Energy*, 31:2039–2047.
- Casey, M. and Wintergerste, T., editors (2000). *Special Interest Group on "Quality and Trust in Industrial CFD", Best Practice Guidelines, Version 1.0*. ERCOF-TAC.
- Cogliati, J. J. and Ougouag, A. M. (2006). PEBBLES: A computer code for modeling packing, flow and recirculation of pebbles in a pebble bed reactor. In *Proceedings of the 3rd International Topical Meeting on High Temperature Reactor Technology, HTR 2006, Johannesburg, South Africa, October 1-4, 2006*.
- Cogliati, J. J. and Ougouag, A. M. (2008). Pebble bed reactor dust production model. In *Proceedings of the 4th International Topical Meeting on High Temperature Reactor Technology, HTR 2008, Washington, DC, USA, September 28 - October 1, 2008*.
- Şeker, V. and Çolak, Ü. (2003). HTR-10 full core first criticality analysis with MCNP. *Nuclear Engineering and Design*, 222:263–270.
- Cui, J., Patel, V. C., and Lin, C. L. (2003). Large-eddy simulation of turbulent flow in a channel with rib roughness. *International Journal of Heat and Fluid Flow*, 24:372–388.
- Cundall, P. A. and Strack, O. D. L. (1979). A discrete numerical model for granular assemblies. *Géotechnique*, 29(1):47–65.

- Dalle Donne, M., Hudina, M., Huggenberger, M., Meyer, L., and Rehme, K. (1978). EIR, KfK joint heat transfer experiment on a single rod, roughened with trapezoidal rounded ribs and cooled by various gases. Technical Report KfK 2674, EUR 5755e, EIR-Bericht Nr. 349, Kernforschungszentrum Karlsruhe, Karlsruhe.
- Dalle Donne, M., Marek, J., Martelli, A., and Rehme, K. (1977). BR2 bundle mockup heat transfer experiments. *Nuclear Engineering and Design*, 40:143–156.
- Dalle Donne, M. and Meyer, L. (1977). Turbulent convective heat transfer from rough surfaces with two-dimensional rectangular ribs. *International Journal of Heat and Mass Transfer*, 20:583–620.
- Difilippo, F. C. (2003). Monte carlo calculations of pebble bed benchmark configurations of the PROTEUS facility. *Nuclear Science and Engineering*, 143:240–253.
- Dipprey, D. F. and Sabersky, R. H. (1963). Heat and momentum transfer in smooth and rough tubes at various Prandtl numbers. *International Journal of Heat and Mass Transfer*, 6:329–332.
- du Toit, C. G. (2002). The numerical determination of the variation in the porosity of the pebble-bed core. In *Proceedings of the 1st International Topical Meeting on High Temperature Reactor Technology, HTR 2002, Petten, Netherlands, April 22-24, 2002*.
- du Toit, C. G. (2006). Analysis of the radial variation in the porosity of annular packed beds. In *Proceedings of the 3rd International Topical Meeting on High Temperature Reactor Technology, HTR 2006, Johannesburg, South Africa, October 1-4, 2006*.
- du Toit, C. G. (2008). Radial variation in porosity in annular packed beds. *Nuclear Engineering and Design*, 238:3073–3079.
- Durbin, P. A. (1995). Separated flow computations with the $k - \epsilon - v^2$ model. *AIAA Journal*, 33:659–664.
- Epiney, A., Mikityuk, K., and Chawla, R. (2010). Heavy-gas injection in the Generation IV gas-cooled fast reactor for improved decay heat removal under depressurized conditions. *Nuclear Engineering and Design*, 240:3115–3125.
- Ergun, S. (1952). Fluid flow through packed columns. *Chemical Engineering Progress*, 48:89–94.
- Forestier, B., Miss, J., Jacquet, O., Bernard, F., and Verboomen, B. (2008). Criticality calculations on realistic modeling of pebble-bed HTR-PROTEUS as a validation for the Woodcock tracking method implemented in the MORET 5 Monte Carlo code. In *Proceedings of the 2008 International Congress on Advances in Nuclear Power Plants (ICAPP '08), Anaheim, California, June 8–12, 2008*.

- Fujikawa, S., Hayashi, H., Nakazawa, T., Kawasaki, K., Iyoku, T., Nakagawa, S., and Sakaba, N. (2004). Achievement of reactor outlet coolant temperature of 950°C in HTTR. *Journal of Nuclear Science and Technology*, 41:1245–1254.
- Gnielinski, V. (1976). New equations for heat and mass transfer in turbulent pipe and channel flow. *International Chemical Engineering*, 16:359–368.
- Gómez, R., Böttcher, M., Krüssmann, R., Aberle, J., Jianu, A., Scherrer, S., Arbeiter, F., and Hering, W. (2014a). Experiment results for heated rod in the L-STAR facility. In *THINS 2014 International Workshop, Modena, Italy, January 20–22, 2014*.
- Gómez, R., Buchholz, S., and Suikkanen, H. (2014b). Experimental and numerical investigation of heat transfer and pressure drop for innovative gas cooled systems. *Nuclear Engineering and Design*. Revised and resubmitted after minor comments.
- Gomez, R., Krussmann, R., Böttcher, M., Arbeiter, F., and Hering, W. (2013). Experimental investigation of heat transfer and pressure drop for turbulent air flows in smooth hexagonal channel. In *21st International Conference on Nuclear Engineering, Chengdu, China, July 29–August 2, 2013*.
- Goodjohn, A. J. (1991). Summary of gas-cooled reactor programs. *Energy*, 16:79–106.
- Goodling, J. S., Vachon, R. I., Stelpflug, W. S., and Ying, S. J. (1983). Radial porosity distribution in cylindrical beds packed with spheres. *Powder Technology*, 35:23–29.
- Han, J. C., Glicksman, L. R., and Rohsenow, W. M. (1978). An investigation of heat transfer and friction for rib-roughened surfaces. *International Journal of Heat and Mass Transfer*, 21:1143–1156.
- Hertz, H. (1881). Über die berührung fester elastischer körper. *Journal für die reine und angewandte Mathematik*, 92:156–171.
- Hishida, M., Fumizawa, M., Takeda, T., Ogawa, M., and Takenaka, S. (1993). Researches on air ingress accidents of the HTTR. *Nuclear Engineering and Design*, 144:317–325.
- Hudina, M. and Markòczy, G. (1977). The hexagonal bundle heat transfer and fluid flow experiment AGATHE HEX. *Nuclear Engineering and Design*, 20:121–131.
- Iaccarino, G., Ooi, A., Durbin, P. A., and Behnia, M. (2002). Conjugate heat transfer predictions in two-dimensional ribbed passages. *International Journal of Heat and Fluid Flow*, 23:340–345.
- Incropera, F. P., DeWitt, D. P., Bergman, T. L., and Lavine, A. S. (2006). *Fundamentals of Heat and Mass Transfer*. John Wiley & Sons, New Jersey, USA.

- Jiang, S., Yang, X., Tang, Z., Wang, W., Tu, J., Liu, Z., and Li, J. (2012). Experimental and numerical validation of a two-region-designed pebble bed reactor with dynamic core. *Nuclear Engineering and Design*, 246:277–285.
- Jodrey, W. S. and Tory, E. M. (1985). Computer simulation of close random packing of equal spheres. *Physical Review A*, 32:2347–2351.
- Kadak, A. C. and Bazant, M. Z. (2004). Pebble flow experiments for pebble bed reactors. In *Proceedings of the 2nd International Topical Meeting on High Temperature Reactor Technology, HTR 2004, Beijing, China, September 22-24, 2004*.
- Keppeler, I. (2013). Failure analysis of pebble bed reactors during earthquake by discrete element method. *Nuclear Engineering and Design*, 258:102–106.
- Keshmiri, A. (2011). Three-dimensional simulation of a simplified advanced gas-cooled reactor fuel element. *Nuclear Engineering and Design*, 241:4122–4135.
- Kloss, C., Goniva, C., Hager, A., Amberger, S., and Pirker, S. (2012). Models, algorithms and validation for opensource DEM and CFD-DEM. *Progress in Computational Fluid Dynamics*, 12:140–152.
- Koster, A., Matzner, H. D., and Nicholsi, D. R. (2003). PBMR design for the future. *Nuclear Engineering and Design*, 222:231–245.
- Kruggel-Emden, H., Sturm, M., Wirtz, S., and Scherer, V. (2008). Selection of an appropriate time integration scheme for the discrete element method (DEM). *Computers and Chemical Engineering*, 32:2263–2279.
- KTA 3102.3 (1981). *Reactor core design of high-temperature gas-cooled reactors, Part 3: Loss of pressure through friction in pebble bed cores*. Nuclear Safety Standards Commission (KTA), Federal Republic of Germany.
- Landau, L. D. and Lifshitz, E. M. (1986). *Theory of Elasticity*, volume 7 of *Course of Theoretical Physics*. Butterworth-Heinemann, Oxford, 3rd edition.
- Leppänen, J. (2007). *Development of a new Monte Carlo reactor physics code*. PhD thesis, Helsinki University of Technology, Helsinki, Finland.
- Leppänen, J. (2010). Performance of Woodcock delta-tracking in lattice physics applications using the Serpent Monte Carlo reactor physics burnup calculation code. *Annals of Nuclear Energy*, 37:715–722.
- Li, Y. and Ji, W. (2012). A collective dynamics-based method for initial pebble packing in pebble flow simulations. *Nuclear Engineering and Design*, 250:229–236.
- Li, Y. and Ji, W. (2013). Pebble flow and coolant flow analysis based on a fully coupled multi-physics model. *Nuclear Science and Engineering*, 173:150–162.

- Li, Y., Xu, Y., and Jiang, S. (2009). DEM simulations and experiments of pebble flow with monosized spheres. *Powder Technology*, 193:312–318.
- Li, Y., Xu, Y., and Thornton, C. (2005). A comparison of discrete element simulations and experiments for ‘sandpiles’ composed of spherical particles. *Powder Technology*, 160:219–228.
- Lieberoth, J. and Stojadinović, A. (1980). Neutron streaming in pebble beds. *Nuclear Science and Engineering*, 76:336–344.
- Lun, C. K. K. and Savage, S. B. (1986). The effects of an impact velocity dependent coefficient of restitution on stresses developed by sheared granular materials. *Acta Mechanica*, 63:15–44.
- Marnet, C., Ivens, G., and Ziermann, E. (1991). The AVR power plant in its last year of operation. *Energy*, 16:71–77.
- Martys, N. S. and Mountain, R. D. (1999). Velocity verlet algorithm for dissipative-particle-dynamics-based models of suspensions. *Physical Review E*, 59:3733–3736.
- Matulik, G., Tóth, S., and Aszódi, A. (2014). CFD analysis of the L-STAR facility and validation of the ANSYS CFX code for gas cooled reactor simulations. In *Proceedings of CFD4NRS-5 Application of CFD/CMFD codes to nuclear reactor safety and design and their experimental validation, Zurich, Switzerland, September 9–11, 2014*.
- Melese, G. and Katz, R. (1984). *Thermal and flow design of helium-cooled reactors*. American Nuclear Society, La Grange Park, Illinois.
- Melese-d’Hospital, G. and Simon, R. H. (1977). Status of gas-cooled fast breeder reactor programs. *Nuclear Engineering and Design*, 40:5–12.
- Mitchell, M. N. and Polson, A. G. (2007). Assessment of the loads on a solid centre reflector of a pebble bed reactor using DEM techniques. *Nuclear Engineering and Design*, 237:1332–1340.
- Miyake, Y., Tsujimoto, K., and Nakaji, M. (2001). Direct numerical simulation of rough-wall heat transfer in a turbulent channel flow. *International Journal of Heat and Fluid Flow*, 22:237–244.
- Mueller, G. E. (2010). Radial porosity in packed beds of spheres. *Powder Technology*, 203:626–633.
- Murata, I., Takahashi, A., Mori, T., and Nakagawa, M. (1997). New sampling method in continuous energy Monte Carlo calculation for pebble bed reactors. *Journal of Nuclear Science and Technology*, 34:734–744.

- Nagano, Y., Hattori, H., and Houra, T. (2004). DNS of velocity and thermal fields in turbulent channel flow with transverse-rib roughness. *International Journal of Heat and Fluid Flow*, 25:393–403.
- Nandakumar, K., Shu, Y., and Chuang, K. T. (1999). Predicting geometrical properties of random packed beds from computer simulation. *AIChE Journal*, 45:2286–2297.
- NERAC (2009). A Technology Roadmap for Generation IV Nuclear Energy Systems. Issued by the U.S. DOE Nuclear Energy Research Advisory Committee and the Generation IV International Forum.
- Nikuradse, J. (1933). Strömungsgesetze in rauhen Röhren. *Forschung auf dem Gebiete des Ingenieurwesens*, 361.
- Ougouag, A. M. and Cogliati, J. J. (2007). Earthquakes and pebble bed reactors: Time-dependent densification. In *Mathematics & Computation and Supercomputing in Nuclear Applications, Monterey, CA, USA, April 15-19, 2007*.
- Ougouag, A. M., Cogliati, J. J., and Kloosterman, J.-L. (2005). Methods for modeling the packing of fuel elements in pebble bed reactors. In *Mathematics and Computation, Supercomputing, Reactor Physics and Nuclear and Biological Applications, Avignon, France, September 12-15, 2005*.
- Ougouag, A. M., Ortensi, J., and Hiruta, H. (2009). Analysis of an earthquake-initiated-transient in a PBR. In *International Conference on Mathematics, Computational Methods & Reactor Physics, M&C 2009, Saratoga Springs, New York, USA, May 3-7, 2009*.
- Patel, V. C., Rodi, W., and Scheuerer, G. (1985). Turbulence models for near-wall and low reynolds number flows: A review. *AIAA Journal*, 23:1308–1319.
- Plimpton, S. (1995). Fast Parallel Algorithms for Short-Range Molecular Dynamics. *Journal of Computational Physics*, 117:1–19.
- Poette, C., Malo, J. Y., Brun-Magaud, V., Morin, F., Dor, I., Mathieu, B., Duhamel, H., Stainsby, R., and Mikityuk, K. (2009). GFR demonstrator ALLEGRO design status. In *Proceedings of ICAPP '09, Tokyo, Japan, May 10-14, 2009*.
- Ponomarev-Stepnoi, N. N., Glushkov, E. S., Kompaniets, G. V., and Polyakov, D. N. (2008). Graphite annular core assemblies with spherical fuel elements containing coated UO₂ fuel particles. In *International Handbook of Evaluated Reactor Physics Benchmark Experiments, March 2012 Edition*. OECD NEA Nuclear Science Committee. NEA/NSC/DOC(2006)01.
- Pöschel, T. and Schwager, T. (2005). *Computational Granular Dynamics*. Springer, Berlin Heidelberg.

- Rau, G., Çakan, M., Moeller, D., and Arts, T. (1998). The effect of periodic ribs on the local aerodynamic and heat transfer performance of a straight cooling channel. *Journal of Turbomachinery*, 120:368–375.
- Rintala, V., Suikkanen, H., Leppänen, J., and Kyrki-Rajamäki, R. (2014). Modelling of realistic pebble bed reactor geometries using the Serpent Monte Carlo code. *Annals of Nuclear Energy*. Accepted.
- Roelofs, F., Shams, A., Hering, W., Otic, I., Papukchiev, A., Lathouwers, D., Pavlidis, D., Suikkanen, H., Hassan, Y., Barth, T., Niceno, B., and Cheng, X. (2012). HTR Related Activities within the European Thermal-Hydraulics for Innovative Nuclear Systems (THINS) Project. In *6th International Topical Meeting on High Temperature Reactor Technology HTR2012, Miraikan, Tokyo, Japan, October 28 – November 1, 2012*.
- Rycroft, C. H. (2009). Voro++: A three-dimensional Voronoi cell library in C++. *Chaos*, 19:041111.
- Rycroft, C. H., Grest, G. S., Landry, J. W., and Bazant, M. Z. (2006). Analysis of granular flow in a pebble-bed nuclear reactor. *Physical Review E*, 74:021306.
- Rycroft, C. H., Lind, T., Güntay, S., and Dehbi, A. (2012). Granular flow in pebble bed reactors: dust generation and scaling. In *Proceedings of ICAPP '12, Chicago, USA, June 24–28, 2012*.
- Ryu, D. N., Choi, D. H., and Patel, V. C. (2007a). Analysis of turbulent flow in channels roughened by two-dimensional ribs and three-dimensional blocks. Part I: Resistance. *International Journal of Heat and Fluid Flow*, 28:1098–1111.
- Ryu, D. N., Choi, D. H., and Patel, V. C. (2007b). Analysis of turbulent flow in channels roughened by two-dimensional ribs and three-dimensional blocks. Part II: Heat transfer. *International Journal of Heat and Fluid Flow*, 28:1112–1124.
- Shih, T., Liou, W. W., Shabbir, A., Yang, Z., and Zhu, J. (1995). A new $k - \epsilon$ eddy viscosity model for high Reynolds number turbulent flows. *Computers Fluids*, 24:227–238.
- Shiozawa, S., Fujikawa, T., Iyoku, T., Kunitomi, K., and Tachibana, Y. (2004). Overview of HTTR design features. *Nuclear Engineering and Design*, 233:11–21.
- Simmad, M. T. (1991). The early history of high-temperature helium gas-cooled nuclear power reactors. *Energy*, 16:25–32.
- Stainsby, R., Peers, K., Mitchell, C., Poette, C., Mikityuk, K., and Somers, J. (2011). Gas cooled fast reactor research in Europe. *Nuclear Engineering and Design*, 241:3481–3489.

- Stansfield, O. M. (1991). Evolution of HTGR coated particle fuel design. *Energy*, 16:33–45.
- Suikkanen, H., Rintala, V., and Kyrki-Rajamäki, R. (2010). An approach for detailed reactor physics modelling of randomly packed pebble beds. In *Proceedings of HTR 2010, Prague, Czech Republic, October 18-20, 2010*.
- Suikkanen, H., Rintala, V., and Kyrki-Rajamäki, R. (2014a). Development of a coupled multi-physics code system for pebble bed reactor core modeling. In *Proceedings of the HTR 2014, Weihai, China, October 27-31, 2014*.
- Suikkanen, H., Ritvanen, J., Jalali, P., and Kyrki-Rajamäki, R. (2014b). Discrete element modelling of pebble packing in pebble bed reactors. *Nuclear Engineering and Design*, 273:24–32.
- Takase, K. (1996). Numerical prediction of augmented turbulent heat transfer in an annular fuel channel with repeated two-dimensional square ribs. *Nuclear Engineering and Design*, 165:225–237.
- Tsuji, Y., Tanaka, T., and Ishida, T. (1992). Lagrangian numerical simulation of plug flow of cohesionless particles in a horizontal pipe. *Powder Technology*, 71:239–250.
- Vafai, K., editor (2000). *Handbook of Porous Media*. Marcel Dekker, New York.
- Vargas, W. L. and McCarthy, J. J. (2001). Heat conduction in granular materials. *AIChE Journal*, 47:1052–1059.
- VDI-Wärmeatlas (1988). VDI-Verlag, Düsseldorf, 5th edition.
- Venter, P. J. and Mitchell, M. N. (2007). Integrated design approach of the pebble bed modular reactor using models. *Nuclear Engineering and Design*, 237:1341–1353.
- Visscher, W. M. and Bolsterli, M. (1972). Random packing of equal and unequal spheres in two and three dimensions. *Nature*, 239:2727–2730.
- Voronoi, G. (1907). Nouvelles applications des paramètres continus à la théorie des formes quadratiques. *Journal für die reine und angewandte Mathematik*, 133:97–178.
- Waltar, A. E., Todd, D. R., and Tsvetkov, P. V. (2012). *Fast Spectrum Reactors*. Springer, New York.
- Walton, O. R. and Braun, R. L. (1986). Viscosity, granular-temperature, and stress calculations for shearing assemblies of inelastic, frictional disks. *Journal of Rheology*, 30:949–980.

- Webb, R. L., Eckert, E. R. G., and Goldstein, R. J. (1971). Heat transfer and friction in tubes with repeated-rib roughness. *International Journal of Heat and Mass Transfer*, 14:601–617.
- White, F. M. (2003). *Fluid Mechanics*. McGraw-Hill, New York, 5th edition.
- White, F. M. (2006). *Viscous Fluid Flow*. McGraw-Hill, New York, 3rd edition.
- Wilcox, D. C. (2006). *Turbulence Modeling for CFD*. DCW Industries, Inc., La Canada, CA, 3rd edition.
- Wolfstein, M. (1969). The velocity and temperature distribution of one-dimensional flow with turbulence augmentation and pressure gradient. *International Journal of Heat and Mass Transfer*, 12:301–318.
- Wu, Z., Lin, D., and Zhong, D. (2002). The design features of the HTR-10. *Nuclear Engineering and Design*, 218:25–32.
- Xiaowei, L., Xiaotian, L., and Suyuan, Y. (2010). Nuclear graphite friction properties and the influence of friction properties on the pebble bed. *Nuclear Engineering and Design*, 240:2674–2681.
- Xu, Y. and Zuo, K. (2002). Overview of the 10 MW high temperature gas cooled reactor - test module project. *Nuclear Engineering and Design*, 218:13–23.
- Yang, X. T., Hu, W. P., Jiang, S. Y., Wong, K. K. L., and Tu, J. Y. (2012). Mechanism analysis of quasi-static dense pebble flow in pebble bed reactor using phenomenological approach. *Nuclear Engineering and Design*, 250:247–259.
- Zhang, Z., Wu, Z., Wang, D., Xu, Y., Sun, Y., Li, F., and Dong, Y. (2009). Current status and technical description of Chinese 2×250 MWth HTR-PM demonstration plant. *Nuclear Engineering and Design*, 239:1212–1219.

ACTA UNIVERSITATIS LAPPEENRANTAENSIS

569. KARPPINEN, HENRI. Reframing the relationship between service design and operations: a service engineering approach. 2014. Diss.
570. KALLIO, SAMULI. Modeling and parameter estimation of double-star permanent magnet synchronous machines. 2014. Diss.
571. SALMELA, ERNO. Kysyntä-toimitusketjun synkronointi epävarman kysynnän ja tarjonnan toimintaympäristössä. 2014. Diss.
572. RIUNGU-KALLIOSAARI, LEAH. Empirical study on the adoption, use and effects of cloud-based testing. 2014. Diss.
573. KINNARINEN, TEEMU. Pressure filtration characteristics of enzymatically hydralyzed biomass suspensions. 2014. Diss.
574. LAMMASSAARI, TIMO. Muutos kuntaorganisaatiossa – tapaustutkimus erään kunnan teknisestä toimialasta. 2014. Diss.
575. KALWAR, SANTOSH KUMAR. Conceptualizing and measuring human anxiety on the Internet. 2014. Diss.
576. LANKINEN, JUKKA. Local features in image and video processing – object class matching and video shot detection. 2014. Diss.
577. AL-SAEDI, MAZIN. Flexible multibody dynamics and intelligent control of a hydraulically driven hybrid redundant robot machine. 2014. Diss.
578. TYSTER, JUHO. Power semiconductor nonlinearities in active du/dt output filtering. 2014. Diss.
579. KERÄNEN, JOONA. Customer value assessment in business markets. 2014. Diss.
580. ALEXANDROVA, YULIA. Wind turbine direct-drive permanent-magnet generator with direct liquid cooling for mass reduction. 2014. Diss.
581. HUHTALA, MERJA. PDM system functions and utilizations analysis to improve the efficiency of sheet metal product design and manufacturing. 2014. Diss.
582. SAUNILA, MINNA. Performance management through innovation capability in SMEs. 2014. Diss.
583. LANA, ANDREY. LVDC power distribution system: computational modelling. 2014. Diss.
584. PEKKARINEN, JOONAS. Laser cladding with scanning optics. 2014. Diss.
585. PELTOMAA, JYRKI. The early activities of front end of innovation in OEM companies using a new FEI platform as a framework for renewal. 2014. Diss.
586. ROZHANSKY, IGOR. Resonant tunneling effects in semiconductor heterostructures. 2014. Diss.
587. PHAM, THUY DUONG. Ultrasonic and electrokinetic remediation of low permeability soil contaminated with persistent organic pollutants. 2014. Diss.
588. HOKKANEN, SANNA. Modified nano- and microcellulose based adsorption materials in water treatment. 2014. Diss.
589. HINKKANEN, JUHA. Cooperative strategy in emerging markets – analysis of interfirm R&D cooperation and performance in Russian manufacturing companies. 2014. Diss.

590. RUSKOVAARA, ELENA. Entrepreneurship education in basic and upper secondary education – measurement and empirical evidence. 2014. Diss.
591. IKÄHEIMONEN, TUULI. The board of directors as a part of family business governance – multilevel participation and board development. 2014. Diss.
592. HAJIALI, ZUNED. Computational modeling of stented coronary arteries. 2014. Diss.
593. UUSITALO, VILLE. Potential for greenhouse gas emission reductions by using biomethane as road transportation fuel. 2014. Diss.
594. HAVUKAINEN, JOUNI. Biogas production in regional biodegradable waste treatment – possibilities for improving energy performance and reducing GHG emissions. 2014. Diss.
595. HEIKKINEN, JANNE. Vibrations in rotating machinery arising from minor imperfections in component geometries. 2014. Diss.
596. GHALAMCHI, BEHNAM. Dynamic analysis model of spherical roller bearings with defects. 2014. Diss.
597. POLIKARPOVA, MARIIA. Liquid cooling solutions for rotating permanent magnet synchronous machines. 2014. Diss.
598. CHAUDHARI, ASHVINKUMAR. Large-eddy simulation of wind flows over complex terrains for wind energy applications. 2014. Diss.
599. PURHONEN, MIKKO. Minimizing circulating current in parallel-connected photovoltaic inverters. 2014. Diss.
600. SAUKKONEN, ESA. Effects of the partial removal of wood hemicelluloses on the properties of kraft pulp. 2014. Diss.
601. GUDARZI, DAVOOD. Catalytic direct synthesis of hydrogen peroxide in a novel microstructured reactor. 2014. Diss.
602. VALKEAPÄÄ, ANTTI. Development of finite elements for analysis of biomechanical structures using flexible multibody formulations. 2014. Diss.
603. SSEBUGERE, PATRICK. Persistent organic pollutants in sediments and fish from Lake Victoria, East Africa. 2014. Diss.
604. STOKLASA, JAN. Linguistic models for decision support. 2014. Diss.
605. VEPSÄLÄINEN, ARI. Heterogenous mass transfer in fluidized beds by computational fluid dynamics. 2014. Diss.
606. JUVONEN, PASI. Learning information technology business in a changing industry landscape. The case of introducing team entrepreneurship in renewing bachelor education in information technology in a university of applied sciences. 2014. Diss.
607. MÄKIMATTILA, MARTTI. Organizing for systemic innovations – research on knowledge, interaction and organizational interdependencies. 2014. Diss.
608. HÄMÄLÄINEN, KIMMO. Improving the usability of extruded wood-plastic composites by using modification technology. 2014. Diss.
609. PIRTTILÄ, MIIA. The cycle times of working capital: financial value chain analysis method. 2014. Diss.

